

Optical Absorption Measurements for Third Generation Gravitational Wave Detectors

Von der Fakultät für Mathematik und Physik
der Gottfried Wilhelm Leibniz Universität Hannover
zur Erlangung des Grades

Doktorin der Naturwissenschaften
– Dr. rer. nat. –

genehmigte Dissertation
von

Dipl.-Phys. Jessica Steinlechner

geboren am 28.05.1981 in Schongau

2013

Referent: Prof. Dr. Roman Schnabel
Korreferent: Prof. Dr. Karsten Danzmann
Tag der Promotion: 05.02.2013

Abstract

Large-scale Michelson interferometers were developed for the purpose of the first direct measurement of gravitational waves (GWs). Since 2002 several science runs of the 1st generation of GW detectors (GWDs) took place. Currently the detectors are being reconstructed and updated. The 2nd generation of GWDs is planned to come on-line in 2015/16. The 3rd generation is in the design phase. For example, the Einstein Telescope (ET) is planned to use techniques such as squeezed light and cryogenic test-masses to reduce the level of quantum noise and thermal noise.

The reduction of these noise sources requires precise knowledge of the optical absorption of various materials. This thesis strongly contributed to the development of the photo-thermal self-phase modulation technique and contains first experimental applications. Absorptions of bulk substrates and high reflective mirror coatings were measured. The results are important for future GWDs and additionally supported the commissioning of the new measurement technique.

Absorption measurements were performed on PPKTP, which is used for second harmonic and squeezed light generation at 1550 nm. The results of $\alpha_{775\text{nm}} = (127 \pm 24)$ ppm/cm and $\alpha_{1550\text{nm}} = (84 \pm 40)$ ppm/cm showed that the absorption of PPKTP by far does not limit an achievable non-classical noise suppression of 10 dB as envisioned for GWDs.

ET is expected to reach sensitivities where quantum radiation pressure noise becomes significant. For cryogenic experiments which work on the measurement and characterization of this noise source, the absorption of silicon nitride membranes at different wavelengths was measured. An absorption of about 1 ppm/nm at 1064 nm was found, which decreased by a factor of 10 at 1550 nm. This makes 1550 nm a suitable wavelength for such cryogenic radiation pressure noise experiments.

Due to its high mechanical quality-factor at low temperatures, crystalline silicon (Si) is currently being discussed as a test-mass material for GWDs at cryogenic temperatures. Within this work absorption measurements on a Si sample at 1550 nm were performed at room temperature and the absorption coefficient for an intensity of 700 W/cm^2 was found to be $\alpha_{1550\text{nm}} = (264 \pm 39)$ ppm/cm. This experiment was a first step in the characterization of silicon absorption.

Further, the absorption of the highly reflective $\text{SiO}_2/\text{Ta}_2\text{O}_5$ mirror coatings at 1550 nm is of interest. A value of $\alpha_{1550\text{nm}} = (1.7 \pm 0.3)$ ppm was found, which is in the same order as $\alpha_{1064\text{nm}}$. A wavelength of 1550 nm might also give the chance for new coating materials like Si/SiO₂. The absorption of such coatings produced with the ion plating procedure was measured to (1035 ± 42) ppm, which is unsuitable for GWDs.

Within this work a new absorption measurement technique was established and valuable results for future GWDs were found, especially at a wavelength of 1550 nm.

Keywords: gravitational wave detectors, optical absorption, photo-thermal self-phase modulation, silicon, PPKTP, silicon nitride, coatings

Kurzfassung

Mit dem Ziel Gravitationswellen erstmals direkt zu messen, wurden weltweit hochempfindliche Laserinterferometer mit mehreren Kilometern Armlänge entwickelt. Seit 2002 fanden mehrere Messphasen der ersten Generation dieser Gravitationswellendetektoren (GWD) statt. Einige dieser Detektoren werden derzeit umgebaut, um eine höhere Messempfindlichkeit zu erzielen. Die Inbetriebnahme dieser zweiten Generation ist in den Jahren 2015/16 geplant. Die nachfolgende dritte Generation befindet sich zurzeit in der Entwicklungsphase. Für das *Einstein Telescope* (ET) ist beispielsweise geplant, Techniken wie gequetschtes Licht und kryogene Testmassen zu verwenden, um die Beiträge von Quantenrauschen und thermischem Rauschen zu senken.

Eine Verringerung dieser Rauschquellen erfordert eine exakte Kenntnis der optischen Absorption diverser Materialien. Diese Arbeit hat maßgeblich zur Entwicklung der photothermischen Selbstphasenmodulationstechnik beigetragen. Erste experimentelle Anwendungen wurden in Form von Absorptionsmessungen an Substraten und hochreflektierenden optischen Beschichtungen realisiert. Die Ergebnisse sind für die Planung zukünftiger GWD relevant und unterstützten die Etablierung der neuen Messtechnik.

Messungen an PPKTP, welches zur Erzeugung der zweiten Harmonischen sowie von gequetschtem Licht bei 1550 nm verwendet wird, ergaben Absorptionen von $\alpha_{775\text{nm}} = (127 \pm 24)$ ppm/cm und $\alpha_{1550\text{nm}} = (84 \pm 40)$ ppm/cm. Dies zeigte, dass die geplante Unterdrückung des Quantenrauschens um 10 dB für zukünftige GWD nicht durch die Absorption von PPKTP limitiert ist.

Für ET wird eine Empfindlichkeit erwartet, bei der Strahlungsdruckrauschen signifikant wird. Kryogene Experimente, die an der Charakterisierung dieser Rauschquelle arbeiten, verwenden Siliziumnitritmembranen. Die gemessene Absorption dieser Membranen betrug 1 ppm/nm bei 1064 nm und sank um etwa einen Faktor 10 zu 1550 nm hin. Damit ist 1550 nm eine geeignete Wellenlänge für solche kryogenen Strahlungsdruckrauschexperimente.

Aufgrund der hohen mechanischen Güte bei niedrigen Temperaturen, wird kristallines Silizium als Testmassenmaterial für kryogene GWD in Erwägung gezogen. In dieser Arbeit wurde an einer Siliziumprobe eine Absorption von $\alpha_{1550} = (264 \pm 39)$ ppm/cm bei einer Leistungsdichte von 700 W/cm^2 und Raumtemperatur gemessen. Dieses Experiment war ein erster Schritt zur Charakterisierung der Absorption von Silizium.

Des Weiteren ist die Absorption hochreflektierender $\text{SiO}_2/\text{Ta}_2\text{O}_5$ Spiegelbeschichtungen bei 1550 nm von Interesse. Ein Wert von $\alpha_{1550\text{nm}} = (1.7 \pm 0.3)$ ppm pro Spiegelbeschichtung wurde gemessen und liegt damit in der selben Größenordnung wie bei 1064 nm. Ferner wurde Si/SiO₂ als neues Beschichtungsmaterial bei 1550 nm untersucht. Für solche im *Ion Plating* Verfahren hergestellten Beschichtungen wurde eine Absorption von (1035 ± 42) ppm pro Beschichtung gemessen, die um etwa drei Größenordnungen über der von $\text{SiO}_2/\text{Ta}_2\text{O}_5$ liegt und somit nicht für GWD in Frage kommt.

Im Rahmen dieser Arbeit wurde ein neues Verfahren zur Absorptionsmessung etabliert und es konnten damit nützliche Ergebnisse für die Planung zukünftiger GWD, insbesondere bei einer Wellenlänge von 1550 nm, gewonnen werden.

Stichworte: Gravitationswellendetektor, optische Absorption, photothermische Selbstphasenmodulation, Silizium, PPKTP, Siliziumnitrit, Beschichtungen

Contents

Abstract	III
Kurzfassung	V
1 Introduction	1
References	7
2 Cavity Theory	13
2.1 Cavity Fields and Powers	13
2.2 Ringing Effects	17
2.3 Traveling-Wave Cavities	19
2.4 The Gaussian Beam	19
References	21
3 The Photo-Thermal Self-Phase Modulation Technique	23
3.1 Introduction	23
3.2 Illustrative Explanation of the Photo-Thermal Self-Phase Modulation Effect	26
3.2.1 The Photo-Thermal Self-Phase Modulation Effect in a Bulk Sub-	
strate	26
3.2.2 The Photo-Thermal Self-Phase Modulation Effect in a High-Reflective	
Mirror-Coating	28
3.3 The Time-Domain Simulation Model	30
3.3.1 Theoretical Model	30
3.3.2 Input Parameters of the Simulation	36
3.3.3 The Results	40
References	43

4	Demonstration of the Measurement Principle	45
4.1	Measuring the Absorption Coefficient of a Bulk Substrate	46
4.1.1	Experimental Setup	46
4.1.2	Calibration of the Time Axis	47
4.1.3	Measurement and Data Analysis	50
4.1.4	Error Propagation	52
4.1.5	The Final Results	54
4.2	Measuring the Absorption of High Reflective Coatings	55
4.2.1	Experimental Procedure and Setup	55
4.2.2	Measurement and Data Analysis	57
4.2.3	Experimental Results and Error Propagation	58
4.2.4	Final Results and Discussion	60
4.3	Conclusion	61
	References	63
5	Absorption Measurements on Crystalline Silicon	65
5.1	Introduction	65
5.2	Absorption Measurements on Silicon Sample A	66
5.2.1	Experimental Setup	67
5.2.2	Measurement Analysis and Results	68
5.2.3	Error Propagation	71
5.3	Measurements on Silicon Sample B	71
5.4	Doping and Contaminations of the Material	73
5.5	Intensity-Dependent Absorption of Silicon	75
5.6	Conclusion and Outlook	76
	References	81
6	Absorption Measurements on PPKTP at 775 nm and 1550 nm	85
6.1	Introduction	85
6.2	Experimental Setups	86
6.2.1	Experimental Setup and Results at 775 nm	89
6.2.2	Experimental Setup and Results at 1550 nm	91
6.3	Conclusion	92
	References	93
7	Optical Absorption Measurements on Thin SiN Membranes	97
7.1	Measurements of the Membrane Temperature with an IR Camera	98
7.2	Absorption Measurements at 1064 nm and 1550 nm	100
7.2.1	Experimental Setup	102
7.2.2	Experimental Results	103
7.2.3	Error Propagation	104
7.3	Calibration of the Temperature Measurements	106

7.4	Final Results and Conclusion	107
	References	109
8	Absorption Measurements on High Reflective Coatings at 1550 nm	111
8.1	Absorption Measurements on a Ta ₂ O ₅ /SiO ₂ Coating at 1550 nm	112
8.1.1	Experimental Setup	113
8.1.2	Results and Error Propagation	113
8.1.3	Discussion	116
8.2	Absorption Measurements on a Si/SiO ₂ Coating at 1550 nm	116
8.2.1	Experimental Setup	116
8.2.2	Experimental Results and Error Propagation	118
8.2.3	Discussion and Conclusion	120
	References	123
9	Conclusion	127
	Curriculum Vitae	133

List of Figures

1.1	Effect of a gravitational wave passing a ring of test-masses	1
1.2	Schematic of a Michelson interferometer for gravitational wave detection .	2
1.3	Effect of a gravitational wave passing a Michelson interferometer	3
1.4	Fundamental noise contribution planned for the Einstein Telescope	5
2.1	Schematic of a Fabry-Perot cavity	14
2.2	Phase-dependend laser power in reflection of a cavity	16
2.3	Impedance mismatch and power build of a cavity	17
2.4	Ringling effects of cavity resonance peaks	18
2.5	Examples of traveling-wave ring-cavities	19
2.6	Gaussian amplitude distribution and Rayleigh range of a laser beam	20
3.1	Illustration of the Beer-Lambert law	24
3.2	Schematic of a Herriott call	25
3.3	Absorption measurement method exploiting a thermal lens	26
3.4	Illustration of the photo-thermal self-phase modulation effect	27
3.5	Simulation of reflected cavity resonance peaks with and without thermal effect	28
3.6	Effect of changing laser power and scan frequency on reflected resonance peaks	29
3.7	Photo-thermal self-phase modulation caused by absorption of the in-coupling mirror coating	31
3.8	Schematic of the cylindrical test-mass with length h and radius a used for the time-domain model	31
3.9	Temperature distribution within a bulk-substrate caused by absorption . .	35
3.10	Aberration of a laser beam caused by heating in a substrate due to phot- thermal self-phase modulation	37

List of Figures

3.11	Obtaining reflectivities and absorption from reflected resonance peaks . . .	41
3.12	Effect of the thermal conductivity on resonance peaks	42
4.1	Experimental setup used for the absorption measurements on LiNbO ₃ . . .	47
4.2	Calibration of the mirror motion	49
4.3	Examples of measured resonance peaks with and without thermal effect .	51
4.4	Data chain from the MCMC algorithm	52
4.5	Histograms that show results from the MCMC algorithm	53
4.6	Single results and mean value for the absorption coefficient of LiNbO ₃ . .	54
4.7	Experimental setup used for the absorption measurements on high reflective SiO ₂ /Ta ₂ O ₅ coatings	55
4.8	Example of measured resonance peaks showing a thermal effect	56
4.9	Individual measurement results for the absorption of mirror samples A and B	59
5.1	Schematic of the experimental layout for the absorption measurements on silicon sample A	67
5.2	Example of measured and simulated resonance peaks for silicon sample A	68
5.3	Results for the absorption from single measurements on silicon sample A .	70
5.4	Experimental setup for the measurement on silicon sample B	71
5.5	Results for the lower limit of the absorption measured on silicon sample B	73
5.6	Literature data for the wavelength dependent absorption of silicon	74
5.7	Deformed resonance peaks at higher input power	76
5.8	Photographs of a previous silicon substrate taken with an IR camera . . .	79
6.1	Measured and simulated cavity resonance peaks from the absorption measurements on PPKTP	88
6.2	Setups for the absorption measurements on PPKTP at 775 nm and 1550 nm	90
6.3	Absorption results of the individual measurements at 775 nm and 1550 nm	91
7.1	Theoretical model and experimental results for the absorption of thin membranes at 1064 nm	98
7.2	Temperature profile of membrane 1000 nm no3 for 6.1 mW absorbed power	99
7.3	Temperature increase with cavity round-trip power for different membranes at 1064 nm and 1550 nm	100
7.4	Simulated reflected resonance peaks for a cavity containing different membranes at 1064 nm	101
7.5	Experimental setup for the membrane loss measurements	103
7.6	Reflected measured and simulated resonance peaks for the 1064 nm cavity without membrane	104
7.7	Measurement principle of NFSR	106
7.8	Membrane absorption with wavelength	107

8.1	Schematics of $\text{SiO}_2/\text{Ta}_2\text{O}_5$ and Si/SiO_2 coating stacks	112
8.2	Schematic of the cavity used for the absorption measurements on $\text{Ta}_2\text{O}_5/\text{SiO}_2$ coatings at 1550 nm	113
8.3	Two examples of measured and simulated reflected resonance peaks . . .	115
8.4	Measurement results for $\text{SiO}_2/\text{Ta}_2\text{O}_5$ HR-coatings at 1550 nm	117
8.5	Reflected resonance peaks for different scan-frequencies at constant scan-amplitude and input power	119
8.6	Measurement results for Si/SiO_2 coatings at 1550 nm	121

List of Tables

3.1	Parameters used to simulate the temperature distributions for bulk and coating absorption shown in Fig. 3.9	34
3.2	Example of an input parameter file for the simulation program <code>tksim</code> . . .	38
4.1	Material and geometric parameters for the absorption measurements on LiNbO_3	48
4.2	NFSRs and results for R_1 , \tilde{R}_2 and α for all single absorption measurements on LiNbO_3	50
4.3	Material and geometric parameters for the absorption measurements on high reflective $\text{SiO}_2/\text{Ta}_2\text{O}_5$ coatings at 1064 nm	58
4.4	Results for R_1 , \tilde{R}_2 and α for high reflective $\text{SiO}_2/\text{Ta}_2\text{O}_5$ coatings at 1064 nm	59
5.1	Scan-frequencies used for the single measurements on silicon	68
5.2	Parameters for the absorption measurements on silicon	69
6.1	Parameters of the bow-tie cavity and the half-monolithic cavity used for absorption measurements on PPKTP at 775 nm and 1550 nm.	87
7.1	Fitted slope coefficient a of temperature increase with power of the membrane surfaces for different membranes and wavelengths	101
7.2	Parameters and results for the wavelength dependent absorption measured on membrane surfaces with an IR camera	102
7.3	Results for the absorption of different membranes at 1064 nm and 1550 nm	105
7.4	Effect of the input parameters on the results of the membrane experiment	106
8.1	Parameters for the absorption measurements on high reflective mirror coatings at 1550 nm	114

In the year 1916 Albert Einstein published the general theory of relativity [1.1]. One of the predictions of this theory is the existence of gravitational waves (GWs) [1.2], which are perturbations in the curvature of space-time and propagate with the speed of light. Examples of GW sources are neutron-star and black-hole binaries, supernovae or the stochastic background which consists of various possible sources [1.3]. GWs have a quadrupole nature [1.4] that influences the distance between objects as illustrated in Fig. 1.1. When a GW passes the ring of masses shown in Fig. 1.1a in y -direction (into the paper-plane), the distances between the masses are stretched vertically during the first half wave-period (see Fig. 1.1b) and stretched horizontally during the second half wave-period (see Fig. 1.1c).

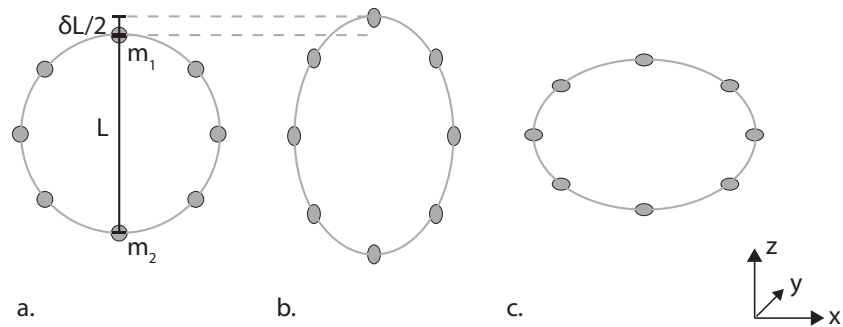
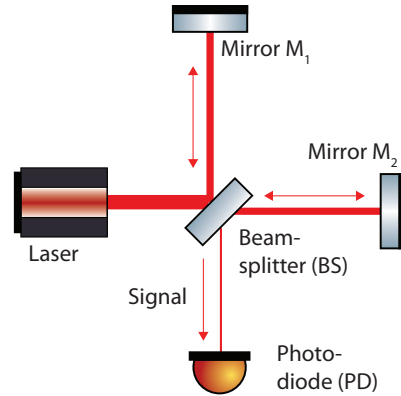


Figure 1.1: A gravitational wave passes a ring of masses (a.) in y -direction (into the paper-plane): During the first half wave-period the distances between the masses are stretched vertically (b.), during the second half wave-period the distances are stretched horizontally (c.). The distance L of the two masses 1 and 2 changes by δL .

1 Introduction

Figure 1.2: Schematic of a simple Michelson interferometer for gravitational wave detection: A 50/50 beam splitter (BS) divides the light emitted by a laser. One part of the beam is transmitted, the other part is reflected in an angle of about 90° . Both partial beams are reflected at the mirrors M_1 and M_2 and pass the BS a second time. The photo diode (PD) detects the superposition of both partial beams, which interfere at the output resulting in a signal that depends on the phase difference.



The amplitude of a GW is defined by its relative length change $h = 2\delta L/L$ [1.5]. The strength of h depends on the distance r between GW source and observatory and the reduced quadrupole moment I of the source

$$h = \frac{2G}{c^4} \frac{1}{r} \frac{\partial^2 I}{\partial t^2}, \quad (1.1)$$

where G is Newton's gravitational constant and c is the speed of light. Since the event rate of GW sources increases rapidly with the monitoring distance, the chance to detect GWs increases with the detectors' sensitivity. An overview of GW sources, their strength and the resulting event rate can be found in [1.6].

While there is already strong evidence for the existence of GWs via observations on binary pulsars [1.7, 1.8], up to now GWs could not be directly measured. The reason for not being able to directly detect GWs in the past are the high sensitivity requirements for possible detectors. The strongest GWs reaching earth are expected to be in the order of a relative length change of 10^{-21} .

The first attempts to detect GWs were done in the 1960s by Joseph Weber using bar detectors. These detectors are based on cylindric aluminium masses with a weight of a few tons [1.9, 1.10], which are suspended isolated from outside vibrations. GWs excite the bar's resonant frequency. The first bar detectors had one resonance frequency with a band width of a few hertz where the sensitivity was highest. Newer detectors like NAUTILUS [1.11] have two resonances a few 10 Hz apart due to a bar-transducer system with slightly different quality factors to increase the band-width. Today's cryogenically cooled bar detectors can reach sensitivities up to $10^{-21} - 10^{-22}$ [1.11, 1.12].

Later, interferometric gravitational wave detectors (GWDs) were developed [1.13]. These detectors are based on Michelson interferometers with up to several kilometers arm length [1.14]. A schematic of a Michelson interferometer is shown in Fig. 1.2. The light emitted by a laser passes a 50/50 beam splitter (BS), where one part of the beam is transmitted, while the other part is reflected in an angle of about 90° to maximize the sensitivity for GWs. Both partial beams are reflected by high reflective mirrors M_1 and M_2 before passing the BS a second time. A photo diode (PD) detects the superposition

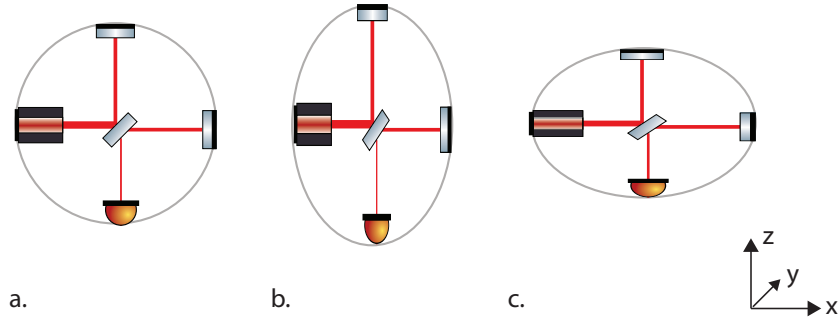


Figure 1.3: A schematic of a Michelson interferometer is shown in a. When a GW passes the interferometer the arms are stretched (b) and compressed (c), respectively.

of both partial beams, which interfere at the output resulting in a signal that depends on the phase difference. Therefore, relative changes in the arms lengths (caused by a GW) are imprinted in the detected power.

Figure 1.3 shows a schematic of the influence of a GW on a Michelson interferometer. While Fig. 1.3 a. shows the interferometer in the original state, Fig. 1.3 b. and c. show the deformation of the interferometer's arms in analogy to Fig. 1.1. The construction of large dimension Michelson interferometer GWs like GEO600 [1.15] and LIGO [1.16] started in the 1990s. In 2002 the first science run of the two detectors took place [1.17].

The 1st generation of interferometric GWs already exceeded the sensitivity of the bar detectors. Additionally, the high sensitivity of interferometric GWs has a bandwidth of about 1 kHz, much larger than the bar detectors. The 2nd generation of interferometric GWs is currently being commissioned while the 3rd generation is in the design phase. An overview over the sensitivity curves of detectors of all three generations can be found in [1.18]. The total sensitivity and its components for the Advanced LIGO detector is shown in [1.18]. A limiting noise source in the whole frequency range above 10 Hz is *quantum noise*. In the frequency range between 80 Hz and 800 Hz additionally *coating Brownian noise* becomes significant. At frequencies below 80 Hz *suspension thermal noise* adds and at even lower frequencies the gravity gradient and seismic noise components become significant for the total noise.

This work aims to reduce the following noise sources for future GWs:

- *Quantum noise*: Quantum noise is composed of *shot noise* (SN) and *radiation pressure noise* (RPN) [1.21, 1.22]. Above a few hundred hertz, SN which originates from statistical fluctuations within the laser light due to its quantum nature is dominating. The counting statistics also cause fluctuations in the test-mass position due to radiation pressure. This RPN shows a $1/f^2$ frequency behavior, while SN has a white (flat) spectrum. Both noise sources are depending on the laser power. While the signal normed SN decreases with increasing laser power by $\sqrt{1/P}$, RPN increases with increasing laser power by \sqrt{P} .

1 Introduction

- *Thermal noise*: Thermal noise occurs in GWDs as *coating* and *substrate thermal noise* of the test-masses, *thermo refractive noise* in transmitting optics such as the detector's beam splitter and *suspension thermal noise*. Thermal noise of the test-mass and its coating causes a motion of the mirror surface. Thermo-refractive noise means fluctuations of the optical length of a transmitting substrate caused by temperature dependent material parameters as the thermo refractive coefficient dn/dT or the thermal expansion coefficient a_{th} . Suspension thermal noise induces vibrations of the suspensions and therefore also motions of the test-masses.

To further increase the sensitivity 3rd generation GWDs, the level of the limiting noise sources has to be decreased. One possibility to reduce shot noise is by increasing the laser power. Unfortunately higher power means an increasing thermal noise due to higher absorptions within the test-masses and the beam splitter. Another possibility is the implementation of squeezed light into GWDs as first discussed by C. Caves in 1981 [1.22] and already implemented in GEO600 [1.23] and tested in LIGO [1.24]. To reduce thermal noise, cooling the GWDs is a promising concept. KAGRA, a Japanese 2nd generation GWD, is already under construction and being planned to perform at a cryogenic temperature of 20 K [1.25]. The Einstein Telescope (ET), a European 3rd generation project, is currently in the design phase. To be able to exploit all advantages of possible sensitivity enhancements, a so called xylophone configuration is considered for ET: For the high frequency detection band above a few ten Hz, a high power detector operating at room temperature (RT) is planned to reduce shot noise. In the low frequency detection band the thermal noise will be reduced in a cryogenic low power detector. For both detectors the implementation of squeezed light is planned to additionally reduce shot noise. The design sensitivity curves of both ET detectors are shown in Fig. 1.4.

In this work a cavity-based optical absorption measurement technique is presented, which was developed to measure small absorption connected with the GWD related noise sources discussed above. In the following an overview of this work and the performed absorption measurements is given:

- The photo-thermal self-phase modulation technique is an optical absorption measurement method based on thermally induced optical length changes within a cavity [1.26]. This method enables to measure small absorptions of bulk substrates and high reflective mirror coatings (Chapter 3). The theoretical background for applications of are the general functionality of cavities as well as their eigenmodes – the Gaussian beams (Chapter 2).
- In two proof of principle measurements exploiting the photo-thermal self-phase modulation technique, the applicability of the method is demonstrated. In the first one the absorption coefficient of a bulk LiNbO_3 substrate was measured [1.26]. The result is compared to values from literature and a cavity loss measurement. In the

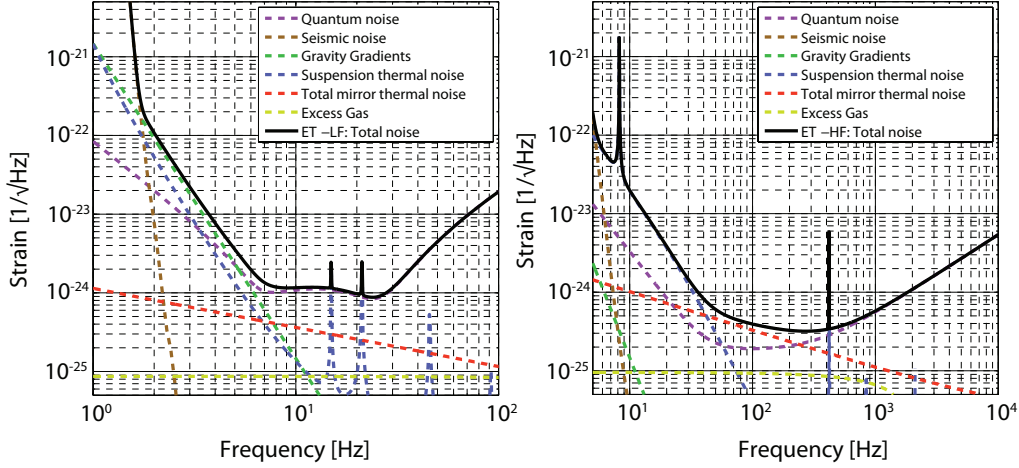


Figure 1.4: Fundamental noise contributions of the two xylophone detectors proposed for the Einstein Telescope (ET). For the high-frequency detection band (HF) a detector operating at high laser power of 3 MW in the detector arms is planned (a.), while in the low frequency detection band (LF) it is planned to use low power of 18 kW to optimize the conditions for cryogenically cooled test-masses [1.19]

second experiment the absorption of a high reflective mirror coating was measured and compared to results from calorimetric measurements [1.27] (Chapter 4).

- In the detection band between about 50 Hz and 800 Hz thermal noise of the test-masses is one of the limiting noise-sources for Advanced LIGO [1.18] and for ET HF (see Fig. 1.4 a., red dashed line), while for ET LF (Fig. 1.4 b. thermal noise is planned to be reduced by cooling the test-masses to cryogenic temperatures. To focus a large amount of thermal noise within a small frequency band, a high mechanical quality-factor (Q-factor) of the test-mass material is requested. Fused silica, which is used as a test-mass material in the 1st generation of GWDs and most of the 2nd generation detectors, has a high Q-factor at RT [1.28] that unfortunately decreases rapidly by several orders of magnitude towards cryogenic temperatures [1.29, 1.30] and makes fused silica unsuitable for cooled detectors. The high Q-factor of crystalline silicon at RT even increases towards cryogenic temperatures [1.30, 1.31], but its optical absorption is very high at the currently used wavelength of 1064 nm, which in turn makes it unsuitable for GWDs at this wavelength. The absorption decreases with increasing wavelength and is assumed to be very low around 1550 nm [1.32]. In this work optical absorption measurements on crystalline silicon at 1550 nm and RT were performed in a high intensity cavity (Chapter 5).
- Since the implementation of strong squeezing into GWDs reduces the quantum noise at high frequencies (shot noise), for ET 10 dB squeezed light injection are planned [1.20]. Up to 12.7 dB at 1064 nm and a sideband frequency of 5 MHz

1 Introduction

were already detected in squeezing experiments [1.33]. Generally, the squeezing factor is limited by optical losses as for example absorption and scattering within the setup [1.34]. When injecting the squeezed light into the GWD, losses caused by the GWD's input Faraday rotator, non-perfect dielectric coatings or a non-perfect photo-diode quantum efficiency additionally reduce the squeezing level. Since the losses caused by the GWDs are already reduced as much as possible, it is particularly important to keep the initial losses in the squeezed light source low. Periodically poled potassium titanyl phosphate (PPKTP) is a non-linear crystalline material that is used to generate second harmonic light and squeezed light. A low absorbing non-linear material for squeezed light generation is essential to generate strong squeezing and meet the demands of the 3rd generation of GWDs. Absorption measurements on PPKTP at 775 nm and 1550 nm are presented in Chapter 6.

- The sensitivity of the 2nd and 3rd generation of GWDs is expected to reach regions where radiation pressure noise (RPN) becomes significant, while it is no limiting noise source in the 1st generation. Recently, RPN was first measured experimentally [1.35] and there exist various experiments world wide, which work on the measurement and characterization of RPN [1.36–1.38]. Low mass silicon nitride (SiN) membranes are used in some of these experiments, which have to be cooled down to cryogenic temperatures to reach the required sensitivity to measure RPN [1.35, 1.38]. The cooling includes the membrane itself and implies low optical absorption within the membrane. Temperature measurements of membrane surfaces heated by a laser beam were performed using an infra-red camera. With this camera the relative absorption at discrete wavelengths in the region from 285 nm to 2 μ m was measured via the temperature. For an absolute calibration of the absorption, cavity loss measurements with several membranes varying in thickness were performed at the two wavelengths 1064 nm and 1550 nm (Chapter 7).
- Future GWDs as ET will at least partly operate at 1550 nm. Therefore the absorption characteristics of the commonly used fused silica and tantala ($\text{SiO}_2/\text{Ta}_2\text{O}_5$) high reflective coatings at this new wavelength are of interest. Also 1550 nm might give the chance for new coating materials which are unsuitable at 1064 nm. For the $\text{SiO}_2/\text{Ta}_2\text{O}_5$ coatings the tantala is the more critical of the two materials having higher mechanical loss [1.39] that has to be reduced for future GWDs. Replacing the tantala with silicon could not only reduce the mechanical loss, but also the number of necessary single layers per coating significantly [1.30] due to the much higher index of refraction of silicon. Optical absorption measurements on $\text{SiO}_2/\text{Ta}_2\text{O}_5$ and SiO_2/Si coatings at 1550 nm were performed and are presented in Chapter 8.
- The results of the experiments for future GWDs are summarized and discussed in the concluding chapter (Chapter 9).

- 1.1 A. Einstein
Die Grundlage der allgemeinen Relativitätstheorie
Annalen der Physik **49** 669 (54pp), 1916
- 1.2 A. Einstein
Näherungsweise Integration der Feldgleichungen der Gravitation
Akademie der Wissenschaften Sitzungsberichte **1916** 99 (10pp), 1916
- 1.3 B. F. Schutz
Gravitational wave sources and their detectability
Class. Quantum Grav. **6** 1761–1780, 1989
- 1.4 P. R. Saulson
Fundamentals of interferometric gravitational wave detectors
World Scientific Singapore **1** edition, 1994
- 1.5 P. Aufmuth, K. Danzmann
Gravitational wave detectors
New Journal of Physics **7** 202, 2005
- 1.6 C. Cutler, K. S. Thorne
An Overview of Gravitational-Wave Sources
arXiv:gr-qc/0204090v1 (40pp), 2002
- 1.7 T. Damour
General relativity and experiment: a brief review
Class. Quantum Grav. **9** 55, 1992
- 1.8 R. A. Hulse, J. H. Taylor
Discovery of a pulsar in a binary system
Astrophys. J. (Letters) **195** L51, 1975

Bibliography

- 1.9 J. Weber
Observation of the thermal fluctuations of a gravitational-wave detector
Phys. Rev. Lett. **17** 24, pp. 1228–1230, 1966
- 1.10 O. D. Aguiar
The Past, Present and Future of the Resonant-mass Gravitational Wave Detectors
arXiv:1009.1138 [astro-ph.IM]
- 1.11 P. Astone
Resonant mass detectors: present status
Class. Quantum Grav. **19** 1227–1235, 2002
- 1.12 G. A. Prodi, L. Conti, R. Mezzena, S. Vitale, L. Taffarello, J. P. Zendri, L. Baggio, M. Cerdonio, A. Colombo, V. Crivelli Visconti, R. Macchietto, P. Falferi, M. Bonaldi, A. Ortolan, G. Vedovato
Initial operation of the gravitational wave detector AURIGA
World Scientific, p. 198, 1998
- 1.13 W. Winkler, K. Maischberger, A. Rudiger, R. Schilling, L. Schnupp, D. H. Shoemaker
Proceedings of the Fourth Marcel Grossmann Meeting on General Relativity, pp. 621–630, 1986
- 1.14 B. C. Barish
Interferometric gravitational wave detectors
Nuclear Physics B (Proc. Suppl.) **138**, pp. 510–517, 2005
- 1.15 H. Grote (for the LIGO Scientific Collaboration)
The GEO 600 status
Class. Quantum Grav. **27** 084003, 2010
- 1.16 The LIGO Scientific Collaboration
LIGO: the Laser Interferometer Gravitational-Wave Observatory
Rep. Prog. Phys. **72** 076901 (25pp), 2009
- 1.17 The LIGO Scientific Collaboration
Detector description and performance for the First Coincidence Observations between LIGO and GEO
Nucl. Instrum. Methods Phys. Res. A **517** 154, 2004
- 1.18 S. Hild
Beyond the second generation of laser-interferometric gravitational wave observatories
Class. Quantum Grav. **29**124006 (9pp), 2012

- 1.19 By courtesy of S. Hild and IOP SCIENCE this figure was taken from:
 S. Hild et. al.
 Sensitivity studies for third-generation gravitational wave observatories
Class. Quantum Grav. **28** 9, p.10, 8. April 2011
[doi:10.1088/0264-9381/28/9/094013](https://doi.org/10.1088/0264-9381/28/9/094013)
- 1.20 S. Hild et. al.
 Sensitivity studies for third-generation gravitational wave observatories
Class. Quantum Grav. **28** 094013 ,2011
- 1.21 C. M: Caves
 Quantum-Mechanical Radiation-Pressure Fluctuations in an Interferometer
Phys. Rev. Lett. **45**, 75–79, 1980
- 1.22 C. M. Caves
 Quantum-mechanical noise in an interferometer
Phys. Rev. D **28** 8 1693–1708, 1981
- 1.23 The LIGO Scientific Collaboration
 A gravitational wave observatory operating beyond the quantum shot-noise limit
Nature Physics **7** 962–965, 2011
- 1.24 The LIGO Scientific Collaboration
 Enhancing the astrophysical reach of the LIGO gravitational wave detector by using
 squeezed states of light
 LIGO internal Document P1200041-v8
- 1.25 K. Somiya (for the KAGRA Collaboration)
 Detector configuration of KAGRA-the Japanese cryogenic gravitational-wave de-
 tector
Class. Quantum Grav. **29** 124007 (12pp), 2012
- 1.26 N. Lastzka, J. Steinlechner, S. Steinlechner, R. Schnabel
 Measuring small absorptions by exploiting photo-thermal self-phase modulation
Applied Optics **49** 28 5391-5398, 2010
- 1.27 J. Steinlechner, L. Jensen, C. Krüger, N. Lastzka, S. Steinlechner, R. Schnabel
 Photothermal self-phase-modulation technique for absorption measurements on
 high-reflective coatings
Applied Optics **51**, pp. 1156–1161, 2012
- 1.28 S. D. Penn, A. Ageev, D. Busby, G. M. Harry, A. M. Gretarsson, K. Numata K, P.
 Willems
 Frequency and surface dependence of the mechanical loss in fused silica
Physics Letters A **352** 3–6, 2006

Bibliography

- 1.29 C. Schwarz et al.
Proceedings of ICEC22-ICMC2008 edited by Chang H-M et al. **978-89-957138-2-2**, 2009
- 1.30 R. Schnabel, M. Britzger, F. Brückner, O. Burmeister, K. Danzmann, J. Dück, T. Eberle, D. Friedrich, H. Lück, M. Mehmet, R. Nawrodt, S. Steinlechner, B. Willke
Building blocks for future detectors: Silicon test masses and 1550 nm laser light
Journal of Physics Conference Series **228** 012029, 2010
- 1.31 D. F. McGuigan, C. C. Lam, R. Q. Gram, A. W. Hoffman, D. H. Douglass
Measurements of the Mechanical Q of Single-Crystal Silicon at Low Temperatures
Journal of Low Temperature Physics **30** 621–629, 1978
- 1.32 M. J. Keevers, M. A. Green
Absorption edge of silicon from solar cell spectral response measurements
Appl. Phys. Lett. **66** 174–176, 1995
- 1.33 T. Eberle, S. Steinlechner, J. Bauchrowitz, V. Händchen, H. Vahlbruch, M. Mehmet, H. Müller–Ebhardt, R. Schnabel
Quantum Enhancement of the Zero-Area Sagnac Interferometer Topology for Gravitational Wave Detection
Phys. Rev. Lett **104** 251102 (4pp), 2010
- 1.34 Y. Takeno, M. Yukawa, H. Yonezawa, A. Furusawa
Observation of -9dB quadrature squeezing with improvement of phase stability in homodyne measurement
Optics Express **15** 4321–4327, 2007
- 1.35 T. P. Purdy, R. W. Peterson, C. A. Regal
Observation of Radiation Pressure Shot Noise
arXiv:1209.6334v1, 21pp., 2012
- 1.36 P. Verlot, A. Tavernarakis, T. Briant, P.-F. Cohadon, A. Heidmann
Scheme to probe optomechanical correlations between two optical beams down to the quantum level
Phys. Rev. Lett. **102** 103601, 2009.
- 1.37 K. Borkje, A. Nunnenkamp, B. M. Zwickl, C. Yang, J. G. E. Harris, and S. M. Girvin
Observability of radiation–pressure shot noise in optomechanical systems
Phys. Rev. A **82** 013818, 2010

- 1.38 K. Yamamoto, D. Friedrich, T. Westphal, S. Goßler, K. Danzmann, K. Somiya, S. L. Danilishin, R. Schnabel
Quantum noise of a michelson-sagnac interferometer with a translucent mechanical oscillator
Phys. Rev. A **81** 033849, 2010.
- 1.39 G. M. Harry, A. M. Gretarsson, P. R. Saulson, S. E. Kittelberger, S. D. Penn, W. J. Startin, S. Rowan, M. M. Fejer, D. R. M. Crooks, G. Cagnoli, J. Hough, N. Nakagawa
Thermal noise in interferometric gravitational wave detectors due to dielectric optical coatings
Class. Quantum Grav. **19** 897–917, 2002

The absorption measurements presented in this work are all based on cavity setups using laser beams with Gaussian propagation and intensity profile. In this chapter the principles of cavity light-fields and intensities, the phase-dependence of these fields and different cavity geometries are introduced. The cavity eigenmodes are transverse electromagnetic (TEM) modes. The fundamental TEM₀₀ mode is a Gaussian beam and hence, Gaussian beam properties are required for the experimental part of this work and are also introduced in this chapter.

2.1 Cavity Fields and Powers

In this section relevant parameters of cavities are introduced, and the light powers in reflection and transmission of a cavity as well as within a cavity, which are important for the photo-thermal self-phase modulation technique, are deduced.

The most basic model of a cavity is composed of two reflecting surfaces, e.g. a so-called Fabry-Perot cavity as is illustrated in Fig. 2.1. A part of the input light field couples into the cavity through in-coupling mirror M_1 with reflectivity R_1 and transmission T_1 . The second mirror M_2 with reflectivity R_2 and transmission T_2 reflects a part of the light field, while the remaining part is transmitted. A standing wave develops between the two reflecting mirror surfaces.

In the following the reflected light field is deduced completely, beginning with some notation remarks:

The cavity mirrors are named M_i . The mirrors show intensity reflections R_i and intensity transmissions T_i . Accordingly their field coefficients are r_i and t_i with $r_i^2 = R_i$ and $t_i^2 = T_i$. For the calculation of the light-fields, the polar form of the coefficients is used

2 Cavity Theory



Figure 2.1: Schematic of a Fabry-Perot cavity: The light couples into the cavity through in-coupling mirror M_1 with reflectivity R_1 . The second mirror M_2 with reflectivity R_2 faces M_1 . Between the two mirrors a standing wave develops. The light field is transmitted by the end-mirror M_2 .

$$r_i = |r_i| e^{i\phi_{r_i}} = \sqrt{R_i} e^{i\phi_{r_i}} \quad t_i = |t_i| e^{i\phi_{t_i}} = \sqrt{T_i} e^{i\phi_{t_i}}. \quad (2.1)$$

If a light-field E_0 is reflected at the surface of the in-coupling mirror with reflectivity r_1 the reflected light-field is $E_{r_0} = -r_1 E_0$. This corresponds to the field left of M_1 in Fig. 2.1. During the first round-trip within the cavity, $t_1 E_0$ is transmitted into the cavity at the in-coupling mirror. At mirror M_2 with reflectivity r_2 the in-coupled field is reflected and $r_2 t_1 E_0$ remains within the cavity. Back at the in-coupling mirror a part t_1 of this field is transmitted, hence $r_2 t_1^2 E_0$ couples out. For the more general case of more than two mirrors further reflection coefficients r_i multiply to the light-field. Intensity round-trip losses α within the cavity of length L form a coefficient $e^{-\frac{\alpha}{2}L}$. Additionally, the round-trip phase (or mirror-detuning) coefficient $e^{-i\omega_0 L/c}$ is multiplied with the light-field. Here, ω_0 is the angular frequency of the beam and c is the speed of light. The resulting light-field in reflection after one round-trip forms to

$$E_{r_1} = t_1^2 r_2 (\times r_3 \times \dots) E_0 e^{-\left(\frac{\alpha}{2}L + i\omega_0 L/c\right)}. \quad (2.2)$$

In the following the parameter \tilde{r}_2 is used to summarize the round-trip losses and the reflectivities of all mirrors apart from M_1 :

$$\tilde{r}_2 = r_2 (\times r_3 \times \dots) e^{-\frac{\alpha}{2}L} \quad \tilde{R}_2 = R_2 (\times R_3 \times \dots) e^{-\alpha L}. \quad (2.3)$$

Using Eq. (2.3) the light-field after n round-trips yields

$$E_{r_n} = t_1^2 r_1^{n-1} \tilde{r}_2^n E_0 e^{-(i\omega_0 L/c)n}. \quad (2.4)$$

The total reflected field is the sum over an infinite number of round trips

$$E_r = \sum_{n=0}^{\infty} E_{r_n} = -E_0 r_1 + t_1^2 r_2 E_0 \sum_{n=0}^{\infty} \left((r_1 \tilde{r}_2) e^{-(i\omega_0 L/c)} \right)^n. \quad (2.5)$$

The sum is a geometric series with $((r_1 \cdot \tilde{r}_2) e^{-i\omega_0 L/c}) < 1$. Therefore the *total reflected light field* is

$$E_r = \left(-r_1 + \frac{t_1^2 r_2}{1 - r_1 \tilde{r}_2 e^{-i\omega_0 L/c}} \right) E_0. \quad (2.6)$$

That results in a *reflected intensity* $I_r \propto |E_r|^2$ with $I_0 \propto |E_0|^2$ of

$$I_r = \left| \frac{-1 + T_1 \sqrt{\frac{\tilde{R}_2}{R_1}} + \sqrt{R_1 \tilde{R}_2} e^{-i\omega_0 L/c}}{1 - \sqrt{R_1 \tilde{R}_2} e^{-i\omega_0 L/c}} \right|^2 R_1 I_0. \quad (2.7)$$

Likewise the remaining two light fields and intensities can be calculated. For the *intra-cavity light field* and *intensity* the results are

$$E_i = \frac{t_1 E_0}{1 - (r_1 \tilde{r}_2 e^{-i\omega_0 L/c})} \quad I_i = \frac{T_1 I_0}{\left| 1 - \sqrt{R_1 \tilde{R}_2} e^{-i(\omega_0 L/c)} \right|^2}. \quad (2.8)$$

For the *transmitted light field* and *intensity* the results are

$$E_t = \frac{E_0 t_1 t_2 e^{-i(\omega_0 L/c)}}{1 - r_1 \tilde{r}_2 e^{ikL}} \quad I_t = \frac{I_0 T_1 T_2}{\left| 1 - \sqrt{R_1 \tilde{R}_2} e^{-i(\omega_0 L/c)} \right|^2}. \quad (2.9)$$

For a simple Fabry-Perot cavity without losses ($T + R = 1$ and $\tilde{r}_2 = r_2$), Eq. (2.7) is plotted in Fig. 2.2a. for a varied phase $\omega_0 L/c = \delta = [-10, 10]$. For $\delta = n \cdot 2\pi$ the cavity is at resonance and resonance peaks occur. This corresponds to a cavity length change of $\lambda/2$ for a standing-wave cavity. The distance of two resonance peaks is the free spectral range of the cavity. In the frequency domain the free spectral range is given by

$$\text{FSR} = \Delta\nu_{\text{FSR}} = \frac{c}{L}, \quad (2.10)$$

where L is the round-trip length of the cavity, which is $2 \cdot d$ for a Fabry-Perot cavity with mirror distance d . The full width half maximum (FWHM) for the transmitted resonance peak (or in this case the full width half minimum, which is the same) is the line-width $\Delta\nu_{\text{LW}}$ of the cavity. The quotient of FSR and line-width is the finesse F of the cavity, which can be approximated from the mirror reflectivities and the round-trip loss

$$F = \frac{\Delta\nu_{\text{FSR}}}{\Delta\nu_{\text{LW}}} \approx \frac{\pi \sqrt{r_1 \tilde{r}_2} e^{-i\omega_0 L/c}}{1 - r_1 \tilde{r}_2 e^{-i\omega_0 L/c}}. \quad (2.11)$$

For $F > 20$ (which is the case for all experiments presented in this work) the error caused by this approximation is $< 0.1\%$ [2.2]. For the further simplification of

$$F \approx \frac{\pi}{1 - r_1 \tilde{r}_2 e^{-i\omega_0 L/c}} \quad (2.12)$$

2 Cavity Theory

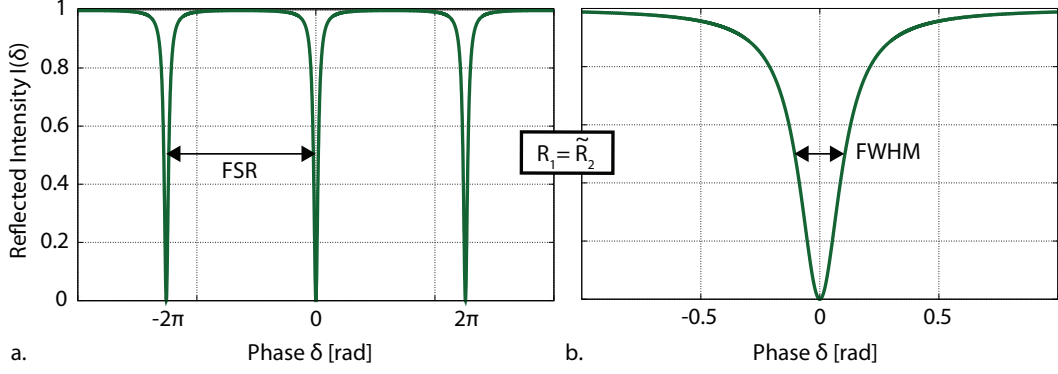


Figure 2.2: Laser power in reflection of the cavity depending on the round-trip phase: Resonance peaks occur. The distance of two resonance peaks is the FSR of the resonator (a.), the half width half minimum is the line width of the resonator (b.).

the error caused by the approximation is $< 1\%$ for $F > 160$ [2.2].

The cavity is said to be *impedance matched* for $R_1 = \widetilde{R}_2 = R$. If impedance matched, all light is transmitted into the cavity at resonance and the reflected light field vanishes. The peaks shown in Fig. 2.2 are for the impedance matched case. For $R_2/R_1 \neq 1$ at resonance a part of the light field is still reflected. Figure 2.3 a. shows the reflected power at resonance in % (= *impedance mismatch*) depending on the ratio R_2/R_1 for an incoupling reflectivity of 90%.

For impedance matching the intra-cavity intensity (from Eq. (2.8), right) reduces to

$$\frac{I_i}{I_0} = \frac{1}{1 - R}. \quad (2.13)$$

Comparing Eq. (2.13) and (2.12) it can be seen that F/π is an approximation for the intra-cavity power for an impedance matched cavity with $F > 160$.

For a non-impedance matched cavity the case of an overcoupled ($R_1 < \widetilde{R}_2$) and an undercoupled ($R_1 > \widetilde{R}_2$) cavity is distinguished. For an overcoupled cavity the intra-cavity power is higher than for an undercoupled one. Figure 2.3 b. shows the intra-cavity power buildup within a cavity with incoupling transmission $T_1 = 1000$ ppm in dependence of the quotient T_2/T_1 . The green line shows the accurate calculation using Eq. (2.8), the purple line shows the approximation F/π , which agrees with Eq. (2.8) in the impedance matched case. For a cavity with no losses, the transmitted signal is due to energy conservation the inversion of the signal shown in Fig. 2.2.

In principle for the measurement method presented in Chapter 3 any of these two signals contain all information that is needed (see Section 3.3.3). For most setups (in particular setups without power stabilization) it is easier to use the reflected signal instead of the transmitted one. While in reflection of the cavity the detected intensity off-resonance is a measure for the absolute power, there is no such measure in transmission. Therefore it can not be differed between input power and cavity losses. An additional

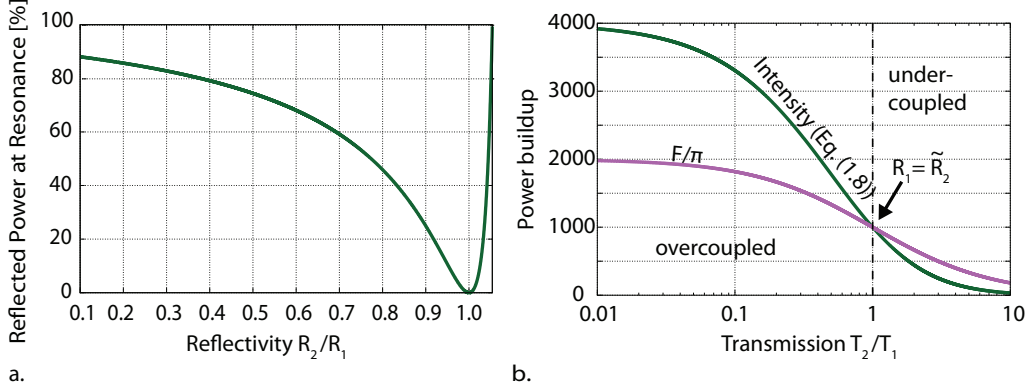


Figure 2.3: a. The green line shows the reflected power at resonance in % of the input power (impedance mismatch of the cavity) depending on the ratio R_2/R_1 for an input reflectivity of $R_1 = 90\%$. b. The green line shows the power buildup I_i/I_0 within a cavity with an in-coupling transmission of $T_1 = 1000$ ppm ($R_1 = 99.9\%$) depending on the quotient T_1/T_2 using Eq. 2.8. The purple line shows the approximation F/π for the intra-cavity power buildup. For an impedance matched cavity the approximation agrees with Eq. 2.8.

photo detector for power calibration is needed before entering the cavity. This makes a measurement in reflection of the cavity much easier.

2.2 Ringing Effects

Depending on the scan-velocity, the free spectral range and the finesse of a cavity, ringing effects can occur [2.3]. Ringing denotes the occurrence of a resonance peak with several maximums with exponentially decreasing amplitude as illustrated in Fig. 2.4c.

To explain ringing, a cavity locked at resonance is imagined where the laser is turned off. The light-field within the cavity circulates with speed of light c , hence the time needed for one round-trip in a Fabry-Perot cavity with length L is $t_{RT} = 2L/c$. A part of the light is transmitted passing the two mirrors and the amplitude E_0 decreases to $(1 - t_1 t_2)E_0$ after one round-trip. The field can be expressed as a differential equation

$$\frac{dE(t)}{dt} = \frac{-c}{2L} t_1 t_2 E(t). \quad (2.14)$$

The solutions of this equation show an exponential decrease of the field

$$E(t) = E_0 e^{\frac{-c}{2L} t_1 t_2 t}. \quad (2.15)$$

This exponential decrease occurs for a cavity with constant length. In our case the cavity length is scanned with a velocity v , so the length is time-dependent. For an external lengthening of the cavity the time-dependent length is $L(t) = L + vt$ with an also time-dependent round-trip time of $t'_{RT} = 2(L + vt)/c$. Therefore, the phase of the

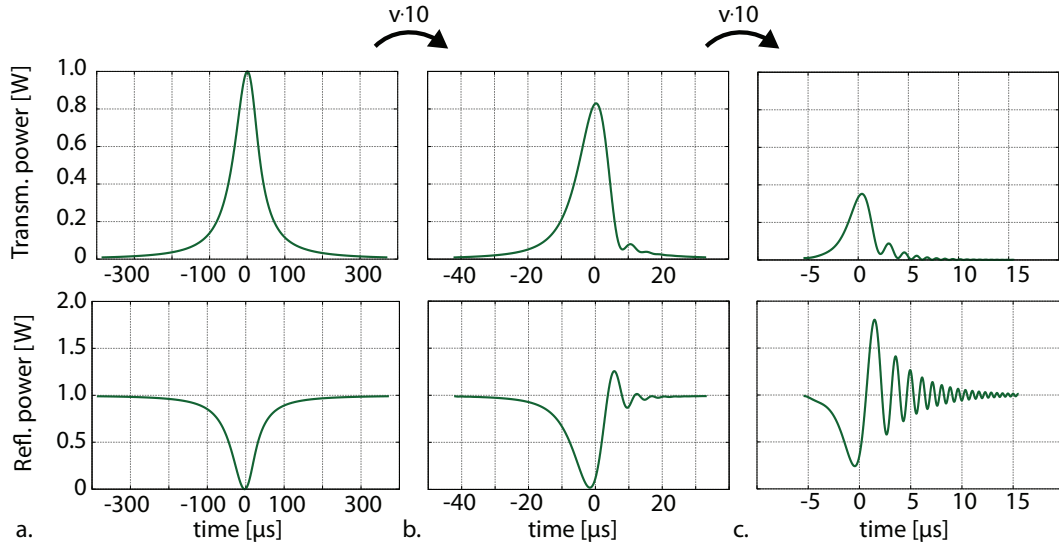


Figure 2.4: Resonance peaks for a cavity with $F \approx 7800$ and 0.42 m round-trip length. a., b. and c. each show transmitted and reflected resonance peaks. From a. to b. only the scan velocity was increased by a factor of 10 and ringing becomes visible. While the main maximum of the transmitted peak decreases, in reflection a maximum occurs that exceeds the input power. c. shows resonance peaks for a further scan velocity increase by a factor of ten. The ringing effect increases and an exponential decrease of the ringing amplitude with time becomes visible.

circulating field is constantly changed due to this length change and cannot interfere constructively at any time. For fast scan-velocities or long decay-times of the intra-cavity light field (high finesse or large L) the field oscillates between constructive and destructive interference.

Figure 2.4 shows an example of transmitted and reflected resonance peaks for a cavity with high finesse of $F \approx 7800$ at different scan frequencies. The input power was chosen to be 1 W, the cavity round-trip length is $L = 0.42$ m and $R_1 = \tilde{R}_2$. For Fig. 2.4 a. the scan frequency was 50 Hz with a scan amplitude of 1.68 % of an FSR resulting in the time-axis shown in the figures (the cavity line-width is 91 kHz). The reflected resonance peak reaches zero at resonance, while all light is transmitted. The peaks are symmetrical and no ringing occurs. Figure 2.4 b. shows transmitted and reflected resonance peaks for identical cavity parameters, only the scan velocity was increased by a factor of ten. The transmitted peak shows further maximums, while the main maximum reaches only about 80 % of the input power. The reflected peak does not reach zero at resonance anymore, while a maximum occurs that exceeds the input power. Another increase of the scan rate by a factor of ten is shown in Fig. 2.4 c. which increases the effect already recognizable in Fig. 2.4 b. furthermore. The transmitted light at resonance is decreased to less than 40 % of the input power, while the power of the first maximum of the reflected peak exceeds the input power almost by a factor of two. The ringing effect is more

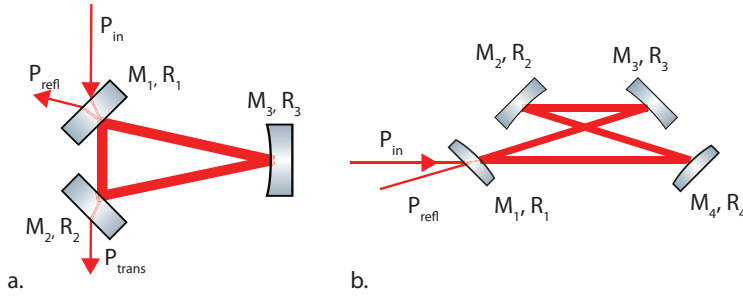


Figure 2.5: Examples of cavities based on three or more mirrors: a. shows a three-mirror ring-cavity, b. shows a bow-tie cavity, which consists of four mirrors.

distinctive and an exponential decrease of the ringing amplitude becomes visible.

In the experiment, ringing effects are obstructive for direct finesse measurements using the ratio $\Delta\nu_{\text{FSR}}/\nu_{\text{LW}}$ (see Eq. (2.11)). For resonance peaks where ringing effects occur, the finesse can be measured via the ratio of the first two transmitted power maximums I_1/I_2 and their time distance Δt (see [2.3]).

2.3 Traveling-Wave Cavities

Cavities consisting of three or more mirrors can form so-called ring-cavities. An advantage of these topologies is, that due to the angle of incidence differing from 0° the reflected beam is automatically separated from the incoming beam. Therefore the reflected beam can be detected easier without having to be elaborately separated from the incoming beam and no parasitic cavity can form within the in-coupling mirror. No standing wave is formed, but the light continuously travels around in the cavity. These cavities are also called traveling-wave cavities. Figure 2.5 shows two examples of cavities consisting of more than two mirrors. In Fig. 2.5a. a three mirror cavity is shown which is often used as a pre-mode cleaner [2.4]. This type of cavity was used in this work for the coating absorption measurements presented in Chapters 4 and 8. Figure 2.5b. shows one option for a four mirror cavity, a so called bow-tie setup. This version of a cavity was used for the PPKTP absorption measurements at 1550 nm presented in Chapter 6.

For the simulation presented in Chapter 3 a setup of more than two mirrors can simply be transferred to the Fabry-Perot cavity design by halving the round-trip (and bulk substrate) length.

2.4 The Gaussian Beam

The calculations in the previous sections assume plane waves. Actually, cavity Eigenmodes are TEM modes and the fundamental TEM_{00} mode is a so-called Gaussian beam. Since cavities are used for lasers to generate the laser beam, the beam emitted by a laser is Gaussian (at least to a high percentage). Since several properties of the Gaussian beam and its propagation characteristics are used in the following chapters, they are summarized in this section.

2 Cavity Theory

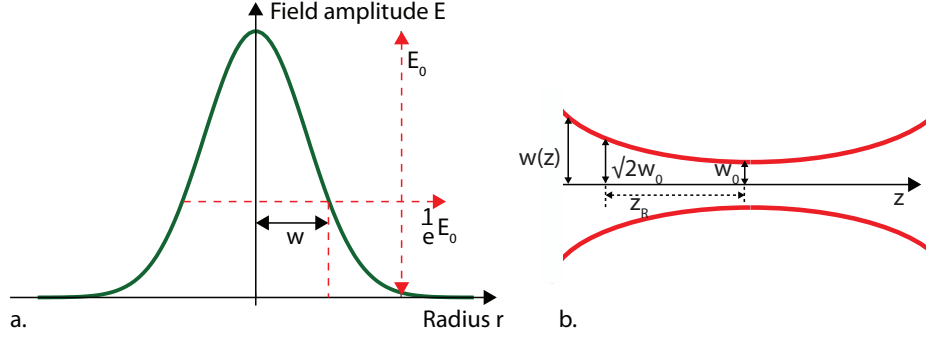


Figure 2.6: a. Gaussian amplitude distribution: w names the distance from the E -axis, at which the amplitude is decreased by a factor $1/e$. b. z_R shows the Rayleigh range, which is the distance at which the beam waist w_0 is increased by a factor of $\sqrt{2}$.

A Gaussian beam can be described by [2.1]

$$u(r, z) = \frac{w_0}{w} e^{-i(kz - \Phi) - r^2 \left(\frac{1}{w^2} + \frac{ik}{2R} \right)} \quad (2.16)$$

with

$$\Phi = \arctan \left(\frac{\lambda z}{\pi w_0^2} \right) \quad (2.17)$$

being the so-called Gouy-phase. r is the beam radius and z is the propagation axis of the beam. The propagation constant within the medium is $k = 2\pi/\lambda$, where λ is the wavelength of the laser beam. λ is related with the laser frequency f via $\lambda = c/f$. The angular frequency of the wave is $\omega_0 = 2\pi f$. Figure 2.6 a. shows a simple Gaussian distribution which is given by $u(r, z = 0)$ and illustrates the beam radius $w(z)$, which is the distance from the maximum amplitude E_0 to where the field amplitude dropped to $1/e$ of the maximum amplitude. This beam radius is given by

$$w(z)^2 = w_0^2 \left[1 + \left(\frac{\lambda z}{\pi w_0^2} \right)^2 \right]. \quad (2.18)$$

The radius of curvature of the beam $R(z)$ also depends on the propagation distance z and is given by

$$R(z) = z \left[1 + \left(\frac{\pi w_0^2}{\lambda z} \right)^2 \right] = z \left[1 + \left(\frac{z_R}{z} \right)^2 \right]. \quad (2.19)$$

The beam diameter is minimal at $z = 0$. At the beam waist $w(z = 0) = w_0$ the wave front of the beam is plane ($R(z = 0) = \infty$). The Gouy-phase introduced in Eq. (2.17) indicates an additional phase-shift of π when passing the beam's focus. In $R(z)$ also the Rayleigh range $z_R = \lambda/\pi w^2$ is introduced, which is the distance at which the beam waist w_0 is increased by a factor of $\sqrt{2}$. Figure 2.6 b. illustrates the Rayleigh range.

Bibliography

- 2.1 K. Kogelnik, T. Li, “Laser Beams and Resonators”, *Applied Optics*. Vol. **5**, No. **10**, pp. 1550-1567 (1966)
- 2.2 G. Heinzl, “Resonant Sideband Extraction – Neuartige Interferometrie für Gravitationswellendetektoren”, Diploma Thesis, Hannover (1995)
- 2.3 J. Poirson, F. Bretenaker, M. Vallet, A. Le Floch, “Analytical and experimental study of ringing effects in a Fabry-Perot cavity. Application to the measurement of high finesse” *J. Opt. Soc. Am. B*, Vol. **14**, No. **11**, pp. 2811-2817 (1997)
- 2.4 N. Uehara, “Ring Mode Cleaner for the Initial LIGO 10 Watt Laser” Internal LIGO Report, Stanford University, Stanford, California (1997)

The Photo-Thermal Self-Phase Modulation Technique

Measuring small absorptions with high accuracy is a challenge and necessary to characterize optical components applied in interferometric gravitational wave detectors. In this chapter an introduction about measurement methods to measure absorptions is given, which motivates the development of the photo-thermal self-phase modulation technique. This new technique is explained in the second section. It is based on a cavity setup exploiting the heating due to absorption to determine the absorption coefficient of a bulk substrate or the total absorption of a high reflective mirror coating using a time-domain simulation model.

3.1 Introduction

The easiest method to measure the optical absorption of any substrate type is a simple power measurement using a power meter or a photo-detector. Exploiting the Beer-Lambert law [3.1]

$$\frac{P_{\text{out}}}{P_{\text{in}}} = e^{-\alpha \cdot L} \quad (3.1)$$

the absorption coefficient α can simply be calculated by measuring the input power P_{in} and the power P_{out} behind the substrate of length L . Figure 3.1 shows an illustration of the Beer-Lambert law.

Errors of common power meters are in the order of some percent. Therefore only large absolute absorptions of some percent of the input power can be measured using this simple method. Large absolute absorptions are equivalent to large absorption coefficients or a long path within the absorbing substrate.

3 The Photo-Thermal Self-Phase Modulation Technique

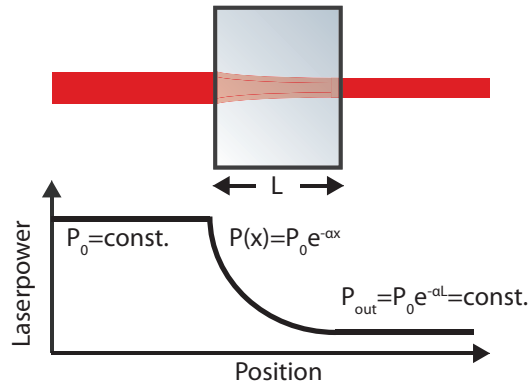


Figure 3.1: Schematic of the Beer-Lambert law. The constant power P_0 increases exponentially within the absorbing substrate.

Since the substrate length is limited in any case, passing the substrate several times, e.g. with a delay line setup where the beam passes the substrate several times can help to increase the sensitivity of the measurement. Figure 3.2 a. shows a schematic of a Harriott cell, a special optical delay line [3.2]. Figure 3.2 b. shows a photograph of a Harriott cell [3.3]. Since entering and leaving a substrate causes losses due to reflection each time (even with anti-reflection coatings), the application of delay lines for absorption measurements is restricted mainly to gas absorptions [3.4–3.6].

A special case of delay line is an optical resonator. Having a very well defined beam and entering the substrate always at exactly the same position, helps to minimize losses, for example by placing the substrate at Brewster's angle. To avoid as much losses due to reflection and scattering as possible a monolithic resonator is optimal, where the substrate's end surfaces are coated and therefore form the cavity mirrors. In principle for a resonator setup it is still possible to measure the input power and the transmitted power to determine the absorption coefficient. The problem occurring in this setup is, that the number of round-trips of the light field within the resonator is not exactly known in the first place. It can be estimated by a finesse measurement, but since the finesse does not distinguish between losses caused by absorption, scattering and mirror transmission this measurement is only accurate if the mirror reflectivities are exactly known. To separate absorption and mirror transmissions, the impedance mismatch of the cavity has to be measured additionally. The impedance mismatch separates the reflection of the in-coupling mirror from the out-coupling reflection plus remaining losses. Using each mirror to couple the light into the cavity once, the reflectivities of both mirrors can be determined and the round-trip loss can be obtained.

This round-trip loss measurement gives the same information as the power measurement. While the error of the power measurement was a few percent of the absolute power, the resonator setup can increase the sensitivity of the absorption measurement into the order of parts per million (ppm) loss per round-trip for an optimized setup, usually with a relative error of about 10%. The hitch is not to be able to separate

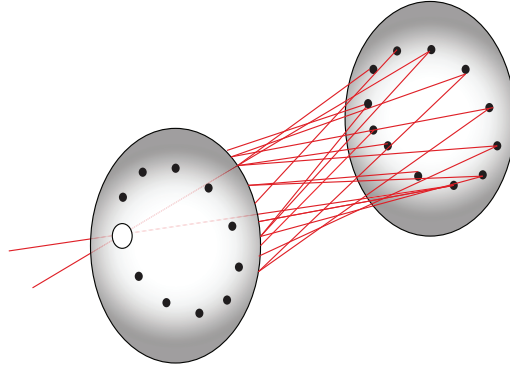


Figure 3.2: Schematic of a Herriott cell, a special type of delay line.

absorption and other loss sources.

To separate the absorption from other loss mechanisms, a completely different effect can be exploited: Absorption causes a heating of the substrate. This heating can be read out by directly measuring the temperature via negative temperature coefficient resistors (NTCs). This measurement method is called *calorimetric method* [3.7]. It reaches high sensitivities of the absorption coefficient in the order of ppm/cm with relative errors of about 10% of the measured absorption. Usually the sensitivity is limited by the available laser power.

Also exploiting heating due to absorption are the *z-scan* and *beam deflection methods* [3.8]. Figure 3.3a. shows a setup of the beam deflection method, which exploits the thermal lens, that is created within the substrate by a strong pump beam in case of a non-vanishing thermal expansion coefficient or a non-vanishing dn/dT . This thermal lens acts equivalent to an optical lens and causes a deflection of the probe-beam. The deflection is measured via a quadrant photo-diode and allows to conclude the absorption (depending on the setup, pump and probe beam can also be identical). Figure 3.3b. shows a setup of a z-scan method. Here, pump and probe beam differ in wavelength, so the photo detector is only sensitive to the probe beam. The substrate is shifted along the beam's propagation axis (z-axis), so the position of the pump beam's waist and therefore the resulting thermal lens changes. Caused by this position change of the thermal lens inside the substrate the beam parameters of the probe beam change and can be measured as a power change with a photo diode behind an aperture. For this setup, variations are also choosing pump and probe beam to be identical or simply switching the pump beam on and off instead of shifting the waist and substrate relative to each other. A third option is to create a thermal lens before entering a cavity and measuring the change of the mode-matching with the cavity's eigenmodes.

These methods can reach sensitivities up to $\alpha < 1$ ppm/cm of absorption. Since the sensitivity increases with the pump beam intensity, it is usually limited by the available laser power.

Based on these methods a technique was developed that uses the thermal lens effect

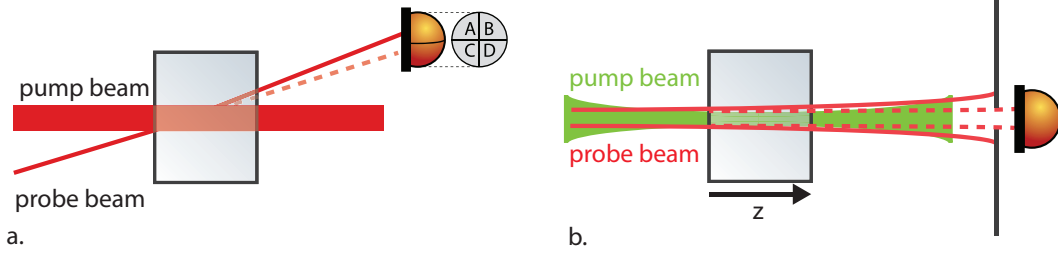


Figure 3.3: Absorption measurement method exploiting a thermal lens: a. The strong pump-beam causes a thermal lens. The weak probe beam is deflected by this lens. The deflection is measured by the quadrant photo diode. b. The thermal lens is caused by the pump beam. The probe beam having another wavelength, propagates along the pump beam. The photo diode that is sensitive only to the probe beam’s wavelength, detects a part of the beam behind an aperture. Moving the substrate around the pump beam’s waist, the detected power changes.

and at the same time exploits the power and sensitivity increase of a cavity setup. We call this method the *photo-thermal self-phase modulation technique*, which is described in the following Section 3.2.

3.2 Illustrative Explanation of the Photo-Thermal Self-Phase Modulation Effect

In this section the photo-thermal self-phase modulation effect as it can be obtained in the experiment is explained. In Subsection 3.2.1 we concentrate on the effect in bulk substrates, while in Subsection 3.2.2 the similar but not identical effect for absorption in mirror coatings is explained.

3.2.1 The Photo-Thermal Self-Phase Modulation Effect in a Bulk Substrate

Due to the absorption of laser power the absorbing substrate heats. For a sum of the thermo refractive index and the thermal expansion coefficient $dn/dT + \alpha_{th} \neq 0$, the optical length of the substrate changes. The following explanation of the method is for the in this work most occurring case of $dn/dT + \alpha_{th} > 0$. (For $dn/dT + \alpha_{th} < 0$ the explanation is equivalent.) Figure 3.4 a. shows a schematic of a substrate that expands due to heating caused by absorption. If this substrate is placed in an optical resonator, which is shown in Fig. 3.4 b., the optical length of the cavity changes due to the expansion and the round-trip phase ϕ_{cav} increases. In Fig. 3.4 c. the right mirror is periodically moved using a piezo electric transducer (PZT). Consequently the cavity length is changed and resonance peaks occur. At resonance the intra-cavity power increases (see Fig. 2.3). Since for small heating ΔT in comparison to the substrate temperature T_0 ($\Delta T \ll T_0$) ΔT increases approximately linear with the power, the sensitivity also increases linear

3.2 Illustrative Explanation of the Photo-Thermal Self-Phase Modulation Effect

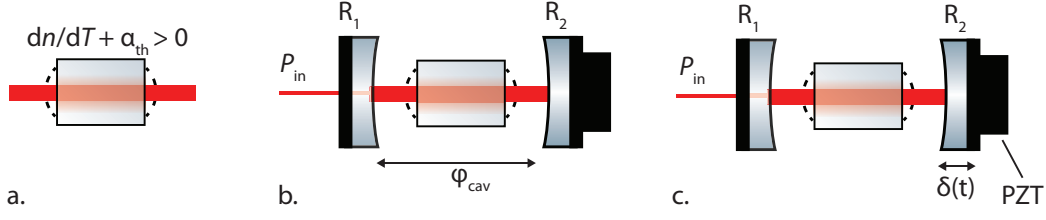


Figure 3.4: a. For $dn/dT + \alpha_{th} > 0$ heating due to absorption within a substrate causes an expansion of the optical length. b. If the substrate is placed in a cavity setup, the laser power within the substrate is increased and the beam passes the substrate several times. c. The cavity length can be modulated via a PZT to scan the cavity over its resonance. The photo-thermal self-phase modulation effect is the optical round-trip length change caused by the absorbed power at resonance.

with the power. Additionally, the beam passes the substrate twice at each round-trip. This makes a cavity a very phase-sensitive instrument for very small variations of the substrate's length.

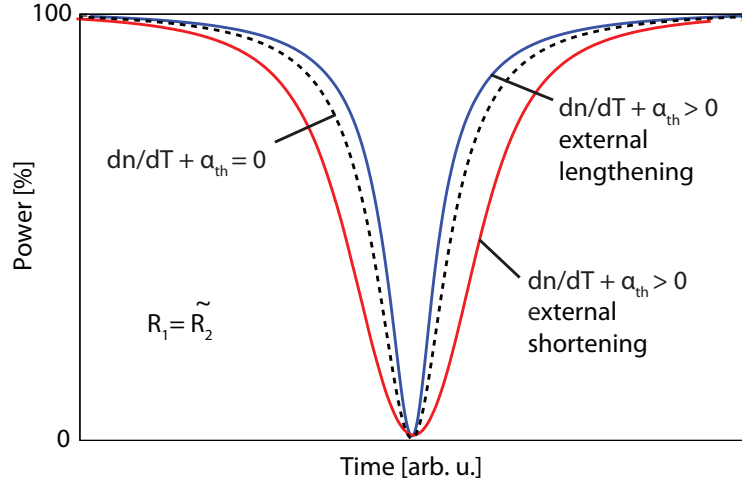
The occurring resonance peaks when scanning the cavity length can be detected with a fast photo diode. Resonance peaks in reflection of a cavity are shown in Fig. 3.5. The black dashed line shows a resonance peak that forms for an impedance matched cavity ($R_1 = \tilde{R}_2$) and no expansion due to heating $dn/dT + \alpha_{th} = 0$.

If the substrate heats at resonance due to absorption the resonance peaks deform and differ for an external shortening and lengthening of the cavity (*thermal effect*). An external lengthening of the cavity and the expansion of the substrate acts in the same direction and effectively adds resulting in a faster scan and therefore a shorter resonance. The resonance peak becomes more narrow (see blue peak in Fig. 3.5) compared to the original black dashed peak. An external shortening of the cavity and the substrate's expansion at resonance partly compensate. The resonance becomes longer and a broader resonance peak forms that is shown by the red line in Fig. 3.5. This self-induced modulation of the resonance width is the *photo-thermal self-phase modulation*.

To measure resonance peaks with significant thermal effect the cavity setup has to be optimized for the substrate under investigation. Usually the order of the absorption is known. Therefore the mirror reflectivities can be chosen near $R_1 = \tilde{R}_2$ which yields a high signal-to-noise ratio. For small absorptions, high intra-cavity power is required, which can be reached via high input power or a high finesse. Also the cavity length can be optimized. An optimum cavity length, radii of curvature of the mirrors and substrate length have to be found to maximize the optical length of the absorbing substrate and at the same time maximize the power density within the substrate by minimizing the beam waist.

For a given material and an optimized cavity setup the strength of the peak deformation is influenced by two parameters: The intra-cavity laser power and the scan frequency f . With increasing laser power the heat deposition in the substrate at resonance and

Figure 3.5: Cavity resonance peaks for $R_1 = \tilde{R}_2$: The black dashed peak forms for compensating parameters ($dn/dT + \alpha_{th} = 0$) or no heating due to low power. For $dn/dT + \alpha_{th} > 0$ (heating due to absorption in a bulk substrate) different peaks form for an external shortening (blue peak) and an external lengthening (red peak) of the cavity.



therefore the deformation increases. Decreasing the scan frequency results in a very similar effect. The cavity stays at resonance for a longer time and the absolute heat deposition increases. Figure 3.6 a. shows reflected resonance peaks with visible thermal effect for an arbitrary set of material, cavity, and scan parameters. For Fig. 3.6 b. no parameter apart from a doubled input laser power P was changed. The difference of broad and narrow peak (thermal effect) becomes stronger. For Fig. 3.6 c. the parameter set is also identical to the set used for Fig. 3.6a. This time the only changed parameter is a halved scan frequency f . Figure 3.6 d. shows the resonance peaks from Fig. 3.6 b. and c. which illustrates that the effect caused for an increasing P and for a decreasing f is similar, but not necessarily identical. These two parameters are the most important for the experiment to find the region where the absorption is measurable.

3.2.2 The Photo-Thermal Self-Phase Modulation Effect in a High-Reflective Mirror-Coating

For high reflective mirror coatings the resulting thermal effect is very similar to the effect described for a bulk substrate, while the reason for the effect is partly different.

For the following explanation we postulate a mirror substrate to be much thicker than the coating and an optimal heat conductivity from coating to substrate. This is given for the most common high reflective mirrors, where only some micrometers of coating material are applied to a substrate of at least a few millimeters thickness. This makes the coating dimensions and therefore their dn/dT and α_{th} negligible compared to the much larger substrate and we can concentrate on the properties of the mirror

3.2 Illustrative Explanation of the Photo-Thermal Self-Phase Modulation Effect

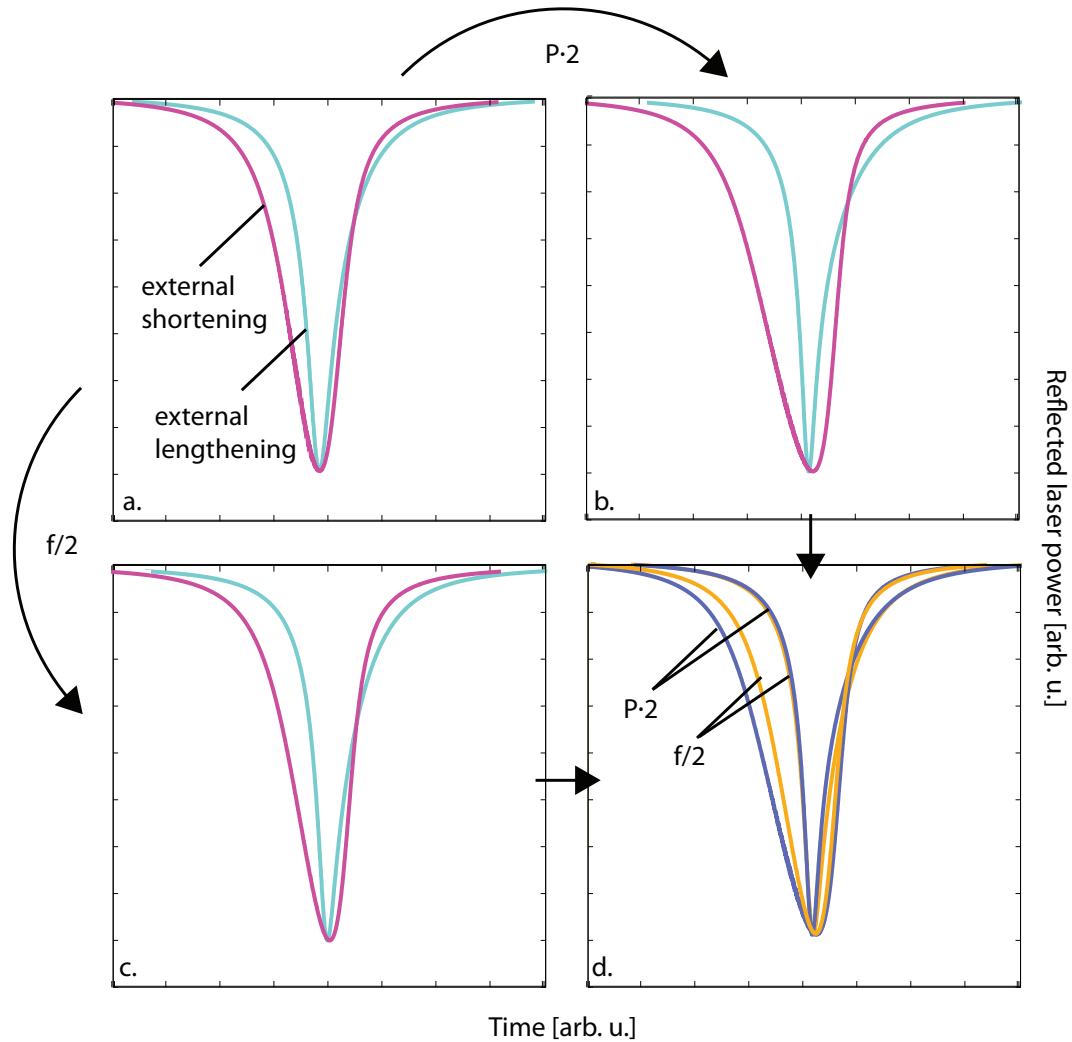


Figure 3.6: a. Resonance peaks with visible thermal effect for an arbitrary set of parameters. b. Resonance peaks for identical parameters as used for a., but doubled input power P . c. Resonance peaks for identical parameters as used for a., but halved scan frequency f . d. Resonance peaks from b. and c. for comparison.

substrate's material. Using such a mirror as a cavity mirror, the beam passes the in-coupling mirror substrate only twice when entering and leaving the cavity, while the coating sees the strongly increased intra-cavity power. Furthermore the incoming beam is constant and causes only a temperature offset, while only the reflected beam is time-dependent. Thus, we can neglect the substrate absorption. Combined, we can measure the coating absorption by examining the optical expansion of the substrate.

If a mirror coating within a cavity absorbs and its substrate expands, two effects occur. First, an $\alpha_{\text{th}} > 0$ causes an expansion of each cavity mirror into the cavity (see Fig. 3.7 a.). This expansion shortens the cavity round-trip length. This first effect is principally identical to the effect in bulk substrates, but since the expansion this time shortens the round-trip length, the peaks forming for an external shortening and lengthening of the cavity are exchanged.

The second occurring effect is a phase delay which the in-coupled beam gains due to dn/dT and α_{th} of the in-coupling mirror. This phase delay corresponds to a faster circulating field (from the in-coupled beam's point of view) or a shorter round-trip length. This second effect is illustrated in Fig. 3.7 b. by a mirror M_{mod} that modulates the phase of the beam before coupling into the cavity. For the second effect only the in-coupling mirror is relevant.

For most types of fused silica dn/dT is at least one order of magnitude larger than α_{th} . This makes the second effect dominating. However, the first effect becomes more important with every additional cavity mirror.

Regarding the measurement of coating absorption, two things have to be considered: For coatings directly applied to an absorbing intra-cavity substrate (for example a monolithic cavity), it cannot be differed between the coating absorption and the bulk absorption. For cavity mirror coatings the effect due to coating absorption and the effect due to absorption of an absorbing intra-cavity bulk substrate (partly) compensate, if both effects are in the same order of magnitude. In this case the coating absorption has to be measured separately in a setup without the bulk substrate.

3.3 The Time-Domain Simulation Model

The time-domain simulation model `tksim` was written by Nico Lastzka. A detailed description of the application's functionality and the simulation code can be found in [3.9]. Here, we will concentrate on a short summary of the analytical model of the heat distribution within an absorbing substrate in Section 3.3.1 and the fitting process used to derive the absorption results from experimental data in Section 3.3.3.

3.3.1 Theoretical Model

P. Hello and Y. Vinet developed an analytical model to simulate the heat distribution within a bulk substrate caused by optical absorption within the substrate or its coating [3.11]. In the following a short summary of the model for coating absorption is given.

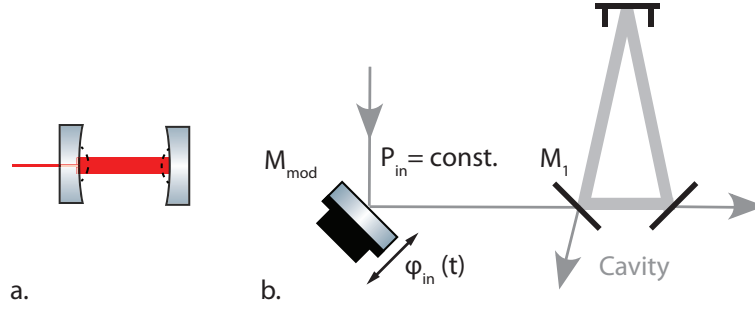


Figure 3.7: Absorption in the mirror coatings causes a heating of the substrate. (a) The thermal expansion of the mirror substrates shortens the cavity round-trip length. (b) $dn/dT + \alpha_{th} > 0$ within the in-coupling mirror causes a phase-delay of the in-coupled beam. This corresponds to an additional mirror that modulates the beam's phase before entering the cavity.

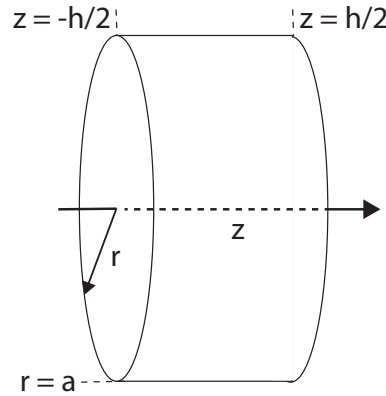


Figure 3.8: Schematic of the cylindrical test-mass with length h and radius a used for the time-domain model.

It is started with the assumption of a cylindric substrate with radius a and length h , which is illustrated in Fig. 3.8, a circular beam, and small heating

$$\frac{T_{\max} - T_{\text{ext}}}{T_{\text{ext}}} \ll 1, \quad (3.2)$$

where T_{\max} is the maximum temperature within the absorbing substrate and $T_{\text{ext}} \approx 300$ K.

The radiative heat transfer R_{ht} from a body with temperature T to a body with temperature T_{ext} is given by

$$R_{\text{ht}} = \sigma'(T^4 - T_{\text{ext}}^4), \quad (3.3)$$

where $\sigma' = \epsilon \times \sigma$. $\sigma = 5.670373 \times 10^8 \frac{\text{W}}{\text{m}^2\text{K}^4}$ is the Stefan-Boltzmann constant and $0 \leq \epsilon \leq 1$ the emissivity. The assumption from Eq. (3.2) allows an approximation using

3 The Photo-Thermal Self-Phase Modulation Technique

a Taylor-expansion that linearizes Eq. (3.3) into

$$R_{\text{ht}} = 4\sigma'(T_{\text{ext}}^3 \delta T), \quad (3.4)$$

with $\delta T = T - T_{\text{ext}}$.

Using the assumption of small heating (see Eq. (3.2)), Hello and Vinet start solving the steady state heat equation, which is homogeneous for no heating in the bulk substrate,

$$\rho C \frac{\partial T}{\partial t} - K \Delta T = 0. \quad (3.5)$$

Here ρ is the density of the substrate's material and C is the specific heat. The first summand of Eq. (3.5) describes the heating of the substrate with time, while the second summand describes the heat flow into the bulk substrate. Regarding this heat flow leads to three boundary conditions

$$-K \frac{\partial T_{\infty}}{\partial r}(a, z) = 4\sigma' T_{\text{ext}}^3 T_{\infty}(a, z), \quad (3.6)$$

$$-K \frac{\partial T_{\infty}}{\partial r}(r, -\frac{h}{2}) = \epsilon I(r) - 4\sigma' T_{\text{ext}}^3 T_{\infty}(r, -\frac{h}{2}), \quad (3.7)$$

and

$$-K \frac{\partial T_{\infty}}{\partial r}(r, \frac{h}{2}) = 4\sigma' T_{\text{ext}}^3 T_{\infty}(r, \frac{h}{2}), \quad (3.8)$$

where K is the thermal conductivity, r is the radius of the substrate and $I(r)$ is the intensity distribution of the incoming beam. Equation (3.6) describes the heat radiation of the cylinder barrel, while Eq. (3.7) and (3.8) describe the heat radiation at the absorbing coating (at $-h/2$) and the end surface of the cylinder (at $h/2$). T_{∞} is the temperature difference to the surrounding after infinite time and for the steady state $\Delta T_{\infty} = 0$.

A general solution of Eq. (3.5) can be expressed as

$$T(r, z) = \sum_m \left[A_m e^{k_m z} + B_m e^{-k_m z} \right] J_0(k_m r), \quad (3.9)$$

where J_0 is the 0th-order Bessel function (and the J_i are higher orders). k_m , A_m and B_m are parameters that can be determined from the boundary conditions Eq. (3.6)–(3.8). The first boundary condition Eq. (3.6) can be expressed as

$$K k_m J_1(k_m a) = 4\sigma' T_{\text{ext}}^3 J_0(k_m a), \quad (3.10)$$

and with $x = k_m a$ and $\tau = 4\sigma' T_{\text{ext}}^3 a / K$ it follows

$$x J_1(x) - \tau J_0(x) = 0. \quad (3.11)$$

$\zeta_m = k_m a$ is the m th solution of Eq. (3.11).

The functions

$$\left\{ J_0 \left(\zeta_m \frac{r}{a} \right), m \in \mathbb{N} \right\} \quad (3.12)$$

form an orthogonal basis for functions which are defined within $[0, a]$ (Sturm-Liouville problem) with the normalization constants

$$\frac{a^2}{2\zeta_m^2} (\tau^2 + \zeta_m^2) J_0(\zeta_m)^2. \quad (3.13)$$

The intensity distribution $I(r)$ of the incoming beam can also be expressed as a sum of these functions

$$I(r) = \sum_m p_m J_0 \left(\zeta_m \frac{r}{a} \right). \quad (3.14)$$

Using this expression, the second and third boundary conditions (Eq. (3.7) and (3.8)) form to

$$(\zeta_m - \tau) e^{-\zeta_m h/a} A_m - (\zeta_m + \tau) B_m = -\frac{\epsilon p_m a e^{-\zeta_m h/2a}}{K} \quad (3.15)$$

and

$$(\zeta_m + \tau) A_m - (\zeta_m - \tau) e^{-\zeta_m h/a} B_m = 0. \quad (3.16)$$

Solving these equations for A_m and B_m gives

$$A_m = \frac{\epsilon p_m a}{K} e^{-3\zeta_m h/2a} \frac{\zeta_m - \tau}{(\zeta_m + \tau)^2 - (\zeta_m - \tau)^2 e^{-2\zeta_m h/a}} \quad (3.17)$$

and

$$B_m = \frac{\epsilon p_m a}{K} e^{-\zeta_m h/2a} \frac{\zeta_m + \tau}{(\zeta_m + \tau)^2 - (\zeta_m - \tau)^2 e^{-2\zeta_m h/a}}. \quad (3.18)$$

From this the final result can be obtained to

$$T_\infty(r, z) = \sum_m \frac{\epsilon p_m a}{K} e^{-\zeta_m h/2a} \frac{(\zeta_m - \tau) e^{-\zeta_m (h-z)/a} + (\zeta_m + \tau) e^{-\zeta_m z/a}}{(\zeta_m + \tau)^2 - (\zeta_m - \tau)^2 e^{-2\zeta_m h/a}} J_0 \left(\zeta_m \frac{r}{a} \right). \quad (3.19)$$

The remaining coefficients p_m can be found assuming a Gaussian intensity profile of the heating beam of radius w and power P

$$I(r) = \frac{2P}{\pi w^2} e^{-2r^2/w^2}. \quad (3.20)$$

Using the formula

3 The Photo-Thermal Self-Phase Modulation Technique

Table 3.1: Material, geometric and beam parameters for the temperature distribution shown in Fig. 3.9

Simulation Input Parameters	Coating	Bulk substrate
Radius r	0.1 m	0.1 m
Power P_0	1 W	10 W
Beam waist w_0	2 cm	200 μm
Length L	0.1 m	0.1 m
Absorption coefficient α	100 ppm	100 ppm
Thermal conductivity K	1.38 W/(mK)	1.38 W/(mK)
External temperature T	300 K	300 K
Emissivity ϵ	1.0	1.0

$$p_m = \frac{2\zeta_m^2}{\underbrace{a^2(\tau^2 + \zeta_m^2)J_0(\zeta_m)^2}_{1/Eq. (3.13)}} \int_0^a I(r) J_0\left(\zeta_m \frac{r}{a}\right) r dr, \quad (3.21)$$

the result for $a \gg w$ is

$$p_m = \frac{P}{\pi a^2} \frac{\zeta_m^2}{(\tau^2 + \zeta_m^2)J_0(\zeta_m)^2} e^{-1/8 \zeta_m w^2/a^2}. \quad (3.22)$$

Figure 3.9 a. shows the steady state temperature distribution within a bulk substrate caused by coating absorption given by Eq. (3.19). The used material and beam parameters can be found in Tab. 3.1.

For absorption within the bulk substrate the heat equation Eq. (3.5) becomes inhomogeneous,

$$\rho C \frac{\partial T}{\partial t} - K \Delta T = \alpha I(r). \quad (3.23)$$

Solving this equation equivalent to Eq. (3.5) results in a temperature profile [3.11]

$$T_\infty(r, z) = \frac{\alpha a^2}{K} \sum_m \frac{p_m}{\zeta_m^2} \left[1 - \frac{2\tau \cosh(\zeta_m z/a)}{(\zeta_m + \tau)e^{\zeta_m h/2a} - (\zeta_m - \tau)e^{-\zeta_m r/2a}} \right] J_0\left(\zeta_m \frac{r}{a}\right). \quad (3.24)$$

The steady state temperature distribution caused by absorption within the substrate given by Eq. (3.24) is shown in Fig. 3.9 b. The used material and beam parameters can be found in Tab. 3.1. For a better resolution of the temperature profiles, input power and beam waist are different for Fig. 3.9 a. and b.

From the heat distribution, the thermal lens can be calculated to the phase ψ caused by dn/dT by integrating

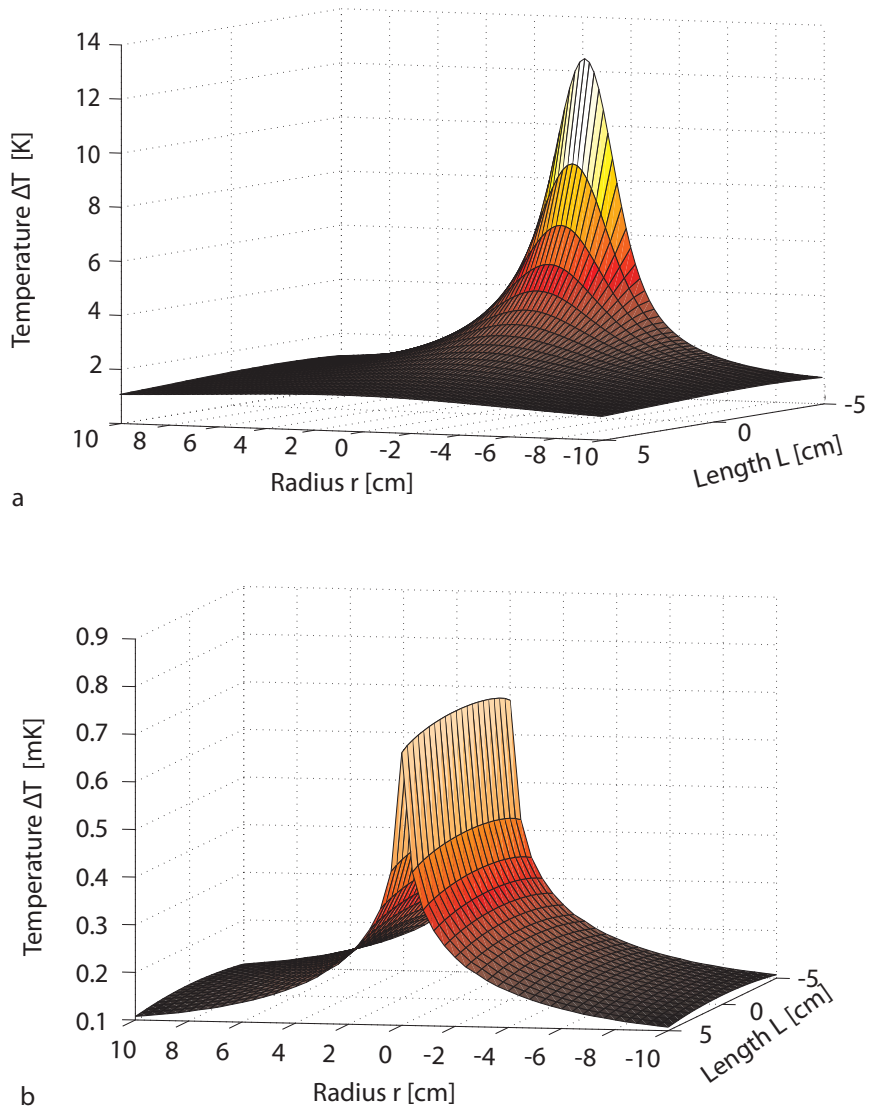


Figure 3.9: Temperature distribution caused by absorption within the coating (a.) and within the bulk substrate (b.) for a cylindrical substrate with 10 cm radius and 10 cm length.

$$\psi = \frac{dn}{dT} \int_{-h/2}^{h/2} T(r, z) dz. \quad (3.25)$$

For a scanned cavity setup, the temperature distribution and the resulting phase have to be calculated for each round-trip of the light field, since the temperature within the cavity changes constantly while the light field is being build up around resonance. The relevant time-domain calculations for the temperature evolution were derived by Hello and Vinet in their follow-up paper [3.12] and correcte dto the scanning cavity simulation by Nico Lastzka [3.9]. Reflected resonance peaks simulated for the substrate from Fig. 3.8 placed in a cavity with a finesse $F \approx 2000$ are shown in Fig. 3.10 a. Figure 3.10 b. shows the intra-cavity power around resonance, which is $P = 4.5 \text{ kW}$ at maximum. It can be seen that the deformation of the resonance peaks in Fig. 3.10 a. follows the shape of the intra-cavity power. In Fig. 3.10 c. the temperature distribution for a power of $P = 4.5 \text{ kW}$ within the substrate is shown after a defined time of $100 \mu\text{s}$, which is approximately the time needed to scan one resonance peak. Finally Fig. 3.10 d. shows the aberration of the beam caused by a_{th} and dn/dT when passing the substrate once for the temperature profile given in Fig. 3.10 c.

3.3.2 Input Parameters of the Simulation

To simulate the temperature and cavity resonance peaks several input parameters are required. An example input data file for the simulation program is shown in Tab. 3.2. In blue the unit of each parameter is given whenever the parameter is not dimensionless. The input file is split into the following blocks.

The first block [**Laser**] contains the beam parameters, which are the input power P , the wavelength λ and the laser beam waist w_0 .

The second block [**Cavity**] gives the cavity and scan parameters. The parameter m is the fraction of the light field mode matched to the cavity eigenmode. $R1$ and $R2$ are the intensity reflections of the input mirror and the effective reflection of the end-mirror containing all cavity losses and transmission of potential further mirrors. s is the distance of the two mirrors less the length of an intra-cavity substrate in case of a standing-wave cavity. For a ring cavity (three or more mirrors), s is the half round-trip length. $NFSR_i$ and $NFSR_d$ are needed for the calibration of the time-axis and gives the number of FSRs scanned per ramp side (i, d). ω_s is the frequency of the ramp signal for modulating the cavity length. Δ_{range} and Δ_{start} are the initial cavity detuning and scanning range in terms of the cavity line width. These last two parameters are not directly correlated to the experiment, but allow to simulate only the relevant part of the scanning range.

The block [**Measurement**] is mainly for calibration and plotting. shift_i and shift_d are for shifting the simulated data on the time axis to overlap it as exactly as possible with the experimental data. ref_val is the basis voltage level measured with the photo diode in reflection of the cavity that is used together with P for calibrating the y-axis

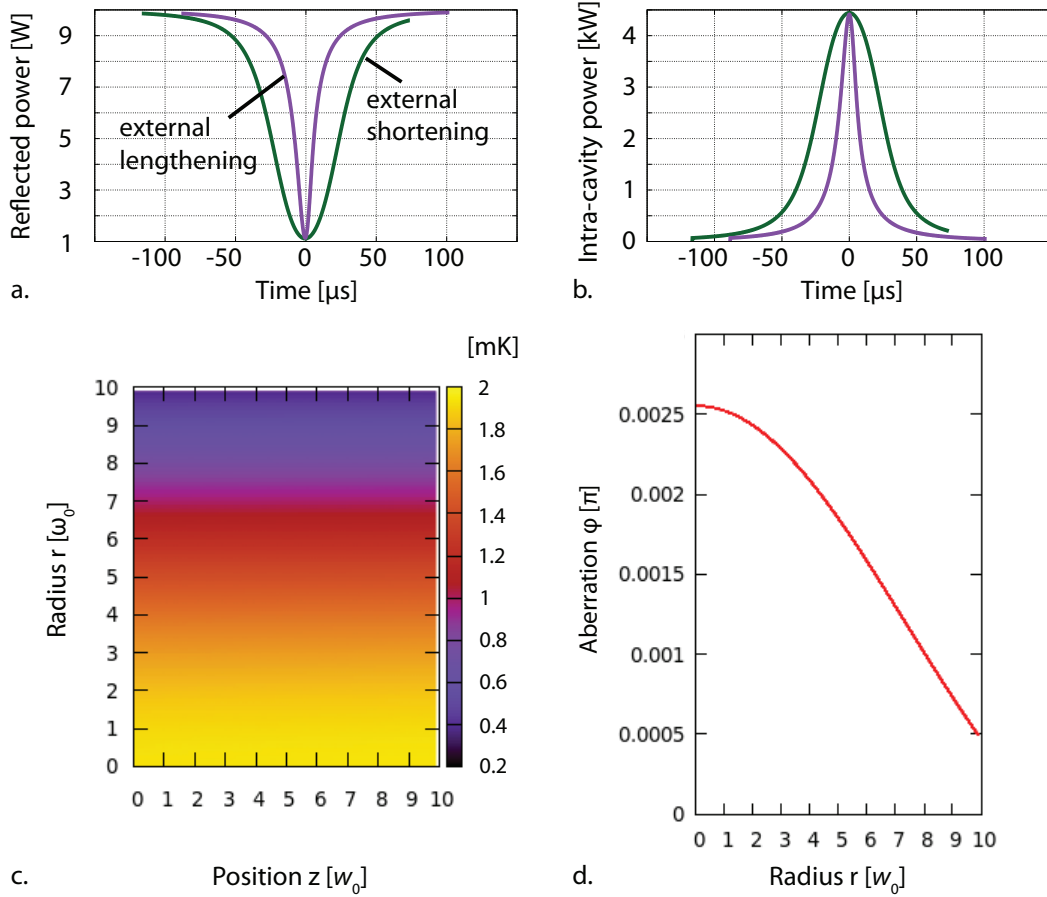


Figure 3.10: a. Simulated resonance peaks in reflection of the cavity for an external shortening (green, broad peak) and an external lengthening (purple, narrow peak) of the cavity. b. Simulated intra-cavity power around resonance for a finesse of $F \approx 2000$ ($R_1 = 99.9\%$, $R_2 = \text{HR}$, $\alpha = 100$ ppm/cm, $L = 10$ cm). c. Temperature distribution within the substrate after $100 \mu\text{s}$ for $P = 4.5$ kW at resonance. d. aberration of the beam passing the 10 cm substrate once caused by a_{th} and dn/dT .

3 The Photo-Thermal Self-Phase Modulation Technique

Table 3.2: Example of an input parameter file for the simulation program `tksim`. The mirror as well as the intra-cavity substrate material is fused silica.

```
[Laser]
P = 10.0 [W]
Lambda = 1064e-9 [m]
w0 = 200e-6 [m]

[Cavity]
mm = 1.0
R1 = 0.999
R2 = 0.998
s = 0.1 [m]
NFSR_i = 0.1
NFSR_d = 0.1
omega_s = 100.0 [1/s]
delta_start = -4 [line width]
delta_range = 8 [line width]

[Measurement]
shift_i = 0.0 [pt]
shift_d = 0.0 [pt]
ref_val = 1.0 [V]
every = 1
datafile = ./example.dat

[Mirror_1]
n = 1.5
dndT = 9.6e-6 [1/K]
rho = 2.2e3 [kg/m3]
k_th = 1.38. [W/(m·K)]
cw = 7704. [J/kg]
a_th = 5.2e-7 [1/(m·K)]
L = 0.1 [m]
R = 0.1 [m]
alpha = 0.0 [1/m]
alpha_coating = 10e-6 [1/coating]
epsilon = 1.0

[Control]
mstep = 100
pstep = 10
xRes = 1500
Tstep = 300
TEPS = 1e-6
T0 = 293. [K]
phiFactor = 2
term = wxt

[Substrate]
n = 1.5
dndT = 9.6e-6 [1/K]
rho = 2.2e3 [kg/m3]
k_th = 1.38. [W/(m·K)]
cw = 770. [J/kg]
a_th = 5.2e-7 [1/(m·K)]
L = 0.1 [m]
R = 0.1 [m]
alpha = 0.01 [1/m]
alpha_coating = 0.0 [1/coating]
epsilon = 1.0
```

of the measurement. The keyword `every` is used to plot only every n th measured data point. `datafile` imports the measurement data file.

The two blocks [`Substrate`] and [`Mirror_1`] contain the material parameters needed to simulate the temperature distribution within substrate or mirror. `n` is the index of refraction of the material at the specific wavelength. `dndT` gives the change of the index of refraction with temperature. `rho` is the density, `k_th` the thermal conductivity, `c_w` the specific heat and `a_th` the thermal expansion coefficient of the material. The absorption coefficient `alpha` is only relevant for the bulk substrate and usually negligible for the mirror substrate. The absolute absorption per coating is given by `alpha_coating`. The emissivity `epsilon` ($0 \leq \epsilon \leq 1$) can be assumed to be 1 for $w_0 \ll R$ which is the case in all experiments presented in this work, i.e. where the beam heats a section of the substrate that is much smaller than the substrate's radius and therefore far away from the substrate's surface.

The last block [`Control`] contains the following parameters: `mstep` and `pstep` are the number of steps used in the summation in Eq. (27) in [3.11]. The number of necessary steps can be found by increasing the number until the resulting temperature profile stops changing. To minimize the simulation time, both parameters should be chosen as small as possible. `xRes` sets the number of simulated points plotted on the x-axis. Every `Tstep` round-trip the temperature profile is calculated. Increasing this parameter can reduce the simulation time. `TEPS` defines the precision of the temperature calculation. `T0` is the temperature of the environment, `phiFactor` gives the number of cavity mirrors that expand into the cavity and therefore participate in changing the round-trip length. `term` sets the plotting terminal for gnuplot.

The parameters which are responsible for the temperature distribution within the absorbing substrate, are summarized into merged parameters in `tksim`. For a better understanding of the parameter correlations, Eqs. (3.26)–(3.30) show the merged parameters (mp). Since we can measure only a bulk absorption or a coating absorption in one setup, Eqs. (3.27) and (3.28) are not relevant at the same time.

$$\text{fsr} = \frac{c}{2(nL + s)} \quad (3.26)$$

$$\text{mp}_1 = \frac{4\alpha P}{RLk_{\text{th}}} \frac{2\pi}{\lambda} (\text{dndT} + a_{\text{th}}) \quad (3.27)$$

$$\text{mp}_2 = \frac{2\alpha_{\text{coating}} P}{R^2 L k_{\text{th}}} \frac{2\pi}{\lambda} (\text{dndT} + a_{\text{th}}) \quad (3.28)$$

$$\text{mp}_4 = \frac{\rho c_w}{k_{\text{th}}} \quad (3.29)$$

$$\text{mp}_{5/6} = \text{NFSR}_{i/d} \frac{2\omega_s}{\text{fsr}} \quad (3.30)$$

3.3.3 The Results

R_1 and \widetilde{R}_2 determine the intra-cavity power that is used to calculate the absorption coefficient from the thermal effect. For high reflectivities the intra-cavity power is very sensitive to small changes of the reflectivities. Since the mirror reflectivities are often not known with sufficient accuracy, and the round-trip losses are often not known at all, these parameters are fitting parameters.

For given cavity geometry and material parameters three quantities are fitted simultaneously. These are the reflectivity of the in-coupling mirror R_1 , the effective reflectivity of the end-mirror \widetilde{R}_2 , that contains all cavity round-trip losses, and for a thermal effect the absorption coefficient α of the intra-cavity substrate or the in-coupling coating. (If the absorption is known accurately, an optional material parameter can be fitted, that influences the thermal lens.) The full width half minimum (FWHM) of the resonance peak together with the calibrated time axis gives the finesse, which contains the product of all reflectivities and losses (see Eq. (2.11)). The impedance mismatch, which is the distance from peak minimum to zero at resonance (for a perfect mode matching) splits the product obtained from the finesse into the reflectivity of the in-coupling mirror and the effective reflection of the end-mirror (see Eq. (2.7) and Fig. 2.3 a.) Finally, the difference of the deformed peaks for the two different scan directions gives the absorption coefficient. This means, the three quantities can principally be determined independently from each other.

The merged parameters (mp) can be used as fitting parameters as well as single material and geometry parameters. This means that if in addition to the absorption coefficient for example dn/dT is unknown, using mp_1 , a product of α and dn/dT (for $dn/dT \gg a_{th}$) can be extracted. This product does not help to find the absorption, but if, for example, only measurements with thermal effects are available it allows to fit the resonance peaks and obtain the reflectivities.

While for most glasses even the thermally deformed reflected resonance peaks are vertically symmetric, for a lot of crystalline materials the resonance peaks become asymmetric. If the peak minimums are laid on top of each other, the peaks for an external increasing and decreasing of the cavity length intersect on the right flank. If existing, this intersection allows to fit the thermal conductivity k_{th} as a fourth parameter. Figure 3.12 shows such reflected resonance peaks for an external lengthening (dark green) and shortening (purple) of the cavity. From Fig. 3.12 a. to c. the thermal conductivity increases from $k_{th}=1$ W/mK to $k_{th}=3$ W/mK in steps of 1 W/mK. Since an increasing k_{th} decreases the resulting thermal effect, the absorption coefficient is also increased in a way that results in a constant thermal effect. It can be seen, that the intersection point of the two peaks on the right flank goes downwards from Fig. 3.12 a. to c. Figure 3.12 d. shows the resonance peaks from Fig. 3.12 a. to c. superimposed, which illustrates the identical thermal effect on the left flanks of the peaks as well as the changing interception point on the right flanks. Figure 3.12 e. zooms into the area around the interception point.

The simulation is fitted to the measurement by varying the fitting parameters and

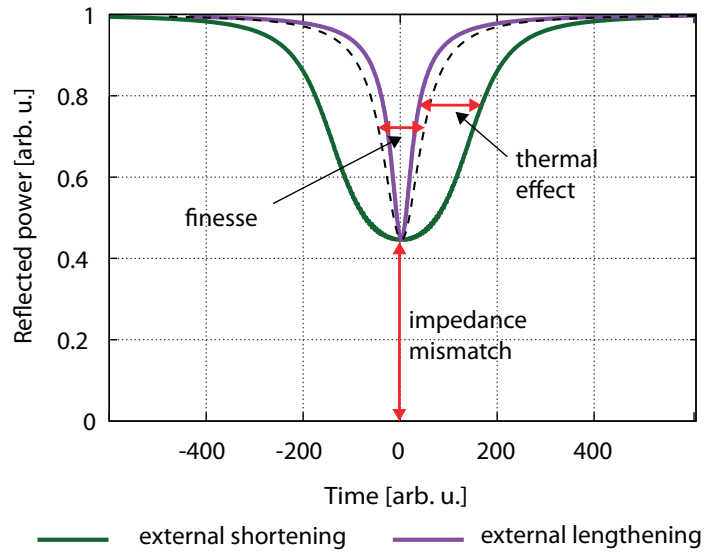


Figure 3.11: Reflected resonance peaks: The FWHM gives the finesse and therefore the product of the cavity reflectivities and losses. The impedance mismatch of the cavity splits the product into R_1 and \tilde{R}_2 . The thermal effect (difference of the peaks for different scan directions) gives the absorption coefficient.

minimizing the standard deviation. For the whole process from generating sets of fitting parameters to the final result there are various different options. In this work a Markov Chain Montecarlo (MCMC) [3.13] algorithm as well as a Nelder-Mead [3.14] algorithm was applied. For more detailed information see Sections 4.1 and 4.2.

3 The Photo-Thermal Self-Phase Modulation Technique

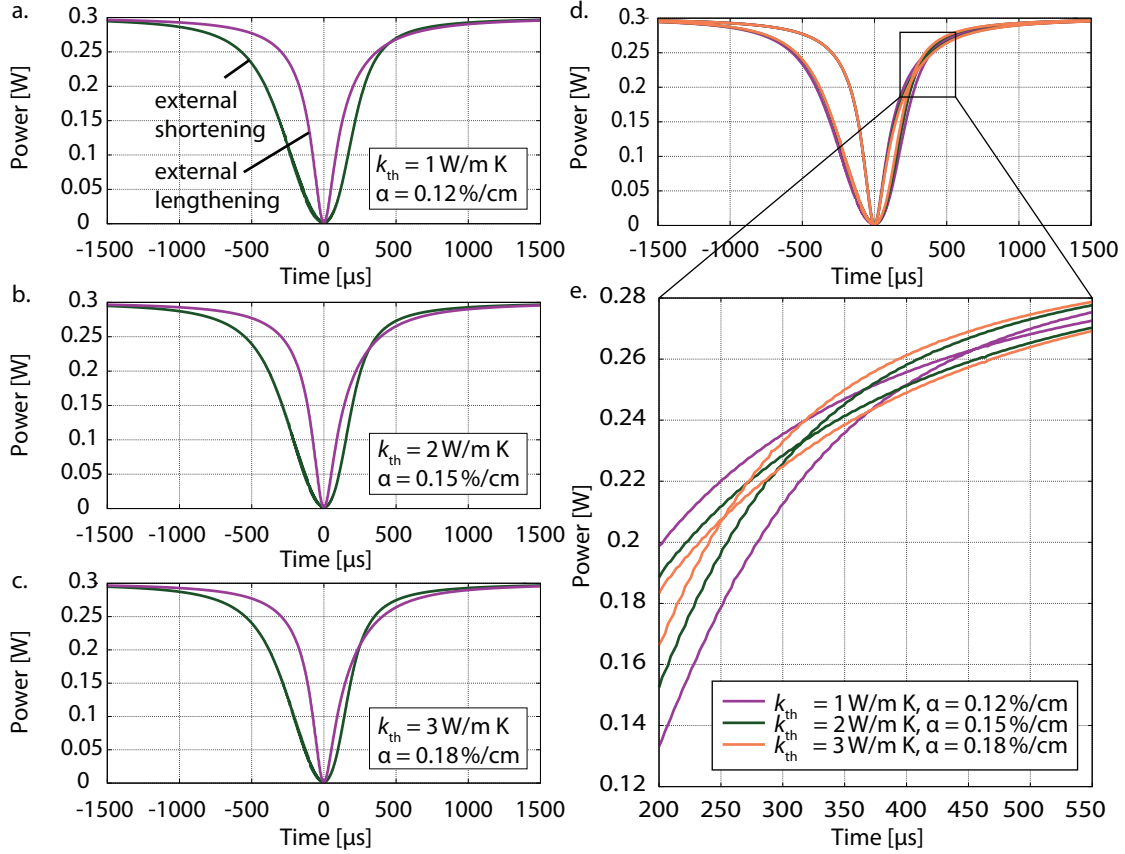


Figure 3.12: The Figures a.-c. each show resonance peaks for shortening (purple) and lengthening (green) cavity. The thermal conductivity was set to be $1 \text{ W/m} \cdot \text{K}$ in a., $2 \text{ W/m} \cdot \text{K}$ in b. and $3 \text{ W/m} \cdot \text{K}$ in c. For b. and c. the absorption coefficient was chosen to result in shapes of the resonance peaks as similar as possible to a, which is demonstrated in d. where all resonance peaks are overlapped. In d. a set of resonance peaks for shortening and lengthening cavity is illustrated in one color each ($k_{\text{th}} = 1 \text{ W/m} \cdot \text{K}$ and $\alpha = 0.12 \text{ \%/cm}$ in purple, $k_{\text{th}} = 2 \text{ W/m} \cdot \text{K}$ and $\alpha = 0.15 \text{ \%/cm}$ in green and $k_{\text{th}} = 3 \text{ W/m} \cdot \text{K}$ and $\alpha = 0.18 \text{ \%/cm}$ in coral). The shape of the peaks is very similar on the left peak flank while after the minimum the peaks start to diverge. In Figure e. the relevant part of the resonance peaks is enlarged. The intersection of the peaks moves in the direction of the minimum with increasing k_{th} .

- 3.1 W. Demtröder, “Experimentalphysik 2 - Elektrizität und Optik”, ISBN 3-540-65196-9, 2. Auflage (2002)
- 3.2 D. R. Herriott, H. J. Schulte, “Folded Optical Delay Lines”, *Applied Optics* **1965**, *4*, 883-889
- 3.3 www.lzh.de
- 3.4 J. S. Pilgrim, R. T. Jennings, C. A. Taatjes
Temperature controlled multiple pass absorption cell for gas phase chemical kinetics studies
Review of Scientific Instruments **68** *4*, pp. 1875–1878, 1997
- 3.5 D. Richter, A. Fried, B. P. Wert, J. G. Walega, F. K. Tittel
Development of a tunable mid-IR difference frequency laser source for highly sensitive airborne trace gas detection
Applied Physics B **75** pp. 281–288, 2002
- 3.6 J. B. McManus, M. S. Zahniser, D. D. Nelson
Dual quantum cascade laser trace gas instrument with astigmatic Herriott cell at high pass number
Applied Optics **50** *4*, pp. A74–A85, 2011
- 3.7 U. Willamowski, T. Groß, D. Ristau and H. Welling
Calorimetric measurement of optical absorption at 532 nm and 1064 nm according to ISO/FDIS 11551
Proc. SPIE **2870** 483, 1996
- 3.8 R. D. Snook, R. D. Lowe
Thermal lens spectrometry. A review
Analyst **120** pp. 2051–2068, 1995

Bibliography

- 3.9 N. Lastzka
Numerical modelling of classical and quantum effects in non-linear optical systems
PHD Thesis, Hannover, Germany (2010)
- 3.10 P. Hello
Compensation for thermal effects in mirrors of gravitational wave interferometers
Eur. Phys. J. D **15**, 373–383, 2001
- 3.11 P. Hello, J.-Y. Vinet
Analytical models of thermal aberrations in massive mirrors heated by high power laser beams
J. Phys. France **51** pp. 1267–1282, 1990
- 3.12 P. Hello, J.-Y. Vinet Numerical model of transient thermal effects in high power optical resonators'
J. Phys. France **3**, pp. 717–732, 1993
- 3.13 P. Gregory
Bayesian logical data analysis for the physical sciences
Cambridge University Press, Cambridge, United Kingdom, 2005
- 3.14 J. A. Nelder, R. Mead
A simplex method for function minimization
The Computer Journal **7** pp. 308–313, 1965

Demonstration of the Measurement Principle

In this chapter the feasibility of the photo-thermal self-phase modulation technique as a measurement method is demonstrated based on two experiments.

In the first experiment the absorption coefficient of a 7 mol% MgO-doped lithium niobate bulk substrate ($\text{MgO}:\text{LiNbO}_3$) at a wavelength of 1064 nm was measured. The results are in good agreement with former cavity loss measurements and with values known from literature. The experiment described in Sec. 4.1 is published in [4.1].

The second experiment exploited the photo-thermal self-phase modulation technique to measure the absorption of a $\text{SiO}_2/\text{Ta}_2\text{O}_5$ high reflection coating at a wavelength of 1064 nm. The obtained results are in excellent agreement with results from calorimetric measurements. Furthermore, in this second experiment the simulation process as well as the experimental execution was improved. The experiment described in Sec. 4.2 is published in [4.2].

The two experiments demonstrate the applicability of the photo-thermal self-phase modulation technique to measure the absorption coefficient of bulk substrates as well as the absorption of high reflection coatings.

In the following a short summary of the experimental implementation of the measurement principle is given. To obtain exact knowledge of the circulating power P_{circ} within the cavity not only the absorption coefficient α but also the reflectivity R_1 of the input mirror and the effective reflectivity \tilde{R}_2 of the end mirror were used as fitting parameters (see Section 3.3.3). To deduce a set of all three quantities including error bars, the following measurements are required:

- a calibration of the photodiode
- a characterization of the PZT that is used to modulate the cavity length

4 Demonstration of the Measurement Principle

- records of resonance peaks for lengthening and shortening cavity where a thermal deformation is clearly visible to quantify R_1 , \tilde{R}_2 and α

In this work such a set of measurements is referred to as *single measurement*. A *series of measurements* means multiple single measurements that differ in scan velocity or input power but are used to determine jointly one absorption result.

To vary the scan velocity the *scan frequency* is changed, which is the frequency of the ramp signal used to scan the cavity length via a piezo electric transducer (PZT) or via the laser wavelength. The scan frequency is a parameter that is easy accessible within the experiment, is accurately known (if for example generated by a function generator) and, since linear to the scan velocity, strongly influences the shape of the resonance peaks (see Fig. 3.6).

The scan frequency on its own is not a sufficient parameter, since the scanning time per resonance peak is needed. Therefore the scan frequency becomes meaningful in combination with the *scan amplitude*, the FSR of the cavity setup and a calibration factor NFSR giving the number of FSRs that can be scanned with the particular scan amplitude (see Section 3.3.2). The scan frequencies are used to name and distinguish the single measurements of a series. Since the scan amplitude was not changed within one series of measurements, the frequencies can also be used to compare scan velocities of measurements within a series. The scanning time per resonance peak can be learned from the plotted example measurements as in Fig. 4.3 a.–Fig. 4.3 d..

4.1 Measuring the Absorption Coefficient of a Bulk Substrate

The work presented in this Section is published in [4.1]. The results are partly published in [4.3].

In this section an experiment is presented, in which the absorption coefficient of a LiNbO₃ crystal in a hemilithic cavity for generating the second harmonic of a light field (SHG) with $F \approx 60$ was measured. The measured resonance peaks were simulated by the numerical time-domain simulation `tksim` (see Chapter 3) with R_1 , \tilde{R}_2 and α as fitting parameters. Applying a Markov Chain Monte Carlo (MCMC) algorithm, the best set of parameters including error bars was found by minimizing the variance of measurement data and simulation.

4.1.1 Experimental Setup

In Fig. 4.1 the experimental setup is shown. A Fabry-Perot cavity is formed by the input mirror M_1 and the curved high reflective (HR) coated end surface of the LiNbO₃ crystal M_2 . The design power reflectivities are $R_1 \approx 90\%$ and $R_2 > 99.8\%$. The input mirror is separated from the crystal by an air-gap of 24 mm. The plane surface of the crystal facing M_1 is anti-reflective (AR) coated. The geometric parameters of the cavity

4.1 Measuring the Absorption Coefficient of a Bulk Substrate

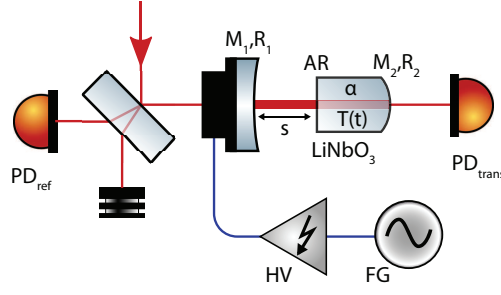


Figure 4.1: The experimental setup: A Fabry-Perot cavity is formed by the input mirror M_1 with reflectivity $R_1 \approx 90\%$ and the curved high reflective (HR) coated end surface of the LiNbO_3 crystal with a reflectivity of $R_2 > 99.8\%$. The cavity length is modulated with a ramp signal generated by a function generator (FG) and amplified by a high voltage amplifier (HV).

and the laser beam are listed in Tab. 4.1. To scan the cavity length, M_1 was moved periodically by a PZT. The PZT was fed with a ramp signal generated from a function generator and amplified by a high voltage amplifier. The transmitted and reflected resonance peaks of the cavity each were detected with a photo diode. It was ensured that the photo diode had a high enough bandwidth so that it did not influence the shape of the detected resonance peaks. The single-mode laser beam was mode matched to the fundamental mode of the cavity with an efficiency of more than 95%, coupling up to nearly 1500 mW into the cavity at resonance. The polarization of the input beam and the crystal temperature were detuned to avoid the generation of second harmonic light.

To confirm the results R_1 , \tilde{R}_2 and α from a single measurement, the measurement was repeated varying scan frequency and input power, altogether at three different frequencies with three different input powers each.

4.1.2 Calibration of the Time Axis

Most PZTs show a significant hysteresis. The expansion of the PZT per voltage depends on the voltage (position), scan direction (negative or positive expansion) and the scan frequency. Hence, the actual motion of the mirror M_1 that is moved by the PZT has to be calibrated for each frequency and separately for shortening and lengthening cavity. In the following chapters modulation sidebands were used for the calibration of the mirror motion and accordingly the time axis of the measured resonance peaks. For the calibration via sidebands, the sideband frequency should be at least approximately five times the line width, so the absorbing substrate can cool down before the sidebands become resonant. For the cavity line width of approximately 65 MHz in this experiment it was technically not possible to generate sidebands of high enough frequency.

For the time axis calibration in this experiment, eight resonance peaks positioned equally distributed on the ramp (modulation voltage) were detected for each frequency

4 Demonstration of the Measurement Principle

Table 4.1: Material and geometric parameters of the LiNbO₃ substrate and cavity geometric parameters used for the simulations.

Cavity geometric parameters		
airgap s	24 mm	
beam waist w_0	24 μm	
crystal length L	6.5 mm	
crystal radius R	2 mm	
Material parameters LiNbO ₃		Reference
index of refraction n	2.147	[4.4]
thermal refr. coeff. dn/dT	$38.5 \cdot 10^{-6} / \text{K}$	[4.5]
specific heat c	630 J/(kg K)	[4.6]
density ρ	4635 kg/m ³	[4.7]
thermal expansion a_{th}	$14.8 \cdot 10^{-6} / \text{K}$	[4.6]
thermal conductivity k_{th}	4.19 W/(m K)	[4.8]
material emissivity ϵ	1.0 ^a	
coating absorption α_{coating}	-	

^a $0.0 < \epsilon \leq 1.0$ are the boundaries for the thermal emissivity. For our systems the value of this parameter is not relevant since $R \gg w_0$.

and ramp-side. The line width of the resonance peaks depending on the peak position corresponds to dL_{LW}/dx , where L_{LW} is the deflection of M_1 and x the position. This measurement showed a divergence of the resonance peak line width of nearly a factor of two from ramp minimum to maximum which confirms the assumption of a strong hysteresis of the motion of M_1 . dL_{LW}/dx can be fitted via a fourth order polynomial whose qualitative shape is plotted in Fig. 4.2 a. Knowing the voltage per peak position as well as the voltage per time, which is shown in Fig. 4.2 b., the ramp position dependence of the line width can be used to calibrate the ramp signal and thereby the deflection per time of M_1 (see Fig. 4.2 c.). For this calibration method it was assumed that in the center of the ramp side the motion is linear with mean speed. Scanning more than one complete FSR, the fundamental modes served as frequency markers and the number of FSRs per ramp side (NFSRs) at each frequency could be determined.

Because of the elaborate calibration, only three different scan frequencies were used for the absorption measurements. For all measurements the resonance peaks were placed in the center of the ramp side with constant amplitude and offset. The resonance peaks were moved to the center of the ramp via a slight laser frequency variation. The determined NFSRs for each scan frequency can be found in Tab. 4.2.

The NFSRs enter the simulation to calculate the time that is needed to scan one resonance peak using the knowledge of the FSR and the ramp frequency.

4.1 Measuring the Absorption Coefficient of a Bulk Substrate

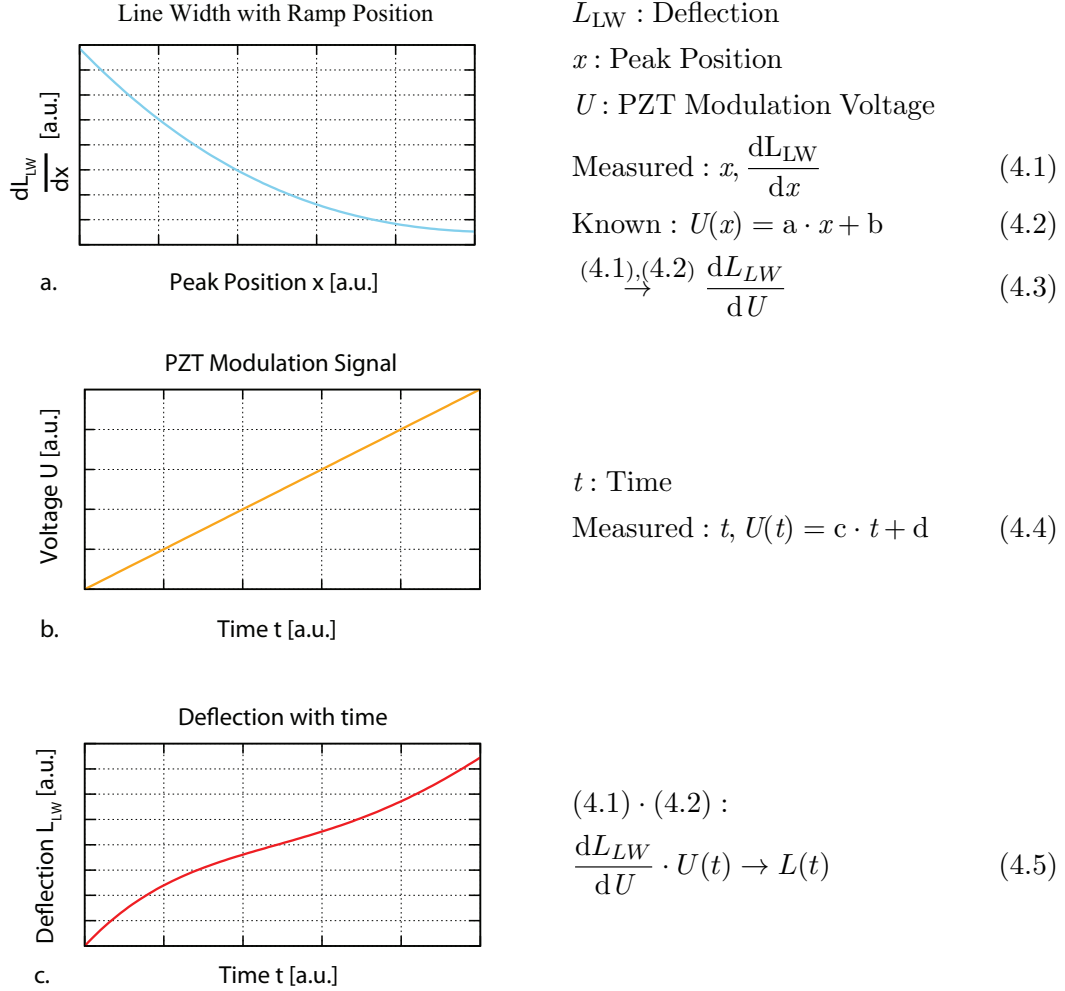


Figure 4.2: a. shows a fourth order polynomial fit of the measured line width of the resonance peaks depending on their position on the ramp dL_{LW}/dx . Knowing the PZT modulation voltage at every peak position leads to dL_{LW}/dU . b. Shows the PZT modulation signal per time which is a simple ramp signal. Only the increasing ramp side is shown. In Fig. c. the modulation signal was multiplied with dL_{LW}/dU resulting in $L_{LW}(t)$ which describes the deflection of M_1 per time.

4 Demonstration of the Measurement Principle

Table 4.2: Number of free spectral ranges (NFSRs) scanned per ramp side for increasing and decreasing ramp for each scan frequency and results obtained for R_1 , \tilde{R}_2 and α with errorbars for each single measurement.

ω_s in Hz	$NFSR_{i/d}$	P [W]	R_1	ΔR_1 $\times 10^3$	\tilde{R}_2	$\Delta \tilde{R}_2$ $\times 10^5$	α $\times 10^3$	$\Delta \alpha_{LN}$
1100 Hz	1.55/1.64	0.1	0.89668	6.46	0.99812	8.58	-	
		0.75	0.89585	5.37	0.99793	8.3	-	
		1.5	0.88532	3.62	0.99786	5.12	-	
110 Hz	1.825/1.87	0.1	0.8957	19.2	0.99802	26.6	-	
		0.75	0.90316	4.68	0.99814	1.27	6.016	0.8828
		1.5	0.88438	7.74	0.9978	12.2	5.5685	0.692
52 Hz	1.92/1.896	0.1	0.90153	5.26	0.99804	7.89	(10.247)	(4.39)
		0.75	0.89401	7.41	0.99797	11.5	6.4605	0.846
		1.5	0.892	11.8	0.99746	24.1	5.5672	0.824

4.1.3 Measurement and Data Analysis

Figure 4.3 a. and b. show examples of measured transmitted and reflected resonance peaks with a low input power of 100 mW. The peaks show no visible thermal effect and are identical apart from statistical fluctuations in the measurements due to for example acoustic noise or air fluctuations. The yellow curves form for a lengthening and the blue curves for a shortening cavity in each case. Figure 4.3 a. and b. show resonance peaks for identical conditions apart from a higher input power of 750 mW. Hence, the resonance peaks show a hysteresis caused by photo-thermal self-phase modulation.

Four of the nine performed measurements show no visible thermal effect and therefore were used only to deduce R_1 and \tilde{R}_2 . One measurement shows a very small thermal effect which results in large error bars for α while delivering good results for the reflections. The remaining four measurements show a clearly visible thermal effect and therefore were used to deduce R_1 , \tilde{R}_2 and α .

A Metropolis-Hastings MCMC algorithm [4.9] was used to minimize the variance of the deviation of simulation and measurement varying the input parameters R_1 , \tilde{R}_2 and α . This algorithm works as follows:

1. The MCMC algorithm starts with an initial set of input parameters $P = \{R_1, \tilde{R}_2, \alpha\}$. Resonance peaks with these input parameters are simulated by `tksim` and the variance σ^2 of the deviation of simulation and measurement is derived.
2. Within a specified uncertainty a new set of random parameters P' , the proposal state, is created.

4.1 Measuring the Absorption Coefficient of a Bulk Substrate

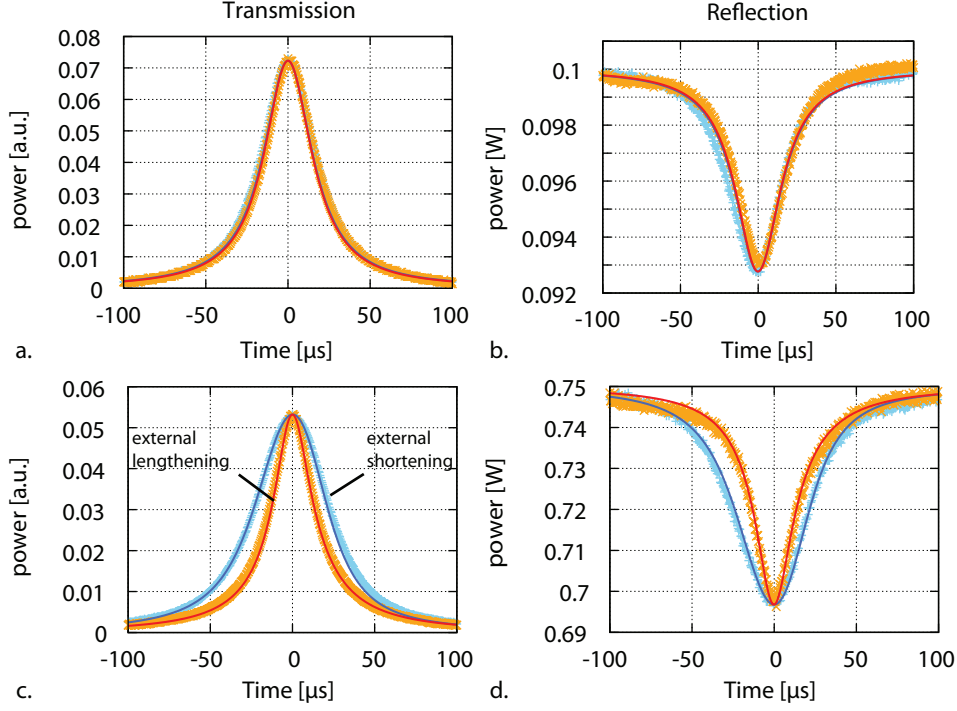


Figure 4.3: Example of measured (yellow/light blue) and simulated (red/dark blue) resonance peaks. Figures a. and b. show transmitted and reflected resonance peaks for low input power. No thermal effect is visible and the peaks are identical for shortening (yellow/red) and lengthening cavity (dark blue/light blue). Figures c. and d. show resonance peaks for high input power. A hysteresis due to absorption is clearly visible in measurement and simulation.

3. The quotient q of the old and new variance forms to

$$q = \frac{\sigma^2(P')}{\sigma^2(P_n)}. \quad (4.6)$$

4. • For $q \geq 1$, P' is dismissed. A new set of random parameters is created based on $P_{n+1} = P_n$.
- For $q < 1$ a random number x is drawn from a uniform distribution with $0 \leq x \leq 1$:

$$P_{n+1} = \begin{cases} P_n & \text{for } x < q \\ P' & \text{for } x \geq q \end{cases}$$

P_n is written into a list. Then jump to step two.

From this list, data chains emerge as shown in Fig. 4.4 for R_1 from the measurement with an input power of 750 mW and a scan frequency of 110 Hz. For every single measurement 10 000 sets of input parameters were created. A more demonstrative way to

4 Demonstration of the Measurement Principle

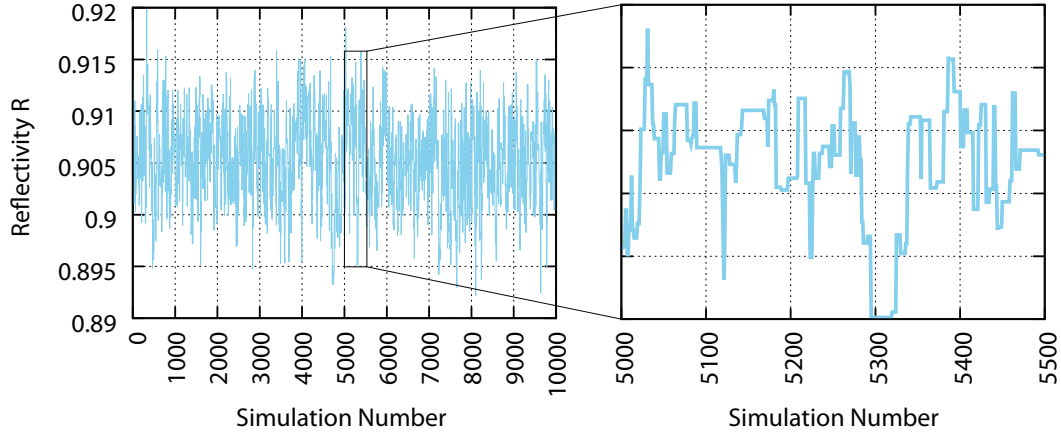


Figure 4.4: The light blue curve shows the values for R_1 from P_n that forms a data chain. A jump means P' was accepted, a constant value for some steps means $P_{n+1} = P_n$. With this method the area around the most likely result is scanned. In the left panel, the data chain is shown for all 10 000 steps created to obtain a result for the fitting parameters. In the right panel, a n extract of 500 steps is shown to make the jumps and constants more visible.

present these data is a histogram for each fitting parameter. A set of three histograms as shown in Fig. 4.5 is the result for every single measurement. The histograms' shape is very similar to a Gaussian distribution and the mean value and the standard deviation is given for results and error bars of the fitting parameters for all nine single measurements in Table 4.6.

4.1.4 Error Propagation

An important error source are possible errors in the input parameters. In the following their influence on the absorption coefficient α of a single measurement are considered. For this investigation the values of the simulation input parameters were individually changed and R_1 , \tilde{R}_2 and α were calculated. Based on this investigation the parameters could be grouped into two categories:

The first category contains the emissivity ϵ , the absorption of the substrate coatings α_{coating} , the index of refraction n , the intra-cavity air gap s , the substrate radius R and the beam waist w_0 , which all have very weak or even no influence on the result for the absorption for this setup. $0 < \epsilon < 1$ is irrelevant for this system, since the substrate is heated within the beam radius which is much smaller than the substrate radius. α_{coating} is much smaller than the substrate absorption and therefore can be neglected. A few percent change of n , s , R or w_0 showed a negligible effect on the result for the absorption coefficient.

The second category contains the parameters that strongly influence the absorption result. This are the input laser power P , the substrate length L , the thermal conductivity

4.1 Measuring the Absorption Coefficient of a Bulk Substrate

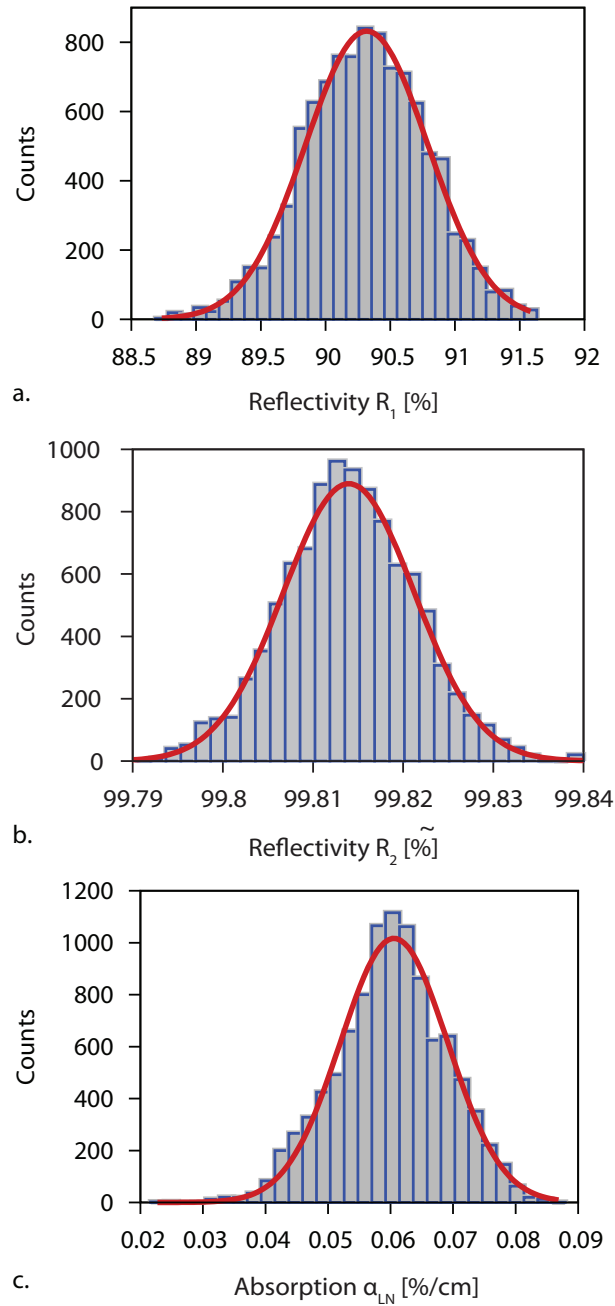


Figure 4.5: Chains (as shown in Fig. 4.4) obtained from a single measurement set were converted to histograms. For this measurement set the laser input power was 750 mW and the scan-frequency was 110 Hz. While R_1 (a.) and \tilde{R}_2 (b.) characterize the cavity, in Fig. c. the result for the absorption α_{LN} is shown. The histograms of the MCMC run are represented by the blue bars. The red lines are Gaussian fits to the histograms.

4 Demonstration of the Measurement Principle

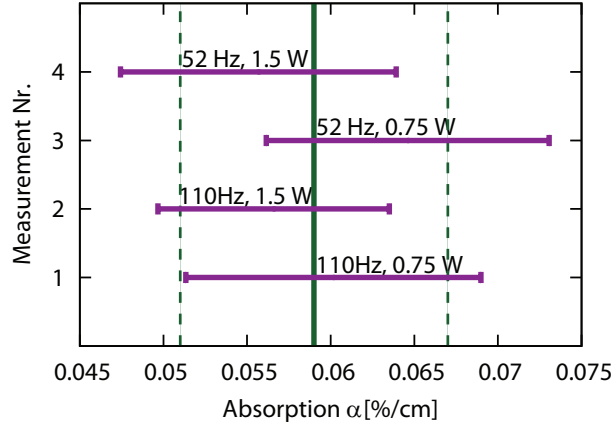


Figure 4.6: The red bars show the results from the MCMC algorithm for the absorption coefficient α and their statistical standard deviations for the four single measurements. The blue line marks the mean value of the four measurements with the mean standard deviation in dashed blue, which is $\alpha = (0.059 \pm 0.008) \text{ \%/cm}$.

k_{th} , the thermal expansion coefficient a_{th} , the thermo-refractive coefficient dn/dT , the density ρ and the heat capacity c_w . For a change of 4% of the input parameter the change in the result for the absorption is as follows: 3.6% for P , L and dn/dT , 2.8% for ρ and c_w , 1.6% for k_{th} and 1.4% for a_{th} . Assuming that the measured cavity geometric parameters and the material parameters from literature are statistically independent from another error on the final result for the absorption coefficient α .

4.1.5 The Final Results

The final results for the parameters are the mean values of the single results and their error bars. In Fig. 4.6 the four single results for α are shown in red and the mean value and error bars of all four results are shown in blue. The mean value of the absorption coefficient at 1064 nm is $\alpha_{\text{LiNbO}_3} = (0.059 \pm 0.08) \text{ \%/cm}$. The manufacturers typically upper bound for the absorption coefficient is 0.1%/cm at a wavelength of 1064 nm. Our result is therefore in accordance with this upper bound. A second reference is a cavity loss measurements performed in [4.10]. The result of this loss measurement was 0.07%/cm, still containing losses due to the residual reflection of the AR coating of the crystal. Our result is also in good agreement with this loss measurement.

The mean value of the results for the input mirror M_1 is $R_1 = (89.43 \pm 0.75) \%$, which is in good agreement with the manufacturers specification of $(90 \pm 1) \%$.

The result for the effective reflection \tilde{R}_2 of $(99.79 \pm 0.01) \%$ containing all round trip losses amongst them the absorption $\alpha \cdot L = 0.059 \text{ \%/cm} \cdot 2 \cdot 0.65 \text{ cm} = 0.077 \%$ is also in agreement with the specified value of $R_2 > 99.8 \%$.

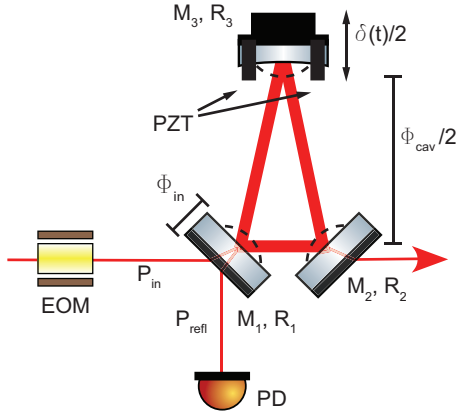


Figure 4.7: Experimental setup: Three mirrors with $R_1 \approx R_2 < R_3 \approx 1$ build a ring-cavity. The cavity round-trip phase change $\delta(t)$ is caused by a PZT between the cavity spacer and mirror M_3 . A temperature change $T(t)$ in the input mirror due to absorption in the coating leads to a time-dependent phase for the in-coupled field $\phi_{\text{in}}(t)$ with respect to the intra-cavity field. The expansion of all three mirrors due to $T(t)$ shortens the cavity round-trip length.

4.2 Measuring the Absorption of High Reflective Coatings

The work presented in this Section is published in [4.2].

In this section an experiment is described that exploits the photo-thermal self-phase modulation to measure the absorption of a dielectric coating. The absorption of a cavity input mirror with a measured power reflectivity of 99.96% at a wavelength of 1064 nm was measured. The dielectric coating was a high-quality ion-beam sputtered (IBS) $\text{SiO}_2/\text{Ta}_2\text{O}_5$ multi-layer stack on a super-polished one-inch fused-silica substrate. The optical arrangement of the (high finesse) ring cavity is shown in Fig. 4.7. The cavity round trip length is about 42 cm, which can be changed by a PZT by a few microns. Similar cavities are frequently used as spatial mode cleaners and frequency low-pass filters in laser-interferometric high-precision experiments [4.11, 4.12]. Here, we used a mode cleaner with a measured finesse of 6700 and an intra-cavity power of about $1700 \cdot P_{\text{in}}$. Using `tksim`, the measured resonance peaks of the cavity were simulated. By applying a Nelder-Mead algorithm, the best fitting values for R_1 , R_2 and α were found.

4.2.1 Experimental Procedure and Setup

A series of absorption measurements was performed on two identical mirrors from the same coating run. The coating was a $\text{SiO}_2\text{-Ta}_2\text{O}_5$ multilayer stack, applied to plane Corning 7980 substrates. The mirrors were manufactured by **Advanced Thin Films** [4.14] and designed for a reflectivity of $(99.95 \pm 0.01)\%$ at a wavelength of 1064 nm and an angle of incidence (AOI) around 44° in s-polarization. Two of these mirrors, the input mirror M_1 and the end-mirror M_2 , and an additional curved mirror M_3 with a 1 m radius of curvature (ROC) and with much higher reflectivity $R_3 \approx 1$ were clamped to an aluminum spacer to form a ring cavity as shown in Fig. 4.7. The cavity was carefully assembled in a clean-room environment to prevent contamination of the mirrors. Since the transmission of M_3 was negligible compared to the transmission of M_1 and M_2 the resonator was impedance matched apart from losses within the cavity. This means that

4 Demonstration of the Measurement Principle

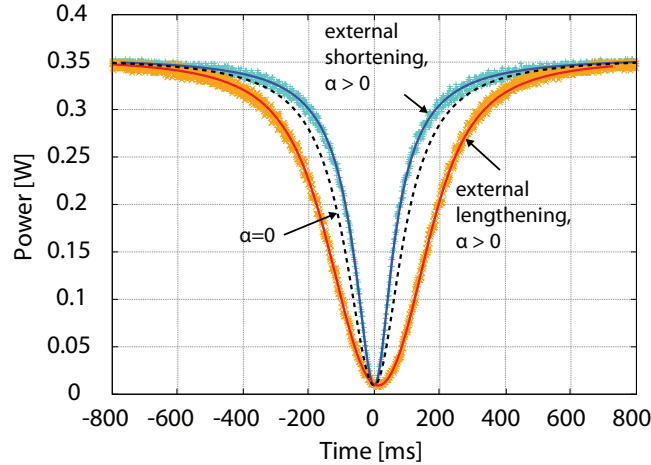


Figure 4.8: Example of measured resonance peaks at an input power of 355 mW and a scan-frequency of 40 Hz. On resonance, a power of less than 10 mW was reflected due to non-perfect impedance matching and non-perfect mode-matching. The light blue dots (measurement) and the dark blue line (simulation) show the resonance peak for an external shortening of the cavity, the yellow dots (measurements) and the red line show the resonance peak for an external lengthening of the cavity. The dashed line represents the resonance peaks without thermal effect (no absorption).

for a perfect mode-matching nearly 100% of the incoming power was transmitted into the resonant cavity and no light was reflected. A fast PD recorded the resonance peaks in reflection of the lengthened or shortened cavity. For both mirror samples, a series of measurements was made, varying the cavity scan velocity and, thus, the heating effect. To actuate the cavity length, a PZT between M_3 and the spacer was used that moved M_3 with a velocity v applying a ramp-signal from a function generator.

In this setup the absorption of the input mirror M_1 can be measured, as the beam receives a phase shift due to the change of the optical path length through this mirror, while M_2 and M_3 only cause a phase shift within the cavity due to their thermal expansion (see Subsec. 3.2.2). For the used mirror substrates the second effect is approximately one order of magnitude smaller than the first one, which in general depends on the material properties of the substrates.

Figure 4.8 shows an example of measured resonance peaks at an input power of 355 mW. At resonance less than 10 mW are reflected. A slow scan frequency of 40 Hz induces a visible hysteresis due to a thermal effect. For an external shortening of the cavity the light blue dots (measured) and dark blue line (simulation) form. For an external lengthening the yellow dots (measurement) and the red line (simulation) form. The black line shows a simulated peak for both scan directions without thermal effect.

4.2.2 Measurement and Data Analysis

For the simulation the PZT-actuated cavity length change per time interval needs to be known precisely. Usually PZTs show a non-linearity and even a hysteresis, which are both scan-velocity dependent. The calibration procedure described in Section 4.1.2 is very complex and time-consuming and therefore limits the possible number of single measurements. Therefore in this experiment the PZT was calibrated via optical frequency markers on the laser light which are sidebands of a phase modulation imprinted by an electro-optical modulator (EOM). It was ensured that the sidebands were as close to the carrier as possible to minimize the required scanning range. Thus, the PZTs motion could be well described by a linear model. At the same time, the sidebands have to be outside the cavity's line width to be visible. Additionally, for measurements where heating leads to high temperatures it should be assured that the substrate can cool down before the sideband becomes resonant. Otherwise the sidebands resonance position is shifted in the time-domain and the calibration becomes inaccurate. For this calibration the cavity length was scanned approximately from sideband to sideband and the mirror-velocity was extracted separately for lengthening and shortening of the cavity. In this experiment a sideband frequency of 2.525 MHz was used and it was scanned over about 1% of an FSR. In this range, the PZTs non-linearity was very small. The calibration procedure via sidebands turned out to be a strong improvement compared to the calibration procedure in the LiNbO₃ experiment since it is much easier and faster to operate (provided that the equipment is available) and more accurate. Since increasing the input power and decreasing the scan velocity both result in further increasing the thermally induced hysteresis of the resonance peaks, only the scan velocity was varied in this experiment which was easier to realize for the used setup.

In Tab. 4.3, the detailed geometric parameters of the cavity and the laser beam are summarized, that enter `tksim`. The internal structure of the coating is neglected in the simulation. The coating is considered as part of the mirror substrate with the substrate's material properties. For the material parameters values from literature were used, ideally given by the manufacturers.

Like in the LiNbO₃-experiment, R_1 and \tilde{R}_2 , as well as the absorption α , were treated as free parameters of the simulation instead of using the reflections as given by the coating manufacturer, because of their strong influence on the heating of the mirror substrate.

For every single measurement a Nelder-Mead algorithm varied the quantities R_1 , \tilde{R}_2 and α , and thus minimized the deviation between simulated and measured data [4.13]. The algorithm starts by creating a so-called simplex with four points in the three-dimensional parameter space and calculates the deviation at each of these points. The simplex is then folded and contracted according to certain rules [4.13], finally converging to the point of minimum deviation. The result from the Nelder-Mead algorithm is a single set of best fitting values for R_1 , \tilde{R}_2 and α . No error bar is given as from the MCMC algorithm. In order to derive error bars for the measured absorption, a large

4 Demonstration of the Measurement Principle

Table 4.3: Material and geometric parameters of the Corning 7980 mirror substrates and the cavity, respectively, as used for the simulations. Wavelength and temperature dependent parameters are given at 1064 nm and room temperature.

Material parameters (at 1064 nm and room temperature)		Reference
index of refraction n	1.48082	[4.15]
thermal refr. coeff. dn/dT	$8.45 \cdot 10^{-6} / \text{K}$	[4.15]
specific heat c	770 J/(kg K)	[4.16]
density ρ	2201 kg/m ³	[4.17]
thermal expansion a_{th}	$0.52 \cdot 10^{-6} / \text{K}$	[4.17]
thermal conductivity k_{th}	1.3 W/(m K)	[4.17]
material emissivity ϵ	1.0	
Cavity geometry parameters		
input power P	350 mW	
round-trip length L	42 cm	
beam waist w_0	371 μm	
mirror length D	6.35 mm	
mirror radius r	12 mm	
mode matching (MM)	99.9 %	
angle of incidence (AOI)	42.13°	

number of measurements was performed on two (identical) mirror samples from the same fabrication batch (samples A and B). For both samples measurements at different scan-velocities were performed. The final results were the mean value of the fits of all single measurements. The error bar was the standard deviation of the individual fitting results.

4.2.3 Experimental Results and Error Propagation

Nine individual measurements were analyzed for sample A, and 22 for sample B. The mean values of all 31 measurements on this particular coating were the following. The reflectivity (of in-coupling mirror M_1) was found to be $R_1 = (99.9607 \pm 0.0009 \%)$. \tilde{R}_2 was determined to be $(99.9446 \pm 0.0017 \%)$. All measurements were performed at an input power of 360 mW for sample A and 355 mW for sample B. The scan frequencies varied from 20 Hz to 1.1 kHz. 200 Hz was the threshold, underneath which a thermal effect was visible. For sample A, six measurements showed a significant thermal effect and were used to derive the absorption of the coating, for sample B, 16 measurements were used. The final absorption was thus deduced from 22 measurements resulting in $\alpha = (23.9 \pm 2.0)$ ppm per coating. Figure 4.9 gives a graphical overview over the

4.2 Measuring the Absorption of High Reflective Coatings

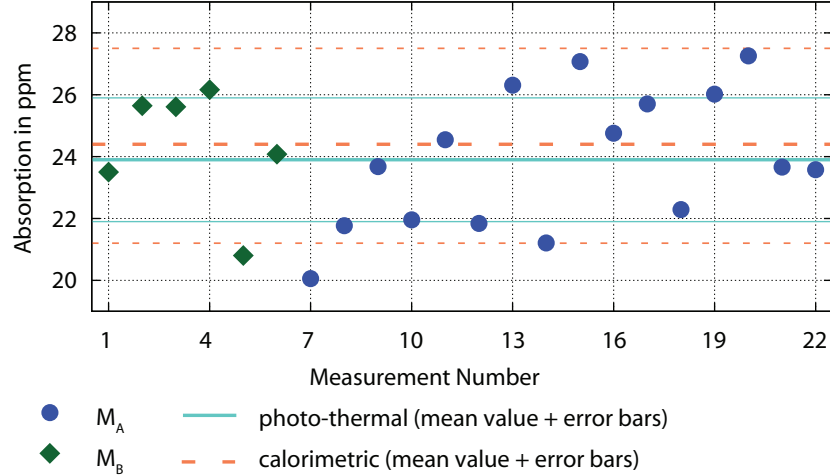


Figure 4.9: Individual measurement results for the absorption of sample A (green diamond) and sample B (blue circle). For both mirror samples several measurements with different scan velocities were performed. The mean value and the standard deviation are given by the light green, solid lines. The red, dashed lines represent the mean value and standard deviation of the independently performed calorimetric measurements.

individual results for α_A (green diamonds) and α_B (blue circles) for all 22 measurements showing a thermal effect. The results for the individual mirrors can be found in Tab. 4.4.

Not only the error due to the measurement statistics has to be considered, but also possible (systematic) errors in the input parameters. The procedure was identical to the one explained in Section 4.1.4. The investigation showed that in this experiment the parameters can also be grouped into two categories. The first category contains parameters that have a very weak influence on the absorption deduced in our setup: Heat radiation described by the material emissivity ($0.0 < \epsilon \leq 1.0$) is almost not relevant because the temperature increase is very small and the heat transport into the substrate is much larger than heat radiation. A change of ϵ from 1.0 to 0.0 results in a change of α smaller than 0.6%. The absorption coefficient of the mirror substrate ($\alpha_{\text{substrate}}$)

Table 4.4: Results for the reflections R_1 and \tilde{R}_2 and the absorption α for each mirror sample, A and B, and from all measurements, \overline{AB} . For an easier legibility we give the results for the reflection in 1-R in this table.

	$1-R_1$ in ppm	$1-\tilde{R}_2$ in ppm	α in ppm
<i>A</i>	391 ± 8	530 ± 18	24.3 ± 2.0
<i>B</i>	394 ± 9	549 ± 14	23.8 ± 2.1
\overline{AB}	393 ± 9	544 ± 17	23.9 ± 2.0

4 Demonstration of the Measurement Principle

can be neglected, as it is already quite small. Also, the power transmitted through the mirror substrate is only single-path and therefore smaller by more than three orders of magnitude than the intra-cavity power, since the power inside the cavity is enhanced by a factor of 1700 on cavity resonance. The index of refraction n of fused silica is known very accurately, but even an error of as large as a few percent would have a negligible effect on the coating absorption α . The same applies to the beam waist w_0 and the AOI, which change the power density on the mirror surface. Both parameters are defined precisely by the cavity geometry. The substrate radius r for $r \gg w_0$ has no effect on the coating absorption α . The second category contains the remaining parameters, whose relative errors result in systematic errors of our absorption having the same order of magnitude. These are the input laser power P , the mode matching factor MM , the mirror substrate length D , the thermal conductivity k_{th} , the thermal refractive coefficient dn/dT , the thermal expansion a_{th} , the density ρ and the heat capacity c . We calculated the influence on α for a 4% change in the particular material parameter for an example measurement. All new results were within the error bars of the original result. Note, that there are no input parameters which influence our result stronger than linearly.

Assuming that the measured parameters as well as the material parameters from literature are precise to within 4% each and statistically independent from each other, it can be concluded that the standard deviation of the measurement statistic of ± 2.0 ppm ($\pm 8.2\%$) dominates our final result.

From the simulations it was found that the phase shift of the incoming beam due to heating of the input mirror is dominating the resonance peak deformation by about one order of magnitude. The mirror expansion which shortens the cavity round-trip length is comparatively small. For Corning 7980 dn/dT is nearly 20 times larger than a_{th} , which is actually the case for a large amount of glasses and crystals, in particular for fused silica.

4.2.4 Final Results and Discussion

The absorption measurements on a high quality $\text{SiO}_2\text{-Ta}_2\text{O}_5$ coating with a reflectivity of 99.96% result in $\alpha = (23.9 \pm 2.0)$ ppm for s-polarized laser light of 1064 nm under an angle of incidence (AOI) of about 42° . Both mirror samples were independently analyzed in a laser calorimetry setup at the Laser Zentrum Hannover (LZH) using the international standard on testing the absorptance of optical laser components, ISO 11551 [4.18]. The result for the same wavelength, polarisation and AOI was $\alpha = (24.4 \pm 3.2)$ ppm. Both results are in excellent agreement.

The calorimetry setup was also used for a third mirror sample (C), again from the same coating run and substrate. Sample C was cleaned with *First Contact* [4.19] before the measurement. Here the result was $\alpha = (25.0 \pm 3.3)$ ppm, being in good agreement to the absorption of samples A and B. In particular this result indicates that neither the rather high absorption measured here is related to surface contaminations, nor the surface absorption increases due to the treatment with First Contact.

Commonly known values for the absorption of high quality IBS coatings are a few ppm per coating. For the coating investigated here similarly low absorptions were expected, although the coating was not explicitly ordered for low absorption losses. The reason for the unexpected high optical absorption is currently unclear. Therefore some information about the history of the mirror samples will be given here. The mirror samples were fabricated a few years ago and were not used in any other experiment before being characterized in the course of this work. The original packaging of substrates was opened in a class 1000 (ISO6) clean-room environment, examined with a cold-light source and, if necessary, cleaned with compressed air or in case of sample C with First Contact. Still inside the clean room the samples A and B were clamped air-tight onto the aluminum spacer. The experiment itself took place in a laboratory outside the clean room. For the measurements at the LZH the samples were removed from the spacer in the clean room and transported in their original packaging. The measurements at the LZH were performed under standard laboratory conditions. In summary, although we tried to minimize any surface contamination and checked the surfaces for dust particles, the possibility cannot be excluded that the high measured absorptions are due to surface contamination.

4.3 Conclusion

In the two experiments presented in this Chapter, the photo-thermal self-phase modulation technique was applied to measure the optical absorption of a bulk-substrate and of a high reflective coating.

The obtained result for the optical absorption of a 7 mol% MgO-doped LiNbO₃ bulk substrate of $\alpha_{\text{LiNbO}_3} = (0.059 \pm 0.08) \%$ /cm agreed with manufacturers data and data from a cavity loss measurement. Additionally, the results for the mirror reflectivities of this setup were in good accordance with manufacturer's data.

In the second experiment the photo-thermal self-phase modulation was exploited in a high-finesse optical cavity to measure the optical absorption inside the coating of the cavity in-coupling mirror. Excellent agreement with results from a calorimetric measurement method was found. The simulation showed that the dominating photo-thermal self-phase modulation in this setup originates from the temperature dependence of the mirror substrate's refractive index dn/dT .

While in the first experiment a MCMC algorithm was used to find the best set of fitting parameters, for the second experiment a Nelder-Mead algorithm was applied. An advantage of the MCMC algorithm are the results including error bars for every single measurements, while for the Nelder-Mead algorithm a larger amount of single measurements are necessary to obtain a standard deviation for error bars. However, the Nelder-Mead algorithm significantly reduced the time needed to obtain a set of best fitting parameters for a single measurements. Therefore, the latter was used for the fitting process for the experiments presented in the following chapters.

4 Demonstration of the Measurement Principle

It can be concluded that the photo-thermal self-phase modulation technique is highly suited as an absorption measurement method to obtain the optical absorption coefficient of a bulk substrate or the in-coupling coating of a (high finesse) cavity.

- 4.1 N. Lastzka, J. Steinlechner, S. Steinlechner, R. Schnabel
Measuring small absorptions by exploiting photo-thermal self-phase modulation
Applied Optics **49** 28, pp. 5391–5398, 2010
- 4.2 J. Steinlechner, L. Jensen, C. Krüger, N. Lastzka, S. Steinlechner, R. Schnabel
Photothermal self-phase-modulation technique for absorption measurements on
high-reflective coatings
Applied Optics **51**, pp. 1156–1161, 2012
- 4.3 N. Lastzka
Numerical modelling of classical and quantum effects in non-linear optical systems
PHD Thesis, Hannover, Germany, 2010
- 4.4 D. E. Zelmon, D. L. Small, D. Jundt
Infrared corrected Sellmeier coefficients for congruently grown lithium niobate and
5 mol.% magnesium oxide-doped lithium niobate
J. Opt. Soc. Am. B **14** 12, pp. 3319–3322, 1997
- 4.5 D. H. Jundt, M. M. Fejer, R. L. Byer
Optical Properties of Lithium-Rich Lithium Niobate Fabricated by Vapor Trans-
port Equilibration
Journal of Quantum Electronics **26** 1, pp. 135–138, 1990
- 4.6 M. J. Weber
Handbook of optical materials
CRC Press LLC, Boca Raton (FL), USA, 2003
- 4.7 I. W. Kim, B. C. Park, B. M. Jin, A. S. Bhalla, J. W. Kim
Characteristics of MgO-doped LiNbO₃ crystals
Material Letters **24**, pp. 157–160, 1995

Bibliography

- 4.8 K. K. Wong (Editor)
Properties of Lithium Niobate
INSPEC, London, United Kingdom, 2002
- 4.9 P. Gregory
Bayesian logical data analysis for the physical sciences
Cambridge University Press, Cambridge, United Kingdom, 2005
- 4.10 H. Vahlbruch
Squeezed Light for Gravitational Wave Astronomy
PhD Thesis, University of Hannover, 2008
- 4.11 N. Uehara
Ring Mode Cleaner for the Initial LIGO 10 Watt Laser
Internal LIGO Report, Stanford University, Stanford, California, 1997
- 4.12 B. Hage, A. Samblowski, and R. Schnabel
Towards Einstein-Podolsky-Rosen quantum channel multiplexing
Phys. Rev. A **81** 062301, 2010
- 4.13 J. A. Nelder, R. Mead
A simplex method for function minimization
The Computer Journal **7** pp. 308–313, 1965
- 4.14 ATFilms, USA
<http://www.atfilms.com>.
- 4.15 D. B. Leviton, B. J. Frey
Temperature-dependent absolute refractive index measurements of synthetic fused silica
Proc. SPIE **6273**, 62732K, 2006
- 4.16 Valley Design Corporation, Santa Cruz, USA
<http://www.valleydesign.com>
- 4.17 Corning Inc., USA
<http://www.corning.com>
- 4.18 U. Willamowski, T. Groß, D. Ristau, H. Welling
Calorimetric measurement of optical absorption at 532 nm and 1064 nm according to ISO/FDIS 11551
Proc. SPIE **2870**, pp. 483–494, 1996
- 4.19 Photonic Cleaning Technologies, Platteville, USA
<http://www.photoniccleaning.com>

Absorption Measurements on Crystalline Silicon

The work presented in this Section is accepted for publication in Classical and Quantum Gravity.

Crystalline silicon is currently being discussed as test-mass material for future generations of gravitational wave detectors that will operate at cryogenic temperatures. We present optical absorption measurements on a large-dimension sample of crystalline silicon at a wavelength of 1550 nm at room temperature. The absorption was measured in a high intensity monolithic cavity setup using the photo-thermal self-phase modulation technique. The result for the absorption coefficient of this sample with a specific resistivity of 11 k Ω cm was measured to be $\alpha_A = (264 \pm 39)$ ppm/cm.

5.1 Introduction

The initial (1st) and advanced (2nd) generations of interferometric gravitational wave (GW) detectors employ suspended fused silica test masses and use a laser wavelength of 1064 nm [5.1–5.3]. Observatories beyond the 2nd generation will require very high laser powers to reduce the quantum noise at frequencies above ~ 50 Hz, while at lower frequencies it is promising to cool the test masses to cryogenic temperatures to reduce thermal noise.

While at room temperature fused silica shows a high mechanical Q-factor [5.4] and low optical absorption [5.5], the mechanical Q-factor decreases by several orders of magnitude at cryogenic temperatures [5.6, 5.7]. This makes fused silica unsuitable as test mass material for cryogenically operated GW observatories. Crystalline silicon, however, shows a promising mechanical Q-factor at room temperature that even increases

towards cryogenic temperatures up to 2×10^9 [5.8,5.9]. Due to the very high absorption coefficient of about $10/\text{cm}$ at 1064nm , silicon test-masses require a change to higher laser wavelengths, where the absorption coefficient decreases rapidly [5.10].

A wavelength of 1550nm is located within the silicon energy gap and appears promising because of the availability of appropriate optical components and lasers developed for the telecommunication sector. Also, strong squeezed-light sources of $> 12\text{dB}$ are available at 1550nm [5.11] to increase the sensitivity of GW detectors beyond the quantum limit [5.12]. An up to now open question are measurements of the optical absorption coefficient at 1550nm in the temperature range from a few kelvin up to 300K . Unfortunately, the measurements presented in [5.10] were done at slightly shorter wavelength up to 1450nm . Furthermore, these measurements are a prediction of the absorption coefficient that is based on photo-current measurements. They might not include various effects that lead to optical absorption but do not generate charge carriers. Also the photo-current measurement might not show all absorption effects that are relevant for thermal noise.

In this paper we present direct optical absorption measurements on two silicon samples in large dimensions at room temperature using the photo-thermal self-phase modulation technique [5.13]. Silicon sample A forms a monolithic cavity. The measurement technique is perfectly adapted to this setup and therefore gives very precise results. While the photo-thermal effect delivers the absorption coefficient, with this method the round-trip loss is measured independently at the same time. Since losses apart from absorption are small for this monolithic setup, the two results confirm each other. Silicon sample B from another manufacturer is uncoated and was placed at Brewster's angle in a Fabry-Perot cavity. Being less stable and containing reflection and scattering losses, the measurement with this setup only served as an order of magnitude estimation to yield an approximate upper and lower limits of the absorption. This measurement ensured sample A to be not coincidentally untypically high or low absorbing or that a large amount of the absorption was not caused by the coating process or by the dielectric coatings.

5.2 Absorption Measurements on Silicon Sample A

Sample A was manufactured by *Siltronic AG* [5.14] with the Czochralski technique. The crystal's orientation is (111). The material has a specific resistivity of about $11\text{k}\Omega\text{cm}$, which indicates a low doping or contamination with foreign atoms. According to the manufacturer it is a low boron doping, which is a p-donator. This means the impurity concentration is approximately 2×10^{12} atoms per cm^3 [5.15]. Sample A is the purest material available to us in the required dimensions at ordering time.

The substrate was cut and polished into a cylinder with the rotation axis being parallel to the (111) axis. The cylinder's diameter was $2 \times R = 10\text{cm}$ (R is the substrate radius), the length was $L = 6.5\text{cm}$. The end surfaces were polished to be convex curved with a radius of curvature of 1m to form a cavity with a free spectral range (FSR) of 663MHz .

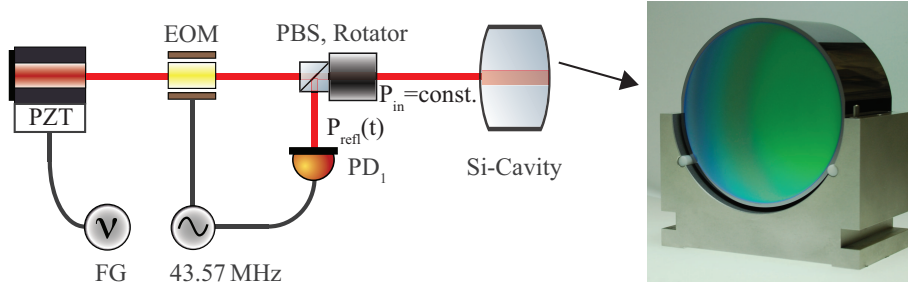


Figure 5.1: Schematic of the experimental layout. The cylindrical silicon substrate with convex curved and coated end surfaces formed a monolithic cavity. A function generator (FG) that actuated the piezo electric transducer (PZT) of the laser modulated the laser wavelength. Photo detector PD_1 detected the power reflected by the cavity and showed the cavity resonance peaks. On the right side, a photograph of the monolithic cavity with 6.5 cm length and 10 cm diameter is shown.

The substrate's curved end surfaces were coated using ion beam sputtering (IBS). The high-reflection coatings consisted of SiO_2 and Ta_2O_5 and had a design reflectivity of $> 99.9\%$ at a wavelength of 1550 nm. Hence, the coated substrate formed a monolithic cavity with beam propagation along the (111) axis.

5.2.1 Experimental Setup

Fig. 5.1 shows a schematic of the experimental setup. A laser beam at a wavelength of 1550 nm was mode-matched to the eigenmode of the monolithic cavity. To calibrate the time-axis of our measurements we used frequency markers. An electro optical modulator (EOM) generated these frequency markers by imprinting sidebands at a frequency of 43.57 MHz onto the light field.

Photo detector PD_1 detected the reflected light, which was separated from the incident field by a combination of a Faraday rotator and a polarizing beam splitter (PBS). Demodulating PD_1 and creating a Pound-Drever-Hall-type [5.16] error-signal generated the frequency markers.

For exploiting the photo-thermal self-phase modulation technique, the laser frequency was scanned around the resonance frequency of the cavity via a piezo electric transducer (PZT). An increasing wavelength corresponded to a shortening of the cavity and a decreasing wavelength to a lengthening of the cavity.

The input laser power was 22 mW for all measurements resulting in an intensity of 700 W/cm^2 within the substrate. We performed several measurements by varying the scan frequency starting from 0.2 Hz to 49 Hz in 18 steps with a constant scan amplitude. The frequency for each measurement number can be found in Tab. 5.1. Because the PZT showed a hysteresis, the actual wavelength change had to be calibrated for each frequency for increasing and decreasing wavelength. The time axis of each measurement was calibrated from the scan frequency, the FSR, and the detected error signal. In

Table 5.1: Scan-frequencies used for the single measurements on sample A.

Measurement number	1	2	3	4	5	6	7	8	9
Scan frequency [Hz]	0.2	0.4	0.6	0.8	1.0	1.2	1.4	1.6	1.8
Measurement number	10	11	12	13	14	15	16	17	18
Scan frequency [Hz]	2	4	6	8	10	20	30	40	49

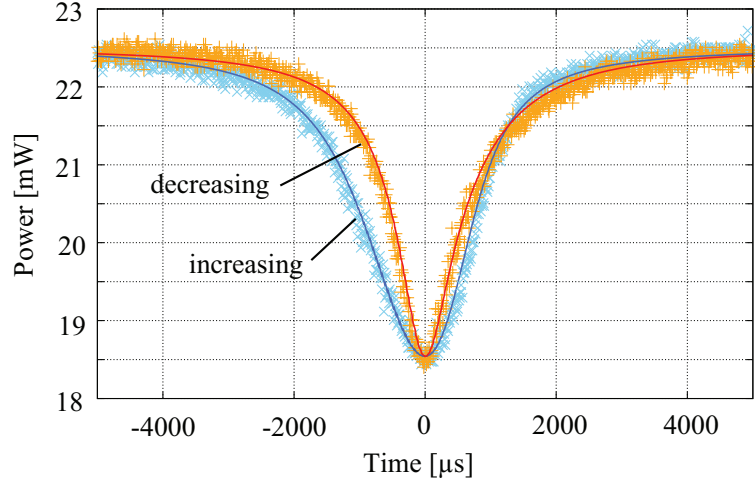


Figure 5.2: Example of measured (crosses) and simulated (solid lines) reflection peaks at a scan frequency of 0.6 Hz: The broad (blue) peak forms for an increasing wavelength, the narrow (orange) one for a decreasing wavelength. Without absorption, both peaks would be identical.

Figure 5.2, an example measurement for a scan frequency of 0.6 Hz is shown. This frequency corresponds to a scan velocity of about 2 ms/peak at full width half maximum (FWHM). The yellow crosses (narrow peak) show the measured peak for a decreasing wavelength with the corresponding simulation in red (solid line). The light blue crosses (broad peak) show the peak for an increasing wavelength with the simulation in dark blue (solid line). Without absorption, the two peaks were identical.

5.2.2 Measurement Analysis and Results

To calculate the absorption coefficient α from the measured peaks as shown in Fig. 5.2, the peaks were fitted. For the fitting process we used the parameters from Table 5.2 as well as the in-coupling reflectivity R_1 , the effective out-coupling reflectivity \widetilde{R}_2 , and for measurements with a visible thermal effect α as fitting parameters. Here, \widetilde{R}_2 is the effective reflection of the out-coupling coating accounting for the entire cavity round trip loss apart from the transmission of the in-coupling coating. The values for material parameters were taken from literature [5.17–5.19]. For the geometric parameters, we

5.2 Absorption Measurements on Silicon Sample A

Table 5.2: Material and geometric parameters of the monolithic silicon cavity used for the simulations.

Geometric parameters		Source
crystal radius R	5 cm	specified by manufacturer
crystal length L	6.5 cm	specified by manufacturer
beam waist ω_0	217.8 μm	calculated from L , n and ROC
Material parameters		
index of refraction n	3.48	[5.17]
thermal expansion a_{th}	$2.62 \times 10^{-6}/\text{K}$	[5.18]
thermal refr. coeff. dn/dT	$1.87 \times 10^{-4}/\text{K}$	[5.19]
specific heat c	714 J/(kg K)	[5.18]
density ρ	2330 kg/m ³	[5.18]
thermal conductivity k_{th}	140 W/(m K)	[5.18]

used values based on our best knowledge of the cavity design. A Nelder-Mead algorithm was run to find the best set of fitting parameters minimizing the standard deviation of measurement and simulation. 13 of 18 single measurements showed a visible thermal effect and were used to derive the absorption. The remaining five measurements showed no thermal effect due to the high scan-frequency. 8 Hz was the threshold above which no thermal effect occurred. All 18 measurements were used to derive R_1 and \widetilde{R}_2 . The results obtained from measurements without thermal effect were consistent with the remaining results.

Figure 5.3 a. shows the results for the absorption coefficient α derived from the 13 different measurements (dark-green dots). The purple lines show the mean value of all single results and their standard deviation which is $\alpha = (264 \pm 39)$ ppm/cm ($39 \text{ ppm} \hat{=} 15\%$).

The results for the (power) reflection R_1 of the in-coupling coating are shown in Figure 5.3(b). The mean value and standard deviation of all 18 single measurements is $R_1 = (99.9784 \pm 0.0015)\%$. Measurement numbers 14–18 did, as stated above, not exhibit a visible thermal effect.

Figure 5.3(c) shows the results for \widetilde{R}_2 for all single measurements (dark-green dots) and their mean value and standard deviation (turquoise lines) of $\widetilde{R}_2 = (99.630 \pm 0.025)\%$. This result was used to cross-check the obtained absorption values. An absorption coefficient of $\alpha = (264 \pm 39)$ ppm/cm results in an absorption of $\alpha_{\text{total}} = 264 \text{ ppm/cm} \times 13 \text{ cm} = 0.343\%$ per round-trip. The round-trip loss added to \widetilde{R}_2 results in a new effective reflection $\widetilde{R}_2' = \widetilde{R}_2 + \alpha_{\text{total}} = 99.973\%$ that still contains the cavity scattering loss. Since the pure reflection can be assumed to be very similar to R_1 (identical coating design, but different coating runs) the results for the three parameters agree perfectly. This is an additional consistency check and not an automatical consequence of the simulation.

We repeated the series of measurements for a polarization rotated by 90° . Further we

5 Absorption Measurements on Crystalline Silicon

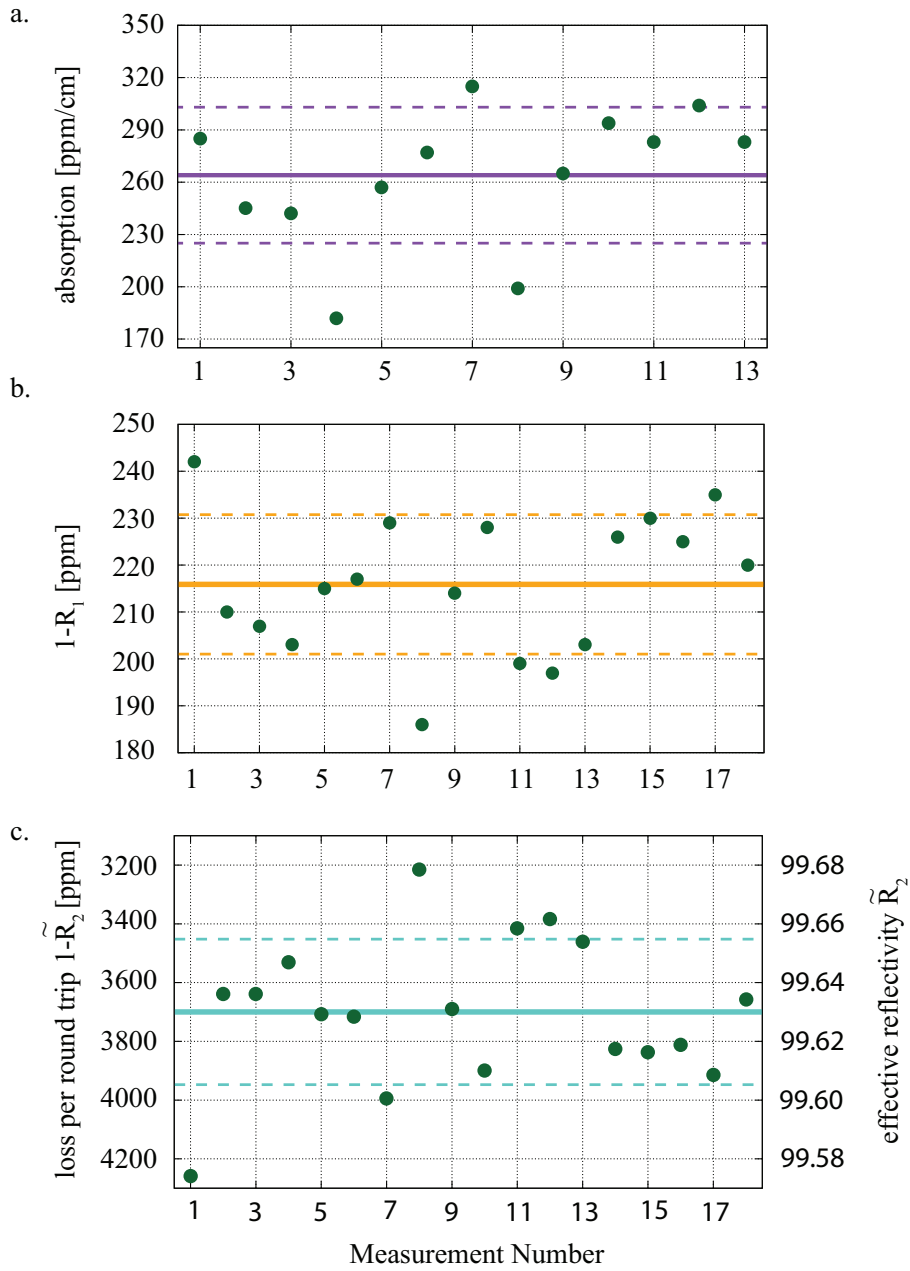


Figure 5.3: a. Results for the absorption from single measurements (green dots). The mean value and the standard deviation of $\alpha = (264 \pm 39)$ ppm/cm are given by the purple line and the dashed purple lines, respectively. The dots in b. and c. show the results for the in-coupling reflectivity R_1 and the effective out-coupling reflectivity \tilde{R}_2 with $R_1 = (99.9784 \pm 0.0015)\%$ in orange and $\tilde{R}_2 = (99.630 \pm 0.025)\%$ in turquoise.

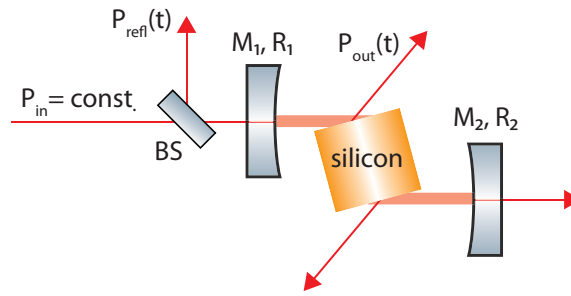


Figure 5.4: Experimental setup for the measurement on the second silicon sample. The beam was coupled into the cavity through mirror M_1 . The silicon substrate was placed in the cavity at Brewster's angle of 74° which caused a strong beam displacement. M_2 was the end mirror of the cavity. The resonance peaks were detected in reflection of the beam splitter (BS). The laser wavelength was scanned with a function generator.

exchanged in-coupling and out-coupling coating and repeated the measurements for the two polarizations. As expected, in each case the results for the absorption coefficient agreed with the result presented above within the error bars.

5.2.3 Error Propagation

The error bar of 39 ppm or 15% corresponds to the standard deviation of 13 independent measurements using different scan-velocities. An additional error bar arises from uncertainties in the simulation input parameters. To estimate this error, we individually changed the input parameters listed in Table 5.2 by $\pm 10\%$ and recalculated R_1 , \widetilde{R}_2 and α . We found that for most parameters the influence on α is approximately linear and none of the changed parameters caused a change of the result for α by more than 15%.

For n , the error bar of the value from literature is in the order of 10^{-5} [5.17] and therefore negligible, the uncertainty of dn/dT is in the same order of magnitude [5.19]. a_{th} and dn/dT affect the result as a sum. Since $a_{th} \ll dn/dT$, an uncertainty of a_{th} is negligible. The error bars of c , ρ and k_{th} are not known to us. We estimate that the uncertainties of the cavity geometric input parameters as well as for the calibration of the time axis and in the measurement of the mode-matching are below 10%.

If the simulation input parameters are precise within 10%, our statistical error bar of 15% is the dominating error contribution.

5.3 Measurements on Silicon Sample B

The absorption measured with sample A was unexpectedly high (see discussion). To verify that this sample did not absorb untypically much, or that the coating process or the coating itself did not cause the absorption, a second experiment with a different sample B was performed. The two samples differed in manufacturer and crystal orientation.

5 Absorption Measurements on Crystalline Silicon

A cylindrical substrate with one inch diameter and 3.5 cm length was manufactured by Mateck [5.20] in (100) orientation using the Czochralski procedure. The (100) axis is the rotation axis of the cylinder. The cylinder end surfaces were polished to be parallel with a tolerance of $< 30''$. The material was declared by the manufacturer to be undoped with a resistivity of $> 5 \text{ k}\Omega\text{cm}$.

The substrate was placed in a resonator at Brewster's angle of 74° to minimize round trip loss due to reflection at the substrate surface (see Figure 5.4). The mirrors were clamped to an aluminium spacer. The laser beam coupled into the cavity through the in-coupling mirror M_1 . The reflected beam power P_{refl} was detected in reflection of the beam splitter (BS). (Using the BS instead of the Faraday rotator and PBS combination in the first setup, does not change anything for the experiment.) The modulation of the laser, the calibration of the time axis and the measurement procedure were identical to the procedures described in Section 5.2.1 for the monolithic cavity setup.

Entering the substrate at Brewster's angle causes an elliptical beam profile within the substrate. Since not necessary for other experiments, a non-circular beam profile is not implemented in our simulation program. The discussed measurement had the goal of independently determining a lower limit for the optical absorption to confront the obtained value with the results from sample A. Therefore, a calculation of an upper limit for the power density and thus for the heat distribution within the substrate is sufficient. This is given by a circular beam profile with the radius of the minor semi-axis of the elliptical profile. Since a higher power density requires a smaller absorption to cause the same thermal effect, this assumption yields a lower limit for the absorption coefficient.

From 52 single measurements, the lower limit for the absorption was found to be $\alpha_B = (149 \pm 79) \text{ ppm/cm}$. The results of the single measurements are shown in Figure 5.5 (green dots). The mean value of all measurements with the standard deviation are depicted by the light-blue line and the light-blue dashed lines, respectively. Despite a shared spacer for mirrors and substrate, the external cavity setup proved to be instable and prone to acoustical disturbances, which caused large error bars due to the statistical fluctuations of the detected peaks.

The error propagation was already discussed for sample A. The uncertainty of the result is dominated by the large standard deviation, while the errors in the material parameters are negligible in first order approximation.

Apart from the elliptical beam profile, the large statistical error shows that the second setup is much more instable and therefore disadvantageous compared to the monolithic setup. Nevertheless, the lower limit for the absorption of $\alpha_B = (149 \pm 79) \text{ ppm/cm}$ allows the conclusion that the absorption in sample A did not primarily originate in the dielectric coatings.

In a second series of measurements, the round trip loss of the cavity was measured. This provided an the upper limit for the absorption coefficient. For this measurement, two mirrors with identical coatings were used and the round-trip loss was minimized by

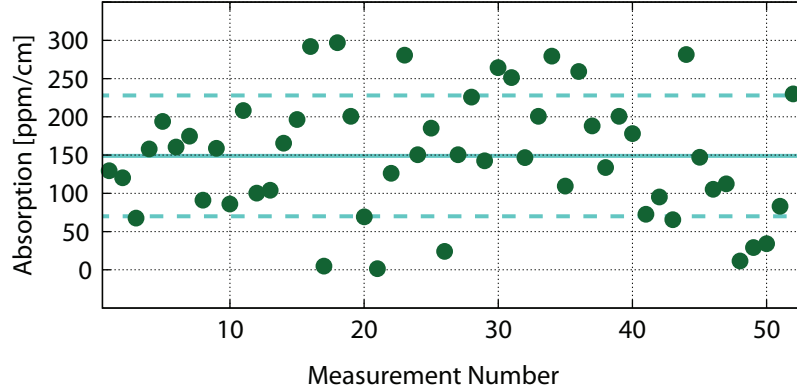


Figure 5.5: The results for the lower limit of the absorption coefficient of sample B obtained using photo-thermal self-phase modulation are shown by the green dots. The light blue line illustrates the mean value of all single measurements of $\alpha_B = 149$ ppm/cm and the dashed light-blue line the error bars of 79 ppm/cm.

inclining and rotating the substrate. The maximum impedance matching was found to be $(21.2 \pm 0.3)\%$. (An impedance matching of 100% means that the reflected power at resonance is zero.) Using the design reflectivity of $R_1=R_2 = (99.97 \pm 0.01)\%$ the optical loss was calculated to $L_{RT} = (4400 \pm 1200)$ ppm. L_{RT} contains the entire optical loss that consists of absorption of and scattering at the mirror coatings as well as of the reflection and scattering P_{out} at the silicon substrate surface. The latter occurs twice per round trip because of entering and leaving the substrate, respectively. These reflections are caused by non-perfect plan-parallel end surfaces of the substrate, the wave-front distortion of the beam, scattering and limitations in fine-adjustment. The laser beam passes $2 \times 3.5 \text{ cm} / \cos(90^\circ - 74^\circ) = 7.28$ cm of the substrate per round trip. This results in a loss of $(4400 \pm 1200) \text{ ppm} / 7.28 \text{ cm} = (604 \pm 165) \text{ ppm/cm}$ and forms the upper limit for the absorption coefficient.

Nevertheless, the result of $70 \text{ ppm/cm} \leq \alpha \leq 770 \text{ ppm/cm}$ for silicon sample B suggests that the result obtained with sample A was typical for samples of the degree of purity involved.

5.4 Doping and Contaminations of the Material

Figure 5.6 shows the absorption result from the present work in comparison to earlier absorption results from spectral response measurements on solar cells taken from literature (purple dots and green triangles) [5.21, 5.22] and to a theoretical prediction of the absorption caused by the residual boron contamination of sample A [5.23].

Previous measurements [5.21, 5.22] found a much lower absorption of silicon than measured here. However, these results are also not consistent. Although no measurements at 1550 nm are available, the absorption measurements from Keevers and

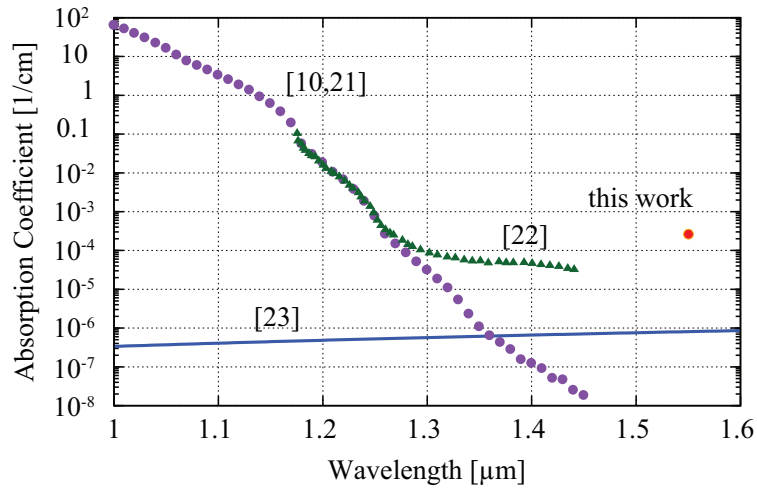


Figure 5.6: The purple dots and green triangles show band-band absorption values α_{BB} of silicon from literature [5.10,5.21] (purple dots) and [5.22] (green triangles). The free carrier absorption α_{FC} for a p-doping of $N = 2 \times 10^{12} / \text{cm}^3$ (sample A) was calculated using [5.23] (blue line). The red dot shows our result for sample A.

Green predict an absorption coefficient of $\alpha < 0.02$ ppm/cm at 1550 nm [5.10], while the measurements from Anagnostopoulos predict an absorption coefficient in the order of $\alpha \approx 50$ ppm/cm [5.22]. Green and Keevers explain their much lower absorption results by suggesting contamination of Anagnostopoulos' sample, due to doping or unintended foreign atoms. The assumed kind of contamination is, however, not specified in either of the two publications. The band-band absorption α_{BB} is the lower absorption limit for intrinsic crystalline silicon.

Even very low doping or contamination of the silicon samples can dominate the band-band absorption in the infrared region due to the free carrier absorption α_{FC} [5.23]. Since the semiconductor industry is by far the largest area of application for crystalline silicon, samples almost always are doped or at least slightly contaminated with the doping material that is normally used in the apparatus for the crystal growth. A specific resistivity of 11 k Ω cm, which is the specific resistivity of sample A, corresponds to a p-doping of $N = 2 \times 10^{12} / \text{cm}^3$ (N is the number of doping atoms). The number of doping atoms was calculated from the specific resistivity using [5.15]. The blue line in fig. 5.6 shows α_{FC} for a p-doping of $N = 2 \times 10^{12} / \text{cm}^3$ (blue line) calculated using [5.23]. α_{FC} and the number of doping atoms are proportional [5.24]. This theory predicts an absorption coefficient of $\alpha \approx 1$ ppm/cm for sample A, which is two orders of magnitude below our measurement results. Therefore, this doping theory does not explain the absorption of samples A and B. However, the theories for absorption due to doping generally are optimized for much higher doping than in our case. It is therefore possible that the prediction for residual-doping-induced absorption is not accurate, and further theoretical and experimental investigations are required to clarify this issue. Another

possible and plausible explanation for the deviation from the numbers published by Keevers and Green is that their photo-current measurements did not include effects that, while leading to optical absorption, would not lead to generation of carrier charges. Such photo-current measurements are thus not unconditionally transferable to optical absorption and may rather be used to derive a lower limit. Finally, the specific resistivity values provided by the manufacturers not necessarily provide information about all kinds of contamination present in the crystal and thus can not be used as an absolute measure for the crystal's purity. Further investigation of the residual contamination is required to derive a model for the dependence of the optical absorption on residual doping and contaminations, which are not reflected in the specific resistivity value.

5.5 Intensity-Dependent Absorption of Silicon

Besides doping affects, non-linear absorption processes are a possible explanation for the high absorption results. In the past, several works about multi-photon absorption processes in silicon were published [5.26–5.28]. According to the measurements presented in [5.28] the additional absorption due to two-photon absorption is 1 ppm/cm for a power density of 700 W/cm² as used for the absorption measurements on sample A. Therefore two-photon absorption was assumed to be negligible in our experiment.

Recently new results were reported from a beam deflection experiment where strong intensity-dependent absorption effects in silicon were observed and explained in a theoretical model based on two effects [5.29]. The first is that two-photon absorption creates free carriers which cause additional absorption. The second effect is the change of the refractive index due to the free carriers. The two processes are time-dependent because of diffusion and recombination of the free carriers. The time-scale changes with the doping of the material. The trend measured for the absorption to change with light intensity is represented well by the theoretical model, while the absolute absorption shows a discrepancy by approximately a factor of 6.

It is not known, whether non-linear absorption effects were relevant for the measurements presented in this chapter since the input power was constant. Decreasing the input power was not possible since the used input power of 22 mW was the lower limit for this setup to achieve a thermal effect. For a higher input power, the resonance peaks deformed in a way that could not be reproduced by the simulation. During the measurements the high thermal conductivity of silicon was assumed to cause this deformation and the effect was not further investigated. For an input power of 22 mW all recorded resonance peaks were perfectly reproducible by the simulation. Figure 5.7 a. shows such deformed resonance peaks for an input power of 63 mW. While the left flanks of the peaks match the fit, there is a strong discrepancy on the right flanks. Figure 5.7 b. shows the same measurement as Fig. 5.7 a. and a simulation for which a second order thermo refractive index d^2n/dT^2 was implemented as an additional parameter. A d^2n/dT^2 can be caused by a changing index of refraction as well as by a changing absorption. Now, the

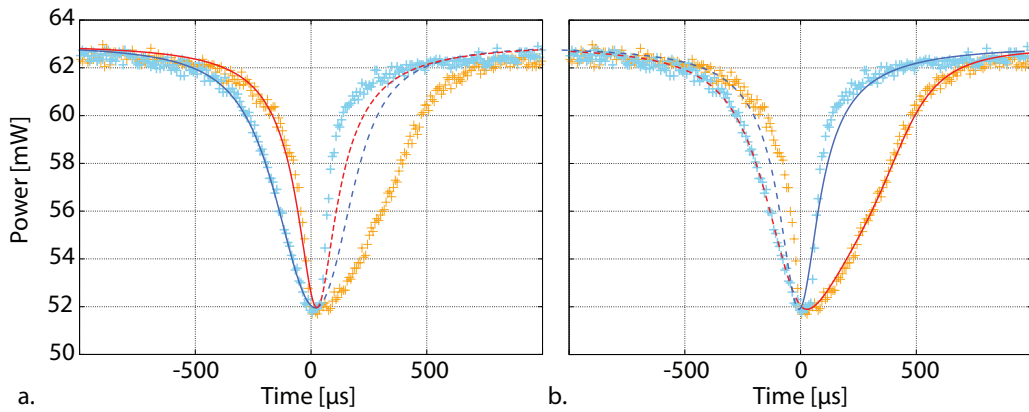


Figure 5.7: Deformed resonance peaks for an input power of 63 mW: a. While the left flanks of the peaks match the fit, there is a strong discrepancy on the right flanks. b. A second order thermo refractive index d^2n/dT^2 was implemented as an additional parameter, which allows a simulation of the trend of the right peak flanks.

trend of the right flanks can be reproduced by the simulation. This indicates a deformation due to a non-linear process like two-photon absorption at higher input powers. The matching simulated and measured left flanks of the peaks for the simulation without d^2n/dT^2 , and the matching right flanks of the peaks with d^2n/dT^2 indicate that the non-linear process takes place around the peak's maximum when high power is reached. For Fig. 5.7 b. a value for d^2n/dT^2 was chosen which led to a matching simulation. No quantitative prediction of the non-linear effect is possible.

5.6 Conclusion and Outlook

We measured the room temperature absorption coefficient of two silicon samples A and B which differed in manufacturer and crystal orientation. According to the manufacturer, sample A had a residual contamination by boron atoms with $N = 2 \times 10^{12} / \text{cm}^3$. For sample B, the specific resistivity was specified to be $< 5 \text{ k}\Omega\text{cm}$, this corresponds to a p-doping of $N < 4 \times 10^{12} / \text{cm}^3$.

For sample A, a result of $\alpha_A = (264 \pm 39) \text{ ppm/cm}$ was obtained. The consistent results for optical absorption and round trip loss indicate that no other process apart from the optical absorption contributes to the optical loss in a significant way.

For sample B, upper and lower limits of $70 \text{ ppm/cm} \leq \alpha_B \leq 770 \text{ ppm/cm}$ were derived for the absorption coefficient. This confirmed the result for sample A not to be extraordinarily high or low. Since uncoated, the measurement of sample B additionally proved that the absorption of sample A did not originate in the dielectric coatings but was due to absorption in the bulk substrate.

The results presented in Sec. 5.2.2 showed that within the error bars the absorption was identical with the cavity round-trip loss. Therefore a finesse measurement as used in

5.6 Conclusion and Outlook

Chapter 7 will be able to show, whether the absorption will significantly decrease with the intensity. Future experiments should concentrate on a decreasing intensity by several orders of magnitude into the regime where the intensity within the ET test-masses is envisaged.

Appendix A. Experiences with a Previous Substrate

The room temperature absorption measurement on sample A was in fact the second try to measure the absorption coefficient of silicon in the monolithic setup. In a first experiment we used an identical silicon substrate, that was cut from the same crystal as sample A and polished at the same time with identical specifications.

The first substrate was coated with a Si/SiO₂ coating. The coating procedure for this first substrate was ion plating. The design reflectivity was $R = 99.97\%$. The finesse was supposed to be $F = 10000$. This monolithic cavity did not operate successfully from the beginning. The impedance mismatch of the cavity was extremely high. In transmission very small resonance peaks of less than 1% of the input power were detected.

Later, the high impedance mismatch could be explained by coating absorption (see Chapter 8). The absorption of the coatings applied to the first monolithic cavity is not known. It was not possible to measure the absorption of the coatings applied to the silicon substrate due to the high impedance mismatch. Unfortunately no test-coatings on mirror substrates were prepared. The absorption can be assumed to be similar or even higher than the absorption of the coatings examined in Chapter 8 since the higher design reflectivity means more absorbing layers per coating stack. An absorption of 1000 ppm as obtained for the silicon coatings in Chapter 8 in both coatings would reduce the transmitted power to only 5% (simulation with `tksim`).

Additionally, losses due to defects in the crystal can increase the impedance mismatch by causing reflections and scattering. These defects could be developed during the crystal growth process or due to fast heating or cooling during the coating process. A substrate is heated up to about 500 °C while being coated in a ion plating procedure. To examine such defects in the crystal, an infra red (IR) camera was used. Figure 5.8 a. shows the substrate without a transmitting laser beam. No defects are visible. Figure 5.8 b. shows the substrate with a laser beam transmitting at Brewster's angle through flats polished onto the sides of the substrate. The laser beam is reflected many times within the substrate which can be explained by a non-parallelism of the flats that prevents from using Brewster's angle for the entering and exiting beam at the same time. Additionally, two "rings" are visible, looking as if the substrate consists of three cylinders. The picture shown in Fig. 5.8 c. was taken in the dark where the "rings" were better visible.

The reason for the non-working cavity was not definitely clarified but it is assumed that the coating absorption was the problem, maybe in combination with defects in the substrate. Therefore, for the second monolithic cavity (sample A), the substrate was tested for inexplicable reflections or partial beams and compared to a third substrate. The one with less inexplicable spots was chosen to be coated and used in the experiment. For this substrate SiO₂/Ta₂O₅-coatings were used. These coatings were produced with the ion beam sputtering (IBS) method, which does not exceed 100 °C. Additionally, for each coating run mirror substrates were added to have the option of checking the coating characteristics separately if necessary.

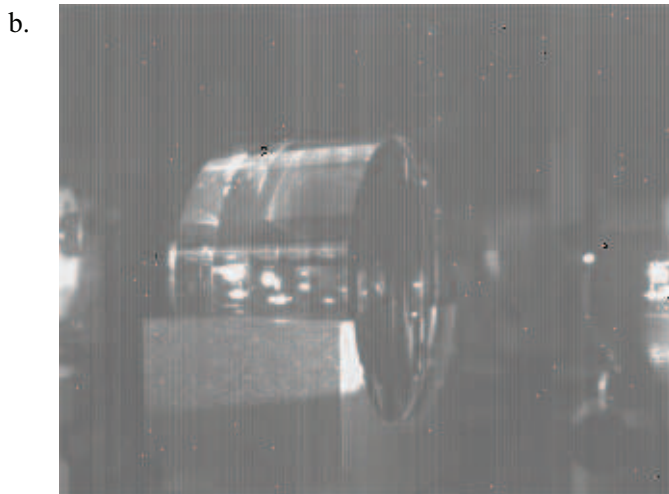
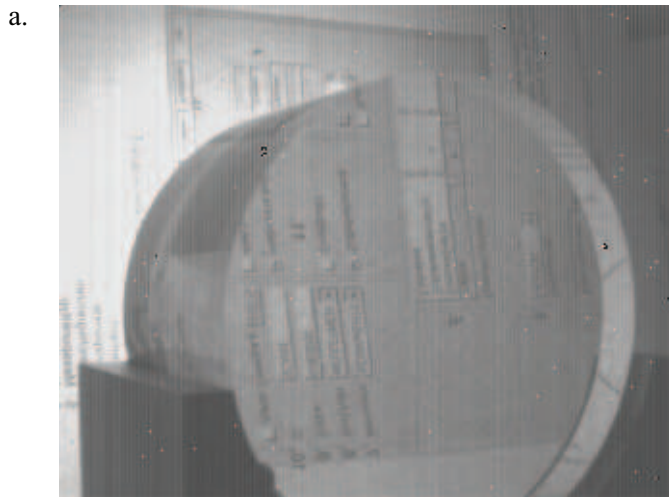


Figure 5.8: Photographs taken with an IR camera: a. Substrate without a transmitting laser beam. No defects are clearly visible. b. Substrate with a laser beam transmitting in Brewster angle. The reflections can be explained by a non-parallelism of the flats. Two “rings” are visible. The substrate appears to consist of three cylinders. c. In the dark the “rings” are better visible.

- 5.1 G. M. Harry (for the LIGO Scientific Collaboration)
Advanced LIGO: the next generation of gravitational wave detectors
Class. Quantum Grav **27**, 084006, 2010
- 5.2 H. Lück, C. Affeldt, J. Degallaix, A. Freise, H. Grote, M. Hewitson, S. Hild, J. Leong, M. Prijatelj, K. A. Strain, B. Willke, H. Wittel, K. Danzmann
The upgrade of GEO 600
J. Phys.: Conf. Ser. **228** 012012, 2010
- 5.3 T. Accadia et al.
Status and perspectives of the Virgo gravitational wave detector
J. Phys.: Conf. Ser. **203** 012074, 2010
- 5.4 S. D. Penn, A. Ageev, D. Busby, G. M. Harry, A. M. Gretarsson, K. Numata, P. Willems
Frequency and surface dependence of the mechanical loss in fused silica
Physics Letters A **352** 3–6, 2006
- 5.5 S. Hild, H. Lück, W. Winkler, K. Strain, H. Grote, J. Smith, M. Malec, M. Hewitson, B. Willke, J. Hough, K. Danzmann
Measurement of a low-absorption sample of OH-reduced fused silica
Applied Optics **45** 7269–7272, 2006
- 5.6 C: Schwarz et al.
Proceedings of ICEC22-ICMC2008 edited by Chang H-M et al. **978-89-957138-2-2**, 2009
- 5.7 R. Schnabel, M. Britzger, F. Brückner, O. Burmeister, K. Danzmann, J. Dück, T. Eberle, D. Friedrich, H. Lück, M. Mehmet, R. Nawrodt, S. Steinlechner, B. Willke

Bibliography

- Building blocks for future detectors: Silicon test masses and 1550 nm laser light
Journal of Physics Conference Series **228** 012029, 2010
- 5.8 R. Nawrodt, A. Zimmer, T. Koettig, C. Schwarz, D. Heinert, M. Hudl, R. Neubert, M. Thürk, A. Tünnermann, S. Nietzsche, W. Vodel, P. Seidel
High mechanical Q-factor measurements on silicon bulk samples
Journal of Physics: Conference Series **122** 012008, 2008
- 5.9 D. F. McGuigan, C. C. Lam, R. Q. Gram, A. W. Hoffman, D. H. Douglass
Measurements of the Mechanical Q of Single-Crystal Silicon at Low Temperatures
Journal of Low Temperature Physics **30** 621–629, 178
- 5.10 M. J. Keevers, M. A. Green
Absorption edge of silicon from solar cell spectral response measurements
Appl. Phys. Lett. **66** 174–176, 1995
- 5.11 M. Mehmet, S. Ast, T. Eberle, S. Steinlechner, H. Vahlbruch, R. Schnabel
Squeezed light at 1550 nm with a quantum noise reduction of 12.3 dB
Optics Express **19**, 25763–25772, 2011
- 5.12 The LIGO Scientific Collaboration
A gravitational wave observatory operating beyond the quantum shot-noise limit
Nature Physics **7**, 962–965, 2011
- 5.13 N. Lastzka, J. Steinlechner, S. Steinlechner, R. Schnabel
Measuring small absorptions by exploiting photothermal self-phase modulation
Applied Optics **49** 5391–5398, 2010
- 5.14 www.siltronic.com
- 5.15 S. M. Sze, J. C. Irvin
Resistivity, Mobility and Impurity Levels in GaAs, Ge, and Si at 300°K
Solid-State Electronics Pergamon Press **11** 599–602, 1968
- 5.16 E. Black
An introduction to Pound-Drever-Hall laser frequency stabilization
American Journal of Physics **69** 79–87, 2001
- 5.17 B. J. Frey, D. B. Leviton, T. J. Madison
Temperature dependent refractive index of silicon and germanium
arXiv:physics/0606168v1, 2006
- 5.18 M. J. Weber
Handbook of optical materials
CRC Press LLC Boca Raton (FL) USA, 2003

- 5.19 J. Komma, C. Schwarz, G. Hofmann, D. Heinert, R. Nawrodt
Thermo-optic coefficient of silicon at 1550nm and cryogenic temperatures
APPLIED PHYSICS LETTERS **101** 041905, 2012
- 5.20 MaTecK GmbH Jülich
www.mateck.de
- 5.21 M. A. Green, M. J. Keevers
Optical Properties of Intrinsic Silicon at 300K
Progress in Photovoltaics: Research and Applications **3** 189–192, 1995
- 5.22 C. Anagnostopoulos, G. Sadasiv
Fine Structure in the Optical-Absorption Edge of Silicon
Phys. Rev. B **7** 733–739, 1973
- 5.23 R. A. Soref, J. P. Lorenzo
All-Silicon Active and Passive Guided-Wave Components for $\lambda=1.3$ and $1.6\ \mu\text{m}$
Journal of Quantum Electronics **QE-22** 873–879, 1986
- 5.24 P. E. Schmid
Optical absorption in heavily doped silicon
Phys. Rev. B **23** 5531–5536, 1981
- 5.25 G. G. Macfarlane, T. P. McLean, J. E. Quarrington, V. Roberts
Fine Structure in the Absorption-Edge Spectrum of Si
Physical Review **111**, pp. 1245–1254, 1958
- 5.26 J. E. Geusic, S. Singh, D. W. Tipping, T. C. Rich
Three-photon stepwise optical limiting in silicon
Phys. Rev. Lett. **19**, no.1, 1967
- 5.27 J. F. Reintjes, J. C. McGroddy
Indirect Two-Photon Transitions in Si at $1.06[\mu\text{m}]$
Phys. Rev. Lett. **30**, pp. 901–903, 1973
- 5.28 A. D. Bristow, N. Rotenberg, H. M. van Driel
Two-photon absorption and Kerr coefficients of silicon for 850–2200 nm
Appl. Phys. Lett. **90**, 191104, 007
- 5.29 J. Degallaix, D. Forest, C. Carcy, L. Pinard, R. Flaminio
What we learned from the silicon absorption measurement at LMA
Talk, 4th Einstein Telescope Symposium, 2012

Absorption Measurements on PPKTP at 775 nm and 1550 nm

The work presented in this Section is published in [6.1].

The efficient generation of second-harmonic light and squeezed light requires non-linear crystals that have low absorption at the fundamental and harmonic wavelengths. In this work the photo-thermal self-phase modulation technique is exploited to measure the absorption coefficient of periodically poled potassium titanyl phosphate (PPKTP) at 1550 nm and 775 nm. The measurement results are (84 ± 40) ppm/cm and (127 ± 24) ppm/cm, respectively. We conclude that the performance of state-of-the-art frequency doubling and squeezed light generation in PPKTP is not limited by absorption.

6.1 Introduction

There is a multitude of applications for squeezed light. Examples are fundamental research in quantum physics [6.2–6.4], the realization of quantum information protocols [6.5, 6.6], and the sensitivity improvement of gravitational wave detectors (GWDs) [6.7]. In 2010, a squeezed light laser operating at a wavelength of 1064 nm was implemented in GEO 600 [6.8]. Design studies of future generations of GWDs consider the application of strongly squeezed light at 1064 nm and 1550 nm [6.9]. State-of-the-art setups for squeezed light generation require second-order nonlinear crystals that have low loss at the fundamental (squeezed) wavelength as well as at the second-harmonic wavelength that pumps the parametric squeezing process. The non-linear medium is placed inside a singly or doubly resonant optical cavity [6.10] defining the so-called squeezing resonator. Typical non-linear media are magnesium doped lithium niobate ($\text{MgO}:\text{LiNbO}_3$) [6.11]

and periodically poled potassium titanyl phosphate (PPKTP) [6.8, 6.12]. The squeezing factor increases with the secondharmonic pump intensity, however, it is ultimately limited by optical losses which include the quantum efficiency of the photo-electric detector, propagation loss, as well as the escape efficiency of the squeezing resonator [6.13]. To give an example, a total optical loss of 10 % limits the nonclassical noise suppression to a maximum of 10 dB below the shot noise variance. The highest squeezing level demonstrated so far is 12.7 dB at a wavelength of 1064 nm [6.12]. The squeezing resonator's escape efficiency is given by [6.13]

$$\eta = \frac{T}{T + L_{\text{RT}}}, \quad (6.1)$$

where T is the transmission of the resonator's coupling mirror and L_{RT} is the resonator's round-trip loss with contributions from non-perfect intra-cavity anti-reflection (AR) coatings, from general coating absorption and scattering, and from the bulk absorption of the non-linear crystal. Since a reduction of L_{RT} allows a reduction of T and thus a reduction of the external pump intensity, the availability of non linear materials with low absorption is of high interest for the efficient generation of strongly squeezed light. The efficient generation of second-harmonic light sets the same requirement to non linear materials. The highest efficiency for frequency doubling achieved so far is 95 % for continuous-wave light at 1550 nm [6.14]. In this work we report on the measurements of the absorption coefficient of PPKTP at 775 nm and at 1550 nm exploiting the photo-thermal self-phase modulation technique [6.15].

6.2 Experimental Setups

The photo-thermal self-phase modulation technique is an absorption measurement method that exploits the deformation of cavity resonance peaks due to absorption in the intra-cavity bulk material [6.15] or in the coating of the cavity's in-coupling mirror [6.16]. The resonance peaks are observed while changing the cavity length with a piezo-electric transducer (PZT) attached to one of the cavity mirrors. For zero absorption the resonance peaks are identical for external shortening and lengthening. The situation changes when absorption takes place. Then, for most materials, heating leads to thermal expansion and to a change of the refractive index. In the case of PPKTP, the cavity round-trip length increases as soon as the intra-cavity light power builds up. For an external lengthening the resonance peak becomes narrower, for an external shortening the resonance peak becomes broader. Fig. 6.1 shows four example measurements of resonance peaks detected in reflection of a Fabry-Perot (a. and b.) and a bow-tie cavity (c. and d.) and corresponding simulations. Shown are peaks with no thermal effect (a.), low thermal effect (c.) and a clearly visible thermal effect (b. and d.). While the peaks in Fig. 6.1a. show no thermal effect, they are identical for both scan directions. For peaks with thermal effect, an external shortening of the cavity forms broad peaks (simulation: light-blue line, measurement: red dots) and an external lengthening of the cavity forms narrow

Table 6.1: Material and geometric parameters of the bow-tie cavity and the half-monolithic cavity used for the simulations.

Geometric parameters	775 nm	1550 nm	References
Beam waist ω_0	27.6 μm	30.2 μm	
Crystal length L	9.3 mm	10 mm	
Crystal radius R	1.5 mm	1.5 mm	
Air gap	24 mm	832 mm	
Material parameters			
Index of refraction n	1.85	1.82	[6.17]
Thermal refr. coeff. dn/dT	$16.9 \times 10^{-6}/\text{K}$	$10.9 \times 10^{-6}/\text{K}$	[6.18]
Specific heat c		726 J/(kg K)	[6.19]
Density ρ_{KTP}		2945 kg/m ³	[6.20]
Thermal expansion a_{th}		$0.6 \cdot 10^{-6}/\text{K}$	[6.19]
Thermal conductivity k_{th}		2.23 W/(m K)	[6.19]
Material emissivity ϵ		1.0 ^a	

^a $0.0 < \epsilon \leq 1.0$ are the boundaries for the thermal emissivity. For our systems the value of this parameter is not relevant since $R \gg \omega_0$ and therefore surface radiation is negligible.

peaks (simulation: orange line, measurement: dark-blue dots). The thermal effect increases with increasing input laser power and vanishes for very low power. Changing the scan velocity also has an effect since faster scanning results in less deposited energy. For an increasing scan velocity the thermal effect thus decreases. Material parameters such as the heat conductivity also need to be considered to quantitatively describe the deformation of the resonance peak.

Solid lines in Fig. 6.1 correspond to our quantitative simulation using the parameters from Table 6.1 as well as the absorption coefficient α as fitting parameters. The simulation also requires the cavity mirror reflectivities R_1 and \widetilde{R}_2 , which are also determined from these measurements. As a consistency check R_1 and \widetilde{R}_2 additionally were determined in independent measurements which show no thermal effect. \widetilde{R}_2 is the *effective* reflectivity of the end-mirror. It includes all cavity round-trip losses apart from the transmission of the in-coupling mirror. The values for the material parameters were taken from literature [6.17–6.20]. The time axis of the measurements is calibrated using frequency markers in terms of phase-modulation sidebands generated by an electro-optical modulator. These sidebands are slightly outside the window shown here. Using frequency markers for each measurement also minimizes errors caused by the hysteresis of the PZT. A set of fitting parameters is then found by minimizing the standard deviation

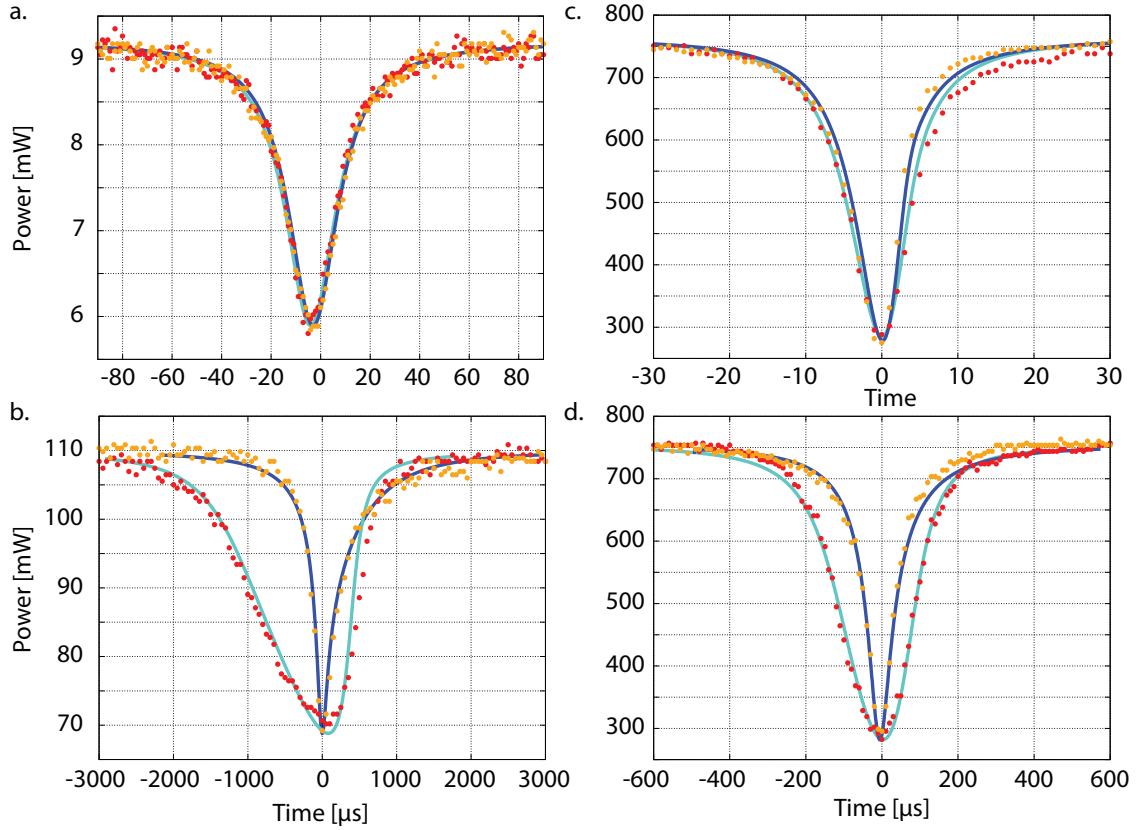


Figure 6.1: Measured and simulated cavity resonance peaks for an external lengthening (dark-blue line and orange dots) and external shortening (light-blue line and red dots) of the cavity (dots: measurements, lines: corresponding simulations). a. and b. were measured with a Fabry-Perot cavity setup at 775 nm (cavity line-width ≈ 10 MHz) using an input power of 9 mW at a scan frequency of 550 Hz (a.) and 110 mW at 15 Hz (b.). c. and d. were measured with a bow-tie cavity setup at 1550 nm (cavity line-width ≈ 750 kHz) at an input power of 760 mW at scan frequencies of 149 Hz (c.) and 11 Hz (d.). For low power and a high scan frequency no thermal effect occurs (a.). For slower scan frequencies and higher powers the narrow peaks form for an external lengthening and the broad peaks for an external shortening of the cavity (b.-d.). From those measurements we derived the absorption coefficients as summarized in Fig. 6.3.

between the measurement data and the simulation employing a Nelder-Mead algorithm. To minimize errors due to transient disturbances, multiple measurements of resonance peaks were performed. Also, the scanning speed as well as the light power was varied, providing a self-consistency check of our evaluation.

In the following sections the experimental setups for the absorption measurements at both wavelengths and the obtained results are presented. For the absorption measurements existing SHG and squeezing cavities were used, which resulted in different cavity types and simultaneously demonstrates the manifold application possibilities of the measurement method.

For the 775 nm absorption measurement we used a half-monolithic standing wave cavity, while for the 1550 nm absorption measurement a traveling-wave bow-tie cavity was used. In a standing wave setup, the absorption depends on the position of the substrate relative to the emerging node-antinode pattern [6.21]. However, this effect is negligible for our measurements, since the substrate dimensions are much larger than the wavelength λ . Traveling-wave cavities generally have the advantage that the reflected beam is easily accessible for detection, since it does not coincide with the incoming beam. Another advantage is that disturbances due to parasitic cavities between the anti-reflection coating and the high reflection coating of the coupling mirror are less likely. Standing wave cavities on the other hand can be realized in a more compact way minimizing acoustic vibrations. In the work presented here, however, both cavity types turned out to be suitable for absorption measurements.

6.2.1 Experimental Setup and Results at 775 nm

For the absorption measurements at a wavelength of $\lambda = 775$ nm we used a half-monolithic standing-wave cavity. Fig. 6.2a. shows the schematic of our experiment. The beam splitter (BS) reflected most of the light towards the in-coupling mirror M_1 . The PPKTP crystal was manufactured by Raicol [6.22] and had a curved end surface with a high reflection (HR) coating applied to it. The other end surface was plane and AR coated. The cavity was formed by the in-coupling mirror M_1 , which was placed 24 mm in front of the AR coating of the crystal, and the crystal's HR coating. A photo diode (PD) detected the light power $P_{\text{ref}}(t)$ which was reflected from the in-coupling mirror M_1 and partly transmitted by the BS. The input light carried phase modulation sidebands imprinted by an EOM. The modulation frequency was chosen to be 101.25 MHz, which is outside the cavity line width of ≈ 11 MHz, so the crystal could cool down before the sidebands became resonant. The PD's photo current was demodulated at the EOM modulation frequency by means of a double-balanced mixer to generate frequency markers in terms of a Pound Drever Hall (PDH) error signal [6.23]. This way we were able to precisely calibrate the motion of the piezo driven mirror M_1 around the cavity resonance.

Altogether we performed 13 individual measurements using three different input powers of 9 mW, 37 mW and 110 mW. The scan frequencies were varied by almost a factor

6 Absorption Measurements on PPKTP at 775 nm and 1550 nm

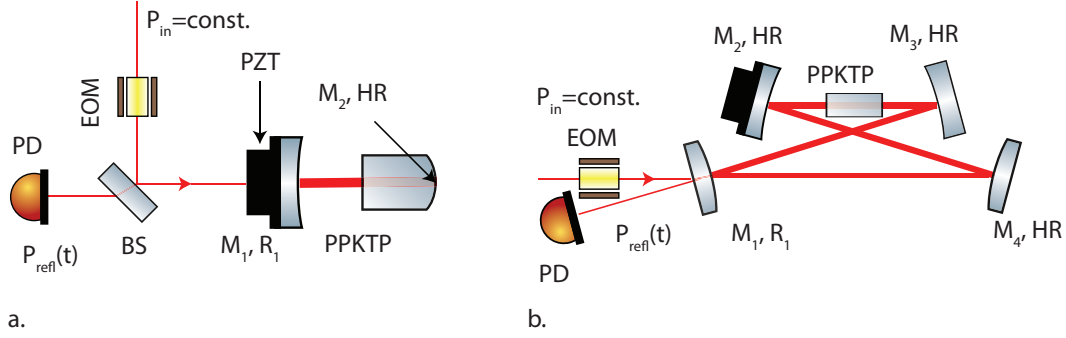


Figure 6.2: a. half-monolithic cavity setup for the absorption measurement at 775 nm: Mirror M_1 and the HR coating on the PPKTP crystal's curved end surface formed the cavity. The length of the cavity was scanned with the PZT onto which M_1 was mounted. A photo diode (PD) detected resonance peaks $P_{\text{refl}}(t)$ in reflection of M_1 . b. Bow-tie cavity setup for the absorption measurement at 1550 nm: The in-coupling mirror M_1 and three HR-coated mirrors formed a bow-tie ring-cavity. The PPKTP crystal was placed within the small waist between the concave mirrors M_2 and M_3 . M_2 was moved by a PZT. The PD detected the resonance peak $P_{\text{refl}}(t)$ in reflection of M_1 . In both setups the beam passed an EOM for imprinting sidebands before entering the cavity for the calibration of the mirror motion.

of a hundred. 6 of the 13 measurements showed a strong thermal effect and permitted to obtain an absorption coefficient as well as the reflections of R_1 and \widetilde{R}_2 . From the remaining 7 measurements only R_1 and \widetilde{R}_2 were independently determined and were found to be in agreement with the first 6 measurements. Figure 6.3 shows the results of the individual measurements of the absorption coefficient α (purple dots, right graph) as well as their mean value (thick yellow line) and their standard deviation (dashed yellow lines) of $\alpha_{775\text{nm}} = (127 \pm 24) \text{ ppm/cm}$. The result for the power reflectivity of M_1 was $R_1 = (98.33 \pm 0.08) \%$, which agreed with the specified design value of $R_1 = (98.5 \pm 0.4) \%$. The result for the effective reflectivity was $\widetilde{R}_2 = (99.76 \pm 0.01) \%$. The designed reflectivity for the HR coating was about $R_2 = 99.95 \%$. The residual loss of about 1900 ppm per round-trip due to absorption, scattering and reflection at the AR-coating is compatible with the specification of the AR coating of $R < 0.1 \%$.

The design reflectivity R_1 of the in-coupling mirror of this setup at 1550 nm was 90 %, while the end-surface of the crystal was HR coated. Due to this strong impedance mismatch of the mirror reflectivities only $\approx 7 \%$ of the laser power are transmitted into the cavity at 1550 nm at resonance instead of $\approx 30 \%$ at 775 nm. The resolution of the peaks at 1550 nm becomes inferior compared to 775 nm and therefore the measured peaks become more noisy. Hence, a setup with more suitable parameters was used for the measurement at 1550 nm.

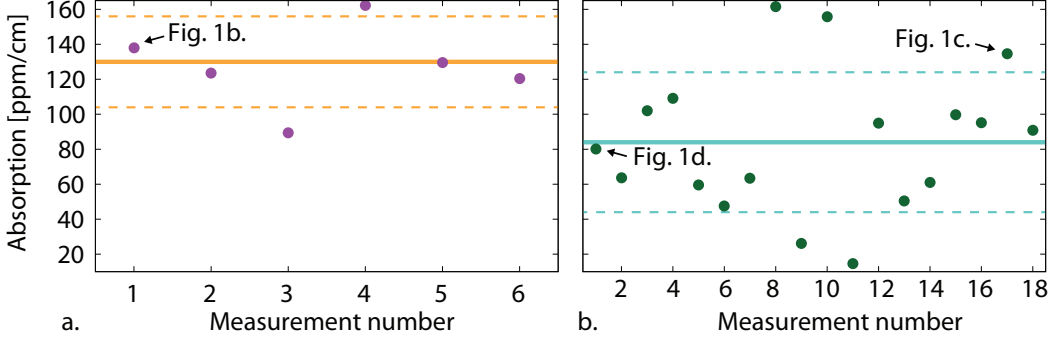


Figure 6.3: The dots show the absorption coefficient obtained from individual measurements at 775 nm (left) and at 1550 nm (right). The mean value (line) and standard deviation (dashed lines) of the absorption coefficient are $\alpha_{775\text{nm}} = 127 \pm 24$ ppm/cm and $\alpha_{1550\text{nm}} = 84 \pm 40$ ppm/cm. The absorption results corresponding to the peaks shown in Fig. 6.1 are labeled.

6.2.2 Experimental Setup and Results at 1550 nm

The absorption measurement at a wavelength of 1550 nm was performed in a four mirror bow-tie ring-cavity setup. Fig. 6.2b. shows a schematic of the experiment. Mirror M_1 , which had a design power reflection of 99%, couples the light into the cavity. The remaining three mirrors were HR coated. While M_1 and M_4 were convex, M_2 and M_3 were concave forming a waist of $30.5 \mu\text{m}$ that was located in the centre of the PPKTP crystal. The latter was again produced by Raico1 [6.22]. Both crystal surfaces were AR-coated. The optical round-trip length of the cavity was 832 mm.

The measurement was performed using p-polarized light to avoid the phase matching condition for second-harmonic generation. The p-polarization also had the advantage that the high reflective cavity mirrors showed a slightly reduced reflectivity which improved the signal-to-noise ratio of our measurement due to a reduced impedance mismatch. The detection of the resonance peaks and the frequency markers was identical to the procedure described in subsection 6.2.1.

From this setup 18 individual measurements were recorded. We used a constant input power of 760 mW, but varied the scan frequency from 11 Hz up to 200 Hz. The measurements at 149 Hz and 11 Hz are shown in Fig. 6.1c. and d.

The time axis of Fig. 6.1d. shows that the scan frequency of 11 Hz corresponded to a scanning time of about $200 \mu\text{s}$ per resonance peak at full width half maximum (FWHM). The scan amplitude was not changed within the series of measurements so the scanning time per FWHM changed proportional to the scan frequency. All 18 measurements showed a thermal effect and allowed to obtain an absorption coefficient besides R_1 and \widehat{R}_2 .

The mean value and standard deviation for the absorption coefficient were $\alpha_{1550\text{nm}} = (84 \pm 40)$ ppm/cm. This non-monolithic setup with a very large round-trip length in

combination with the small waist is very susceptible to acoustic and thermal fluctuations, which most likely caused the large error bar. The result for the reflection of M_1 was $R_1 = (99.03 \pm 0.10)\%$ which agrees with the design value of 99%. The result for the effective reflection was $\widetilde{R}_2 = (99.76 \pm 0.04)\%$. \widetilde{R}_2 again included all cavity round-trip losses, which are the absorption of the PPKTP crystal, the reflection of the two AR coatings, the transmission of the three HR mirror coatings as well as the absorption and scattering of all four mirrors. A loss of $1 - \widetilde{R}_2 \approx 4000$ ppm per round trip is a reasonable result for p-polarized light.

Our bow-tie cavity is usually operated with s-polarized light at 775 nm as well as at 1550 nm for which the PPKTP crystal is quasi-phase-matched. To be able to compare the crystal's absorption with other cavity round trip losses for s-polarized light, we performed another series of eight individual loss measurements. The polarization was rotated to s-pol and the light power was strongly reduced so no thermal deformation occurred. The crystal's temperature was tuned far away from the quasi-phase-matching regime to avoid SHG. The result for the effective reflection is $\widetilde{R}_2 = (99.935 \pm 0.008)\%$ which corresponds to a round-trip loss of (650 ± 80) ppm. Thus, for our cavity operated in s-pol the absorption of the crystal of 84 ppm/cm (crystal length: 1 cm) is not the dominating loss source.

6.3 Conclusion

In this work the absorption coefficient of PPKTP [6.22] was measured at the quasi-phase matched wavelengths of 775 nm and 1550 nm using the photo-thermal self-phase modulation technique. We used two almost identical crystals of 10 mm and 9.3 mm length in two geometrically different cavity setups, a half-monolithic standing-wave cavity and a traveling-wave bow-tie cavity. The results for the absorption coefficients are $\alpha_{775\text{nm}} = (127 \pm 24)$ ppm/cm and $\alpha_{1550\text{nm}} = (84 \pm 40)$ ppm/cm. The error bars correspond to one standard deviation excluding systematic effects due to errors in the material parameters. The latter are, however, estimated to be smaller than our statistical error bars. If such a crystal is used in an otherwise lossless squeezing resonator with an in-coupling reflectivity of $R \approx 90\%$, the escape efficiency would be as high as $\eta > 99.9\%$. With this value, a loss of merely 1% is associated, thus allowing the generation and observation of squeezing strengths and second harmonic conversion efficiencies beyond what has been achieved so far. The highest squeezing factor at 1550 nm observed so far is 12.3 dB [6.24] with a total optical loss of the setup of 3.5%. The highest efficiency for external continuous-wave second harmonic generation so far is 95% [6.14]. We conclude that the bulk absorption of PPKTP, by far, does not limit state-of-the-art squeezed light and second-harmonic generation at this wavelength.

- 6.1 J. Steinlechner, S. Ast, C. Krüger, A. Pal Singh, T. Eberle, V. Händchen, R. Schnabel
Absorption Measurements of Periodically Poled Potassium Titanyl Phosphate (PP-KTP) at 775 nm and 1550 nm *Sensors* **13**, pp. 565–573, 2013
- 6.2 Z. Y. Ou, S. F. Pereira, H. J. Kimble, K. C. Peng
Realization of the Einstein-Podolsky-Rosen Paradoxon for Continuous Variables
Phys. Rev. Lett. **68**, pp. 3663–3666, 1992
- 6.3 W. P. Bowen, R. Schnabel, P. K. Lam
Experimental characterization of continuous-variable entanglement
Phys. Rev. A **69**, pp. 012304–1–012304–17, 2004
- 6.4 V. Händchen, T. Eberle, S. Steinlechner, A. Samblowski, T. Franz, R. F. Werner, R. Schnabel
Observation of one-way Einstein-Podolsky-Rosen steering
Nature Photonics **6**, pp. 596–599, 2012
- 6.5 A. Furusawa, J. L. Sørensen, S. L. Braunstein, C. A. Fuchs, H. J. Kimble, E. S. Polzik
Unconditional Quantum Teleportation
Science **282**, pp. 706–709, 1998
- 6.6 T. C. Ralph
Continuous variable quantum cryptography
Phys. Rev. A **61**, 010303(R), 2000
- 6.7 R. Schnabel, N. Mavalvala, D. E. McClelland, P. K. Lam
Quantum metrology for gravitational wave astronomy
Nature Communications **121**, pp. 1–10, 2010

Bibliography

- 6.8 The LIGO Scientific Collaboration
A gravitational wave observatory operating beyond the quantum shot-noise limit
Nature Physics **7**, pp. 962–965, 2011
- 6.9 S. Hild, S. Chelkowski, A. Freise, J. Franc, N. Morgado, R. Flamino, R. DeSalvo
A xylophone configuration for a third-generation gravitational wave detector
Class. Quantum Grav. **27**, 015003 (8pp), 2010
- 6.10 R. W. Boyd
Nonlinear Optics, Academic Press: 2008
- 6.11 H. Vahlbruch, M. Mehmet, S. Chelkowski, B. Hage, A. Franzen, N. Lastzka, S. Goßler, K. Danzmann, R. Schnabel
Observation of Squeezed Light with 10-dB Quantum-Noise Reduction
Phys. Rev. Lett. **100**, 033602 (4pp), 2008
- 6.12 T. Eberle, S. Steinlechner, J. Bauchrowitz, V. Händchen, H. Vahlbruch, M. Mehmet, H. Müller-Ebhardt, R. Schnabel
Quantum Enhancement of the Zero-Area Sagnac Interferometer Topology for Gravitational Wave Detection
Phys. Rev. Lett. **104**, 251102 (4pp), 2010
- 6.13 Y. Takeno, M. Yukawa, H. Yonezawa, A. Furusawa
Observation of -9dB quadrature squeezing with improvement of phase stability in homodyne measurement
Optics Express **157**, pp. 4321–4327, 2007
- 6.14 S. Ast, R. Moghadas Nia, A. Schönbeck, N. Lastzka, J. Steinlechner, T. Eberle, M. Mehmet, S. Steinlechner, R. Schnabel
High-efficiency frequency doubling of continuous-wave laser light
Optics Letters **36** 17, pp. 3467–3469, 2011
- 6.15 N. Lastzka, J. Steinlechner, S. Steinlechner, R. Schnabel
Measuring small absorptions by exploiting photothermal self-phase modulation
Applied Optics **49**, pp. 5391–5398, 2010
- 6.16 J. Steinlechner, L. Jensen, C. Krüger, N. Lastzka, S. Steinlechner, R. Schnabel
Photothermal self-phase modulation technique for absorption measurements on high-reflective coatings
Applied Optics **51**, pp. 1156–1161, 2012
- 6.17 T. Y. Fan, C. E. Huang, B. Q. Hu, R. C. Eckardt, Y. X. Fan, R. L. Byer, R. S. Feigelson
Second harmonic generation and accurate index of refraction measurements in flux-grown KTiOP_4
Applied Optics **26**, pp. 2390–2394, 1987

- 6.18 W. Wiechmann, S. Kubota
Refractive-index temperature derivatives of potassium titanyl phosphate
Optics Letters **18**, pp. 1208–1210, 1998
- 6.19 J. D. Bierlein, H. Vanherzeele, H
Potassium titanyl phosphate: properties and new applications
J. Opt. Soc. Am. B **6**, pp. 622–633, 1989
- 6.20 KTP Crystals for SHG
www.quantumtech.com
- 6.21 D. Friedrich, H. Kaufer, T. Westphal, K. Yamamoto, A. Sawadsky, F. Y. Khalili,
S. Danilishin S. Gößler, K. Danzmann, R. Schnabel
Laser interferometry with translucent and absorbing mechanical oscillators
New Journal of Physics **213**, 093017, 2011
- 6.22 Raicol, Israel
www.raicol.com
- 6.23 E. D. Black
An introduction to Pound-Drever-Hall laser frequency stabilization
American Journal of Physics **69**, pp. 79–87, 2001
- 6.24 M. Mehmet, S. Ast, T. Eberle, S. Steinlechner, H. Vahlbruch, R. Schnabel
Squeezed light at 1550nm with a quantum noise reduction of 12.3 dB
Optics Express **19**, pp. 25763–25772, 2011

Optical Absorption Measurements on Thin SiN Membranes

Third generation gravitational wave detectors (GWDs) such as the Einstein Telescope (ET) are expected to be limited by radiation pressure noise (RPN) in the low frequency detection band [7.1]. Up to now the occurrence of RPN in GWDs is merely a theoretical prediction. Recently, RPN was first measured in a cryogenic cavity setup using a nanogram membrane oscillator [7.2] and various experiments work on measuring and characterizing this noise source [7.3–7.5]. In our group a Michelson-Sagnac interferometer including a translucent silicon nitride (SiN) membrane with sub-wavelength thickness is used for this purpose [7.5]. Low optical absorption of the membrane is necessary, since heating caused by optical absorption limits quantum opto-mechanical experiments at low temperatures. Therefore, [7.5] discusses the absorption behavior of SiN membranes and makes theoretical predictions of the absolute optical absorption for a laser wavelength of 1064 nm. These predictions are plotted in Fig. 7.1. For membranes with sub-wavelength thickness the absorption differs for a membrane position within a traveling wave (orange line) and the node (dark blue line) or anti-node (light blue line) of a standing wave. When the membrane thickness converges to the laser wavelength the node absorption converges to the anti-node absorption. The red line shows the absorption if geometrical effects are neglected.

In this chapter, measurements with an infra red (IR) camera from *DIAS Infrared* [7.6] are presented. These measurements show the temperature on the surface of SiN membranes when heated with a laser beam at various wavelengths. Since the measurements were performed in air, they do not deliver absolute temperatures of the membranes comparable to the opto-mechanical experiments performed in vacuum, but relative changes for three different membrane thicknesses and five different laser wavelengths between 285 nm and 2 μ m. For an absolute calibration of the membranes' absorption they were placed in cavities at Brewster's angle and loss measurements at 1064 nm and 1550 nm

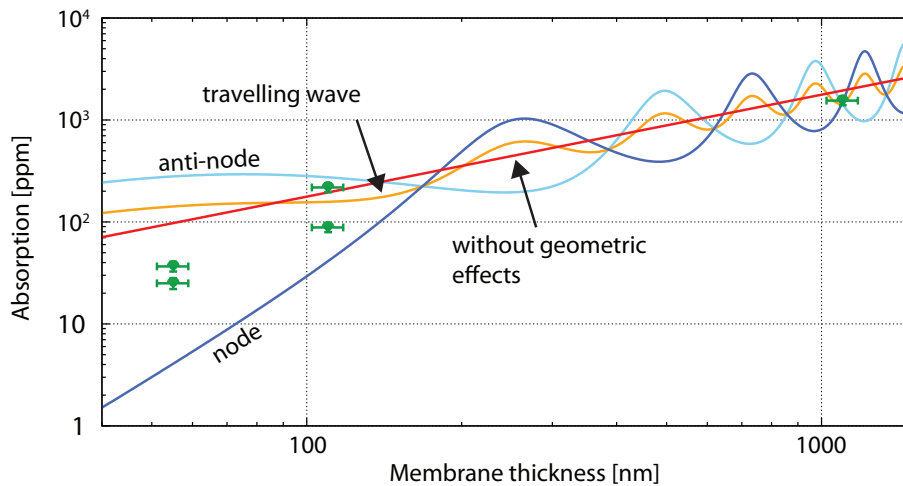


Figure 7.1: Theoretical model for the absorption of thin membranes at 1064 nm from [7.5]: For membranes with sub-wavelength thickness the absorption differs for a membrane position within a traveling wave (orange line) or the node (dark blue line) or anti-node (light blue line) of a standing wave. The red line shows the absorption without geometric effects. The green dots present the experimental results from the cavity round-trip loss measurements.

were performed.

In the experiments presented in the following sections, nine membranes were used: three at each of the thicknesses 50 nm, 100 nm and 1000 nm. The membranes are named after their thickness and numbered serially. They were manufactured at *Norcada Inc.* [7.7]

7.1 Measurements of the Membrane Temperature with an IR Camera

For temperature measurements of the membranes' surfaces, the membranes were placed at Brewster's angle in cavities locked on resonance (one optimized for each wavelength) (see Fig. 7.5). This approach had the advantage of exact knowledge of the beam waist and position. The round-trip power was calculated from measurements of the mirror reflectivities. For details see Section 7.2. To measure the temperature the IR camera was placed under normal incidence to the membrane surface in a distance of about 12 cm. The temperature was measured for two membranes at 1064 nm (100 nm no1 and 1000 nm no3) and for four membranes at 1550 nm (50 nm no2, 100 nm no1 and 1000 nm no2 & no3). Figure 7.2 shows a temperature profile for membrane 1000 nm no3 at 1064 nm. In this picture, the temperature increase ΔT is about 8 K, which was calculated from the temperature difference from the hottest point (pixel) in the middle of the spot to a point

7.1 Measurements of the Membrane Temperature with an IR Camera

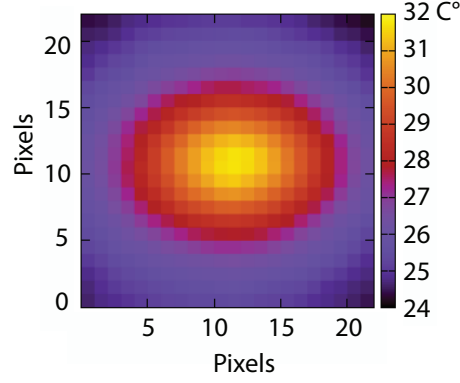


Figure 7.2: Temperature profile for membrane 1000 nm no3 in the locked cavity with a power of about 22.6 W at a wavelength of 1550 nm. Due to Brewster's angle the beam profile was elliptical. The absolute absorbed power was calculated to 6.1 mW. The vertical beam diameter on the membrane was 600 μm . x- and y-axes are given in camera pixels.

on the membrane far outside of the beam radius. ΔT was measured for the different membranes with varied laser power. The temperature ΔT with intra-cavity power is illustrated in Fig. 7.3 and was linearly fitted using an equation of the form

$$\Delta T(P) = a \times P. \quad (7.1)$$

The error bars for ΔT are 10 % due to camera specifications. The error bars for the power measurements are 5 % due to the specifications for the absolute error of the power meter. The beam waist at the two wavelengths was not identical but $w_{1064} = 248.5 \mu\text{m}$ and $w_{1550} = 301.9 \mu\text{m}$ resulting in a ratio of

$$\frac{I_{1550}}{I_{1064}} = \frac{A_{1550}}{A_{1064}} = 1.48 \quad (7.2)$$

in the intensities for identical powers, where I is the intensity and A the area of the beam at each wavelength.

To compare the heating for the two wavelengths, the slope factor a of the measurements at 1550 nm was normalized to the intensity at 1064 nm. a_{1064} and $1.48 \times a_{1550} = a'_{1550}$ are listed in Tab. 7.1. For the two membranes measured at both wavelengths, a decrease of the coefficient a of ≈ 10 (11 for membrane 100nm no 1 and 9.7 for membrane 1000nm no 3) was found when changing the wavelength from 1064 nm to 1550 nm. While this result is consistent for the two membranes measured at both wavelengths, a linear correlation of temperature with membrane thickness could not be observed. Most likely this is due to the large surface of the heated volume, where convection takes places. This means that

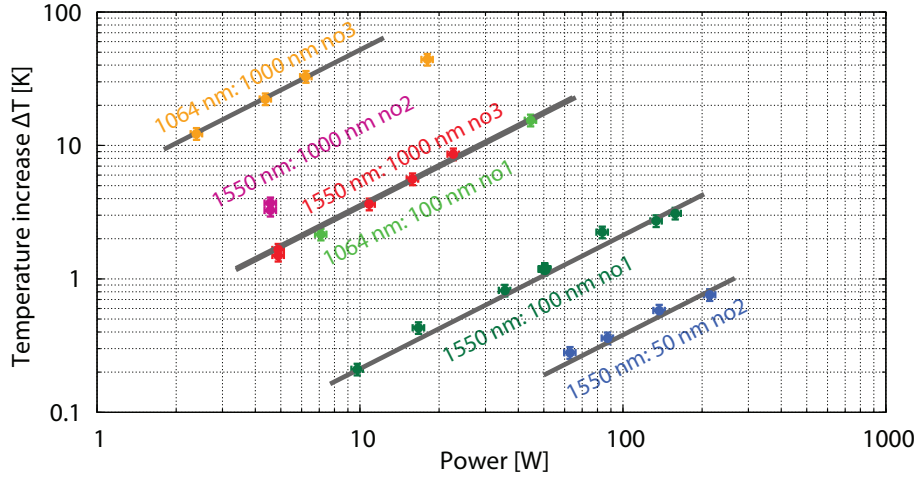


Figure 7.3: Temperature increase with cavity round-trip power for different membranes at 1064 nm and 1550 nm.

the temperature increase with membrane thickness is stronger than linear. A further reason can be capillary damages of the membranes or manufacturing tolerances. Both effects were hard to observe.

Additional temperature profiles were measured at 285 nm, 532 nm and $2\ \mu\text{m}$. Since these measurements took place in existing experiments with limited space, no cavity setups were used. The available laser power was sufficiently high in all cases even without a cavity. However, the knowledge of the beam diameter was less accurate than for the cavity setups and is assumed to have an error of 10%. Further, less measurements per wavelength could be performed. For all measurements apart from the 532 nm measurement, membrane 1000 nm no3 was used. At 532 nm this membrane was replaced by 100 nm no3. (Membrane 1000 nm no3 has been broken before the last measurement took place.) For the four wavelengths $\Delta T(P)$ was measured and a was fitted. a was normalized to the intensity on the membrane surface at 1550 nm via $a' = a \times \frac{A_x}{A_{1550}}$. The ratio of the beam area and a are listed in Tab. 7.2.

To calibrate the relative absorptions obtained from the surface temperature measurements, cavity round-trip loss measurements with different membranes at 1064 nm and 1550 nm were performed. These measurements delivered the absolute absorption of the membranes and are presented in the following Section 7.2.

7.2 Absorption Measurements at 1064 nm and 1550 nm

A thermal absorption measurement using `tksim` as described in Chapter 3 is not possible for thin membranes with subwavelength thickness. To cause a clearly visible thermal deformation of cavity resonance peaks, a significant expansion of the optical substrate

7.2 Absorption Measurements at 1064 nm and 1550 nm

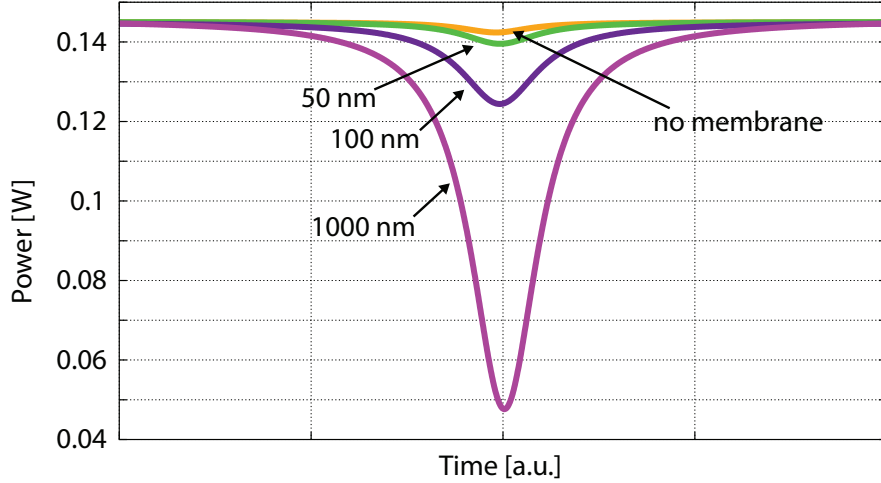


Figure 7.4: Reflected resonance peaks for a wavelength of 1064 nm: Cavity without membrane (orange line) and with 50 nm (green line), 100 nm (dark purple line) and 1000 nm (pink line). The impedance mismatch of the overcoupled cavity decreases with increasing absorption losses due to the increasing membrane thickness.

length is required. The shorter the substrate length the more heating is necessary. Since `tksim` requires small temperature changes in the regime where the material parameters change linearly with temperature, for very thin substrates thermal measurements are not realizable for very thin substrates. Therefore, the absorption of the membranes was measured via cavity round-trip losses. Figure 7.4 shows the mean value of the simulated resonance peaks for the cavity without membrane (orange line) and the cavity with membranes 50 nm no2, 100 nm no3 and 1000 nm no2. The impedance mismatch decreases with increasing membrane thickness.

Table 7.1: Slope coefficient a from Eq. (7.1) fitted to the measurement data shown in Fig. 7.3 for each membrane and wavelength.

membrane	a_{1064} [K/W]	a'_{1550} [K/W]
50 nm no2	-	0.005624
100 nm no1	0.346 $\leftarrow \times 11.0$	0.031376
1000 nm no2	-	1.12924
1000 nm no3	5.204 $\leftarrow \times 9.7$	0.539016

$\left. \begin{matrix} 1.12924 \\ 0.539016 \end{matrix} \right\} \times 17.4$

Table 7.2: Parameters and results for the wavelength dependent absorption measured with the IR camera. The absorption is given per 1000 nm membrane. Due to Brewster's angle the beam covers a distance of 1103 nm within the membrane.

wavelength	$\frac{A_x}{A_{1550}}$	a [K/W]	α [ppm/1103 nm]
285 nm	7.1 ± 2.0	857	$(2.3 \pm 1.0) \times 10^6$
532 nm	0.87 ± 0.18	600.9*	$(1.9 \pm 0.5) \times 10^5$
1064 nm	0.68	5.2	$(1.3 \pm 0.1) \times 10^3$
1550 nm	1	0.36	137 ± 14
2 μm	0.59 ± 0.12	2.7	605 ± 199

* This measurement was performed with membrane 100 nm no3. The results are multiplied with a factor of 17.4, since for the other measurements membrane 1000 nm no3 was used.

7.2.1 Experimental Setup

For the measurement a Fabry-Perot cavity was used. Figure 7.5 shows a schematic of the experimental setup. The cavity was formed by in-coupling mirror M_1 with design reflectivity $R_1 = 99\%$ and the high reflective (HR) coated end-mirror M_2 , which were fixed to an aluminium spacer. The mirror distance was 158 mm. The membrane was positioned at Brewster's angle within the cavity. The cavity length was scanned via a piezo-electric transducer (PZT), which was fixed between end-mirror and spacer. A polarizing beam splitter (PBS) and a Faraday rotator (FR) separated the reflected light field P_{refl} from the incoming light field P_{in} to measure the reflected resonance peaks of the cavity with a photo diode. The $\lambda/2$ -waveplate was used to match the polarization to Brewster's angle. The electro-optical modulator (EOM) imprinted sidebands onto the light field to calibrate the motion of the mirror (see Subsec. 7.2.3).

The setup for the 1550 nm measurements was very similar to the setup used at 1064 nm shown in Fig. 7.5. The mirror distance was slightly longer with $L = 163$ mm. The mirrors had a design reflectivity of $R_1 = 99.4\%$ on the input mirror M_1 and a HR coating on end-mirror M_2 .

The cavity round-trip losses caused by the membrane were measured in two steps. First, resonance peaks of the cavity without membrane were detected. From these measurements, the reflectivity R_1 of M_1 as well as the effective out-coupling reflectivity \tilde{R}_2 were obtained, where \tilde{R}_2 contains the absorption and scattering losses of the two mirrors. Due to the differing mirror reflectivities, the cavity is strongly impedance mismatched and only small resonance peaks become visible (see Fig. 7.6, orange line). In the second step, a membrane was placed within the waist of the cavity at Brewster's angle. The membrane caused additional losses, which decreased the reflectivity \tilde{R}_2 and therefore the impedance mismatch (see Fig. 7.4). Detecting and fitting these peaks via `tksim` delivered a change of \tilde{R}_2 (while R_1 stayed constant) and therefore the losses

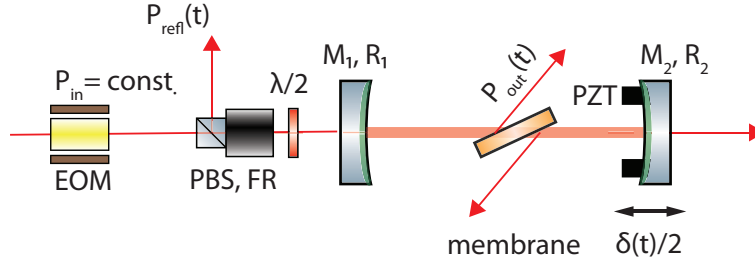


Figure 7.5: The laser power P_{in} was transmitted by a polarizing beam splitter cube (PBS), a Faraday rotator (FR) and a $\lambda/2$ -waveplate before coupling into the cavity through input mirror M_1 . The mirrors M_1 and M_2 formed the cavity. The membrane was positioned in the beam waist in the middle of the cavity. To minimize losses due to reflected light the membrane was arranged at Brewster's angle. A piezo electric transducer (PZT) was used to modulate the cavity length.

caused by the membrane. These losses contain surface scattering of the membrane and reflection losses caused by a non-perfect alignment to the Brewster's angle. Due to a Brewster's angle of $\arctan(n = 2.2) = 65^\circ$ the membrane could not be placed within a node or anti-node of the standing-wave light field, but saw an integration over many nodes and anti-nodes. Therefore, the absorption measured in this experiment is expected to correspond to the red line in Fig. 7.1, which is the absorption neglecting geometric effects. The Brewster's angle was optimized by rotating both the waveplate and the membrane, minimizing the round-trip losses. The remaining power P_{out} reflected at the membrane surface at resonance was measured with a calibrated photo diode.

Between 10 and 14 single measurements varying the modulation frequency were performed for each of six membranes: 50 nm no1 & no2, 100 nm no1 & no2 and 1000 nm no2 & no3. (Note, due to Brewster's angle the path through the membrane is about 10% longer than the path under normal incidence. Here, always the membrane thickness is given, not the propagation length of the beam through the membrane.)

7.2.2 Experimental Results

The plots in Fig. 7.6 shows a measured (dots) and simulated (lines) resonance peak in reflection for scan frequencies of 1 kHz (left) and 150 Hz (right) of the cavity at 1064 nm without membrane. Since no absorption occurs, the peaks are identical (apart from statistical fluctuations) for the two scan directions. The left peaks with fast scan frequency show ringing while the peaks with slow scan frequency show a conventional shape. From 14 single measurements the input reflectivity and the effective output reflectivity were fitted. The results from 14 single measurements obtained with scan frequencies between 100 Hz and 1 kHz were $R_1 = (98.916 \pm 0.015) \%$ and $\tilde{R}_2 = (99.9951 \pm 0.0003) \%$ ($1 - \tilde{R}_2 = (49 \pm 3) \text{ ppm}$) which corresponds to a finesse of $F = 574 \pm 8$.

At 1550 nm the loss of the empty cavity was measured from 10 single measurements.

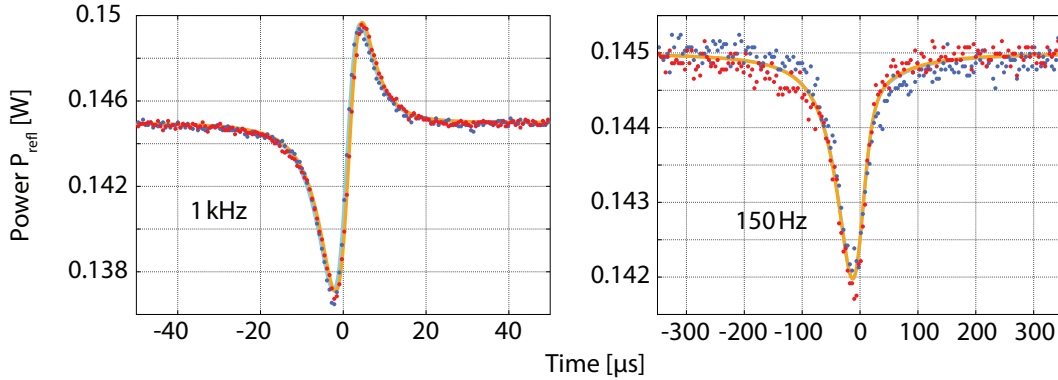


Figure 7.6: Reflected resonance peaks for the 1064 nm cavity without membrane. Since no absorption occurs, the peaks are identical for the two scan directions. The measured peaks are represented by the dots, the simulation by the lines. The left peaks showing a ringing effect are for a fast scan frequency of 1 kHz, the right peaks for a frequency of 150 Hz.

The results were $R_1 = (99.428 \pm 0.013)\%$ and $\tilde{R}_2 = (99.9900 \pm 0.0004)\%$ ($1 - \tilde{R}_2 = (100 \pm 4)$ ppm). The finesse of the cavity without membrane was determined to be $F = 1078 \pm 24$.

The procedure was repeated for different membranes placed in the cavities. For each membrane, R_1 and \tilde{R}_2 were fitted. The remaining power reflected at the membrane surface at resonance P_{out} is given in Tab. 7.3 in ppm of the round-trip power P . The single pass absorption of a membrane at Brewster's angle is then given by

$$\alpha = \frac{\tilde{R}_2 - \tilde{R}_{2\text{mem}}}{2} - \frac{P_{\text{out}}}{P}. \quad (7.3)$$

R_1 and $1 - \tilde{R}_2$ with the standard deviation from all single results are given in Tab. 7.3 for 1064 nm and at 1550 nm. (Note that for the measurements with different wavelengths, the used membranes with same thickness and numbers were identical. Unfortunately, not all membranes could be measured at the two wavelengths, since some of the very fragile membranes were destroyed during the measurements.)

7.2.3 Error Propagation

The standard deviation of the results is very small and therefore uncertainties of the input parameters are assumed to dominate the error of the results.

For a loss measurement the simulation input parameters for `tksim` reduce to the mode matching factor mm and the parameters which are relevant for the time axis calibration. For the time-axis calibration these are the scan frequency f , the side-band frequency, the NFSRs and the cavity length L . In the membrane setups L is simply the mirror distance since the optical length increase due to the thin membrane is negligible.

7.2 Absorption Measurements at 1064 nm and 1550 nm

Table 7.3: Results for R_1 and $(1 - \tilde{R}_2)$ of the measurements for different membranes and without membrane at 1064 nm and 1550 nm. The number of single measurements varying per series is given as well as the power P_{out} reflected at the membrane surface due to non perfect Brewster's angle.

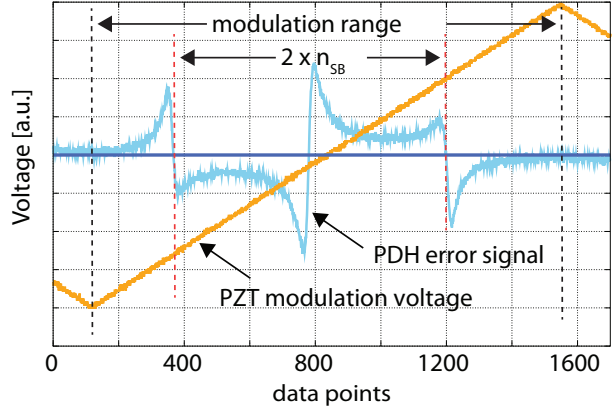
Membrane	No. of meas.	R_1 [%]	P_{out}/P [ppm]	$(1 - \tilde{R}_2)$ [ppm]	α
1064 nm					
-	14	98.916 ± 0.015	-	49 ± 3	-
50 nm no1	13	98.922 ± 0.010	$< 1^*$	100 ± 4	26 ± 4
50 nm no2	13	98.941 ± 0.014	1	123 ± 4	36 ± 4
100 nm no1	10	98.896 ± 0.028	5	234 ± 10	88 ± 7
100 nm no3	12	98.920 ± 0.017	1	486 ± 8	218 ± 6
1000 nm no2	12	98.928 ± 0.012	4	3155 ± 35	1579 ± 19
1550 nm					
-	10	99.428 ± 0.013	-	100 ± 4	-
50 nm no1	10	99.411 ± 0.009	1	121 ± 3	10 ± 4
50 nm no2	9	99.410 ± 0.027	1	243 ± 14	71 ± 9
100 nm no1	10	99.421 ± 0.035	2	138 ± 6	17 ± 5
100 nm no2	9	99.416 ± 0.009	1	128 ± 2	13 ± 3
1000 nm no2	10	99.410 ± 0.013	5	2115 ± 41	1003 ± 23
1000 nm no3	10	99.422 ± 0.007	3	380 ± 5	137 ± 5

*not measureable, since too small

For the mode matching measurement an error of more than 1% is unlikely. The length L of the cavity can be determined better than ± 1 mm which corresponds to less than 1%. The scan frequency and side-band frequency were generated by a function generator and were known very accurate. This leaves the NFSRs as potentially critical parameters. The effect of an input error of 1% on the results for R_1 and \tilde{R}_2 for each of the three parameters mm , L and $\text{NFSR}_i/\text{NFSR}_d$ is given in Tab. 7.4 for both setups.

Fig. 7.7 shows a measurement of NFSR_i from the 1064 nm setup. The modulation voltage, which follows a ramp function, is shown by the yellow line. The number of data points of the increasing ramp side was measured (distance of the black dashed lines) and divided by the distance of the side bands, which are the zero-crossings of the light blue PDH error signal and marked by the red dashed lines. This ratio of about two for this example, calibrated with two times the side band frequency divided by the frequency of 1 FSR, yields NFSR, the number of FSRs scanned per ramp side. For the measurements at 1064 nm about 7–8% of an FSR were scanned per ramp side, for 1550 nm about 4%. The value slightly increased with scan frequency. This measurement itself is very accurate and the separate measurement for each ramp side and scan frequency reduces the error of the time axis calibration strongly. The remaining error source is the part of

Figure 7.7: Measurement of NFSR: The yellow curve shows the PZT modulation voltage (= ramp signal), the light blue curve shows a PDH error signal. The ratio of one ramp side (distance of black dashed lines) and PDH zero-crossing distance (red dashed lines) in data points multiplied with $(2 \times \nu_{SB})/\Delta\nu_{FSR}$ gives NFSR.



the ramp outside the sidebands. This error is assumed to be about 5%, which results in error bars of 10% for the round trip loss measurements.

An additional error source of the loss measurements is that it cannot be ensured that the membrane is passed in center. If the silicon frame of a membrane is covered by a part of the beam, the much thicker frame (200 μm) can cause additional absorption and the edge between membrane and frame causes scattering loss. Further, the membranes can be contaminated for example by dust when brought from one cavity to the other. The size of these errors cannot be quantified.

7.3 Calibration of the Temperature Measurements

In Sec. 7.1 temperature measurements with the IR camera for different wavelengths were presented. For the measurements 285 nm, 1064 nm, 1550 nm and 2 μm membrane 1000 nm no3 was used. On this membrane an absorption of (137 ± 14) ppm was measured at 1550 nm (see Sec. 7.2). Using this absorption value and the intensity normalized slope factor $a \times \frac{A_x}{A_{1550}}$ from Tab. 7.2 the absorption for the other wavelengths was calculated.

Table 7.4: Effect on R_1 and \tilde{R}_2 for 1% change of the simulation input parameters mm , L and $\text{NFSR}_i/\text{NFSR}_d$.

	mm	L	$\text{NFSR}_i/\text{NFSR}_d$
1064 nm			
R_1	0.01 %	0.005 %	0.005 %
\tilde{R}_2	1 ppm	< 1 ppm	1 ppm
1550 nm			
R_1	50 ppm	50 ppm	80 ppm
\tilde{R}_2	1 ppm	1 ppm	2 ppm

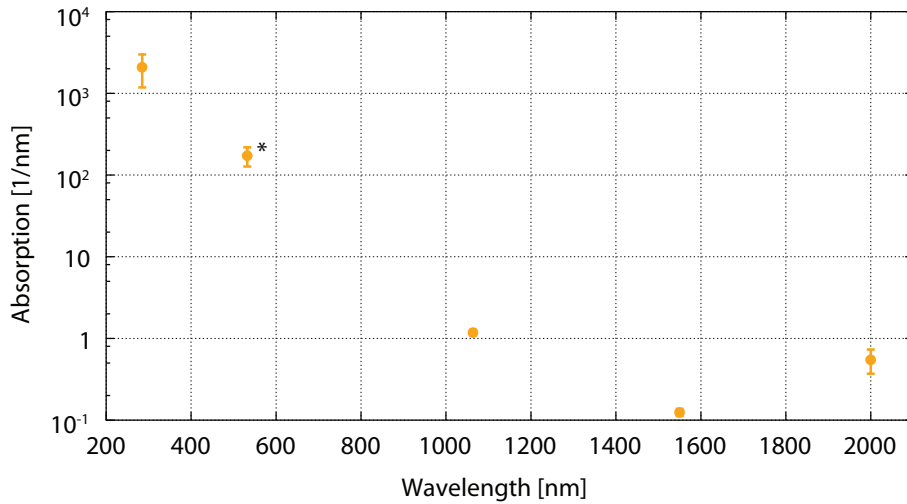


Figure 7.8: Membrane absorption with wavelength: The orange dots show the absorption α given in Tab. 7.2 depending on the wavelength. (*This measurement was performed with membrane 100 nm no3 while for the other measurements membrane 1000 nm no3 was used.)

The results are given in Tab. 7.2 and are illustrated in Fig. 7.8.

For the temperature measurements at 532 nm membrane 100 nm no3 was used. For this membrane the slope factor was additionally multiplied by a factor of 17.4, which was found for the temperature ratio of a 100 nm and a 1000 nm membrane (see Tab. 7.1). The result is also given in Tab. 7.2.

7.4 Final Results and Conclusion

The results for the absorption at 1064 nm given in Tab. 7.3 are shown in Fig. 7.1 (green dots). The measurement for the 1000 nm membrane is in good accordance with the theory (red line). The other results are below the theory curve, but confirm the increasing trend of the curve. An increase of the absorption due to the membrane's thickness can be confirmed, while the expected linear correlation is not represented in the results.

With an IR camera the temperature on the surface of a membrane at different wavelengths could be calibrated and a minimum absorption at 1550 nm was found (see Fig. 7.8).

The measurements with the IR camera as well as the cavity loss measurements showed that the absorption of SiN membranes decreased by a factor of approximately 10, when the wavelength is changed from 1064 nm to 1550 nm.

Cryogenic opto-mechanical experiments are limited by the temperature increase due to absorption at very low temperature. An absorption decrease by a factor of 10 increases

7 Optical Absorption Measurements on Thin SiN Membranes

the sensitivity of such experiments by a factor of 2 regarding the change to the higher wavelength.

For these experiments, the absolute temperature of the membranes is also of interest. However, the measurements presented in this chapter were performed in air while the cryogenic experiments work in vacuum. Thus, the temperatures measured here are not transferable since convection cannot be neglected. Therefore, temperature measurements in vacuum are planned.

- 7.1 S. Hild, S. Chelkowski, A. Freise, J. Franc, N. Morgado, R. Flaminio, R. DeSalvo
A xylophone configuration for a third-generation gravitational wave detector
Class. Quantum Grav. **27** 015003, 2010
- 7.2 T. P. Purdy, R. W. Peterson, C. A. Regal
Observation of Radiation Pressure Shot Noise
arXiv:1209.6334v1, 2012
- 7.3 K. Borkje, A. Nunnenkamp, B. M. Zwickl, C. Yang, J. G. E. Harris, and S. M. Girvin
Observability of radiation–pressure shot noise in optomechanical systems
Phys. Rev. A **82** 013818, 2010
- 7.4 P. Verlot, A. Tavernarakis, T. Briant, P.-F. Cohadon, A. Heidmann
Scheme to probe optomechanical correlations between two optical beams down to the quantum level
Phys. Rev. Lett. **102** 103601, 2009.
- 7.5 D. Friedrich, H. Kaufer, T. Westphal, K. Yamamoto, A. Sawadsky, F. Khalili, S. L. Danilishin, S. Goßler, K. Danzmann, R. Schnabel
Laser interferometry with translucent and absorbing mechanical oscillators
New Journal of Physics **13** 093017, 2011
- 7.6 DIAS Infrared GmbH, Dresden, Germany
www.dias-infrared.de
- 7.7 Norcada Inc., Canada
www.norcada.com

Absorption Measurements on High Reflective Coatings at 1550 nm

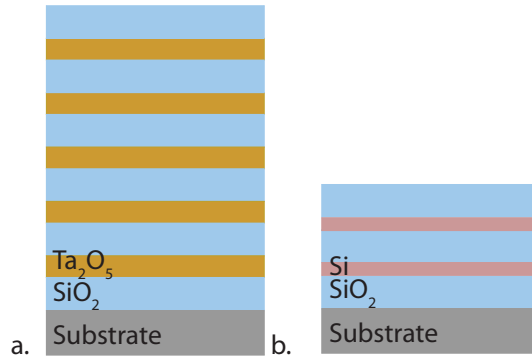
Highly reflective dielectric mirror coatings are essential for interferometric GWDs. Optical coatings with very accurately specified transmission as well as low optical absorption and mechanical loss are required [8.1]. It is assumed that thermal noise due to mechanical loss might be a significant thermal noise source in future GWDs [8.2].

The first and second generations of GWDs operate at a laser wavelength of 1064 nm. Dielectric optical coatings made of alternating layers of fused silica (SiO_2) and tantala (Ta_2O_5) are used in the detectors up to now. The coating absorption requirements for LIGO were ≤ 1 ppm [8.3], for Advanced LIGO they are already 0.5 ppm [8.1, 8.4] for high reflective coatings with only 5 ppm transmission [8.4]. While coatings with the specified absorption requirements were already produced [8.1], the mechanical loss is still above the requirements of $\phi = 5 \times 10^{-5}$ [8.4], with tantala being the material with higher losses [8.2]. Doping the tantala with titanium can reduce the loss by nearly a factor of two, but also slightly increases the coating absorption [8.1]. Further, tantala shows a loss peak at low temperatures [8.5], where GWDs of the third generation are planned to operate [8.6]. Therefore various materials are under investigation to replace the tantala within coatings.

Amongst the considered materials is silicon. Bulk crystalline silicon has a high mechanical quality factor (Q-factor) at room temperature that even increases towards cryogenic temperatures [8.7, 8.8] and makes silicon interesting for a test-mass material [8.10]. Silicon shows a high optical absorption at the currently used wavelength of 1064 nm, that decreases rapidly towards higher wavelength and is assumed to be very low around 1550 nm [8.9]. Therefore silicon is considered for a test-mass material for future GWDs operating at cryogenic temperatures and a wavelength of 1550 nm [8.6] and thus silicon also comes into play for coatings.

Dielectric high reflective coatings are based on alternating layers of a low refractive

Figure 8.1: a. shows a coating stack of 11 single $\lambda/4$ layers. Fused silica (SiO_2) and tantala (Ta_2O_5) layers are alternating. The reflectivity results in $\approx 96\%$. Replacing the tantala with index of refraction $n_{\text{Ta}} = 2.2$ by silicon with index of refraction $n_{\text{Si}} = 3.48$, reduces the number of layers necessary for $\approx 96\%$ reflectivity to only 5. Since the optical thickness of the single layers has to be constant, the higher index of refraction additionally reduces the absolute thickness of the coating (b.).



index (n_1) and a high refractive index (n_2) material. The intensity reflection results from the Fresnel equations, which for the simple case of an angle of incidence of 0° and negligible absorption read

$$R_s = R_p = \left(\frac{n_1 - n_2}{n_1 + n_2} \right)^2. \quad (8.1)$$

The minimum of this function (no reflection) occurs at $n_1 = n_2$, while the reflection increases with increasing n_2 for $n_2 < n_1$. Silicon has a very high index of refraction of $n_{\text{Si}} = 3.48$ [8.11] compared to tantala with $n_{\text{Ta}} = 2.2$ [8.13]. The low index material fused silica has an index of refraction of $n_{\text{FS}} = 1.45$ [8.12] at 1550 nm. Due to the higher index of refraction of silicon much less single layers are required in a Si/ SiO_2 coating stack compared to $\text{Ta}_2\text{O}_5/\text{SiO}_2$. Calculations with a coating design tool [8.14] showed that changing the index of refraction of the high refractive material from 2.2 (fig. 8.1 a.) to 3.5 (Fig. 8.1 b.) reduces the number of necessary single layers to achieve a reflectivity of $\approx 96\%$ from 11 to only 5. The higher index of refraction additionally reduces the absolute thickness of the coating (Fig. 8.1 b.), since the single layers have a constant optical thickness of a quarter of the wavelength.

In parallel, the absorption behavior of the commonly used $\text{Ta}_2\text{O}_5/\text{SiO}_2$ coatings at the new wavelength of 1550 nm is of interest. In the following two experiments are presented, the first one measuring the absorption of $\text{Ta}_2\text{O}_5/\text{SiO}_2$ coatings, the second one measuring the absorption of Si/ SiO_2 coatings – both at 1550 nm.

8.1 Absorption Measurements on a $\text{Ta}_2\text{O}_5/\text{SiO}_2$ Coating at 1550 nm

For the absorption measurement on $\text{Ta}_2\text{O}_5/\text{SiO}_2$ at 1550 nm a Fabry-Pérot cavity was used. The two cavity mirror substrates consist of Corning 7980 glass [8.15]. The coatings were manufactured at *Advanced Thin Films* (ATF) [8.17] and optimized for a finesse of 10000 under an angle of incidence (AOI) of 0° at 1550 nm. A finesse of 10000 theoretically is reached by two identical lossless mirrors with intensity reflectivities of

8.1 Absorption Measurements on a Ta_2O_5/SiO_2 Coating at 1550 nm

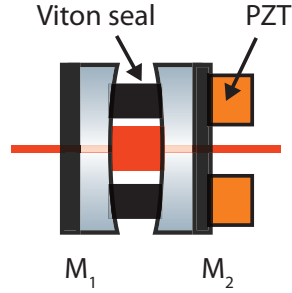


Figure 8.2: Schematic of the short Fabry-Pérot cavity used for the absorption measurements on the Ta_2O_5/SiO_2 coating: A compressible viton seal (black) separates the two identical mirrors M_1 and M_2 . A PZT (orange) actuated by a function generator modulates the mirror distance by pressing M_2 into the viton seal.

$R_1=R_2=99.969\%$ ($1-R=310$ ppm). The transmission measured by the manufacturer on a mirror from this coating run was $T=320$ ppm.

8.1.1 Experimental Setup

Figure 8.2 shows a schematic of the Fabry-Pérot cavity setup. Two identical curved mirrors M_1 and M_2 are clamped together facing each other, separated only by a 0.75 mm viton seal. A PZT, driven by a function generator (FG), presses M_2 into the viton seal and therefore changes the cavity length.

Both mirrors are convex curved with a radius of curvature (ROC) of 0.5 m resulting in a cavity waist of $82\ \mu\text{m}$. The mode matching factor was only 78% for this setup, since the very short cavity is very sensitive to the mode matching lenses positions. The short cavity length results in a large free spectral range (FSR) of 200 GHz. Assuming a finesse of approximately 10000 the cavity line width $\nu_{\text{LW}} = \nu_{\text{FSR}}/F$ was expected to be in the order of 20 MHz. The material properties and cavity geometry parameters of this setup are summarized in Tab. 8.1. The mirror substrate material and therefore the wavelength independent material properties are identical to the experiment described in Section 4.2.

To linearize the mirror motion, the cavity length was modulated only in a small range around the resonance of approximately 0.3% of an FSR slightly varying with the modulation frequency (the modulation voltage was constant for all measurements). The actual mirror motion for each modulation frequency and ramp side (expansion or contraction of the PZT) was calibrated using side bands imprinted on the laser signal via an electro optical modulator (EOM) before entering the cavity (see Sec. 7.2.3). The resonance peaks for the absorption measurement were detected with a photo detector (PD) in reflection of input mirror M_1 . The reflected beam was separated from the incoming beam at a polarizing beam splitter cube (PBS) using a $\lambda/2$ waveplate and a Faraday rotator.

8.1.2 Results and Error Propagation

To measure the absorption several single measurements of reflected resonance peaks were detected, partly showing a thermal effect caused by absorption, partly showing no

Table 8.1: Material and geometric parameters of the Corning 7980 mirror substrates and the cavity, as used for the simulations. Wavelength and temperature dependent parameters are given at 1550 nm and room temperature.

Material parameters		Reference
index of refraction n	1.44	[8.12]
thermal refr. coeff. dn/dT	$9.6 \cdot 10^{-6} / \text{K}$	[8.15]
specific heat c	770 J/(kg K)	[8.16]
density ρ	2201 kg/m ³	[8.15]
thermal expansion a_{th}	$0.52 \cdot 10^{-6} / \text{K}$	[8.15]
thermal conductivity k_{th}	1.3 W/(m K)	[8.15]
material emissivity ϵ	1.0	
Cavity geometry parameters		
input power P	2 mW, 130 mW, 260 mW	
round-trip length L	0.75 mm	
beam waist ω_0	82 μm	
mirror length D	6.35 mm	
mirror radius r	12 mm	
mode matching (MM)	78 %	
angle of incidence (AOI)	0°	

thermal effect. The measured peaks were fitted using the simulation program `tksim` (see chapter 3) and a Nelder-Mead fitting algorithm with the input parameters shown in table 8.1 and table 4.3.

Altogether 34 single measurements were performed: 12 measurements with an input power of 2 mW and scan frequencies between 160 Hz and 1000 Hz showing no thermal effect, 10 measurements with an input power of 130 mW and scan frequencies between 10 Hz and 100 Hz all showing a thermal effect. From the 12 measurements with an input power of 260 mW and scan frequencies between 160 Hz and 1000 Hz 11 are showing a thermal effect. The results for the measurements without visible thermal effect are the input reflectivity R_1 and the effective reflectivity of the end mirror \tilde{R}_2 containing the output transmission and all round-trip losses, which are the absorption and scattering of both mirror coatings. Additionally, for the measurements with visible thermal effect the absorption α of the input mirror results.

Figure 8.3 shows two examples of measured and simulated reflected resonance peaks. In Fig. 8.3 a., a measurement at an input power of 2 mW and a scan frequency of 600 Hz resulting in no thermal effect is shown. The resonance peaks in Fig. 8.3 b. show a clear thermal effect detected at an input power of 260 mW and a scan frequency of 160 Hz.

The results for R_1 and \tilde{R}_2 of all measurements are shown in Fig. 8.4 a. For a better readability $1 - R$ is given on the y-axis instead of R . The light-blue dots show $1 - R_1$ and

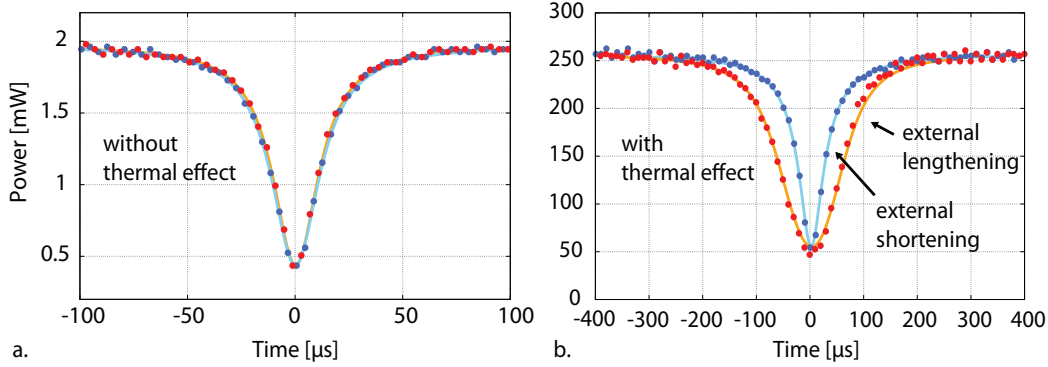


Figure 8.3: Two examples of measured and simulated reflected resonance peaks: a. shows a measurement at an input power of 2 mW and a scan frequency of 600 Hz resulting in no thermal effect. The resonance peaks in b. show a clear thermal effect detected at an input power of 260 mW and a scan frequency of 160 Hz.

the orange triangles $1 - \tilde{R}_2$. The blue line gives the mean value of all results for R_1 , with the dashed blue lines marking the standard deviation of all results. Correspondingly the red lines mark the mean value and standard deviation of $1 - \tilde{R}_2$. The results are $1 - R_1 = (253.73 \pm 16.4)$ ppm and $1 - \tilde{R}_2 = (276.3 \pm 13.3)$ ppm. (In Fig. 8.4 a. the result of one measurement which deviates strongly is left out for a better resolution of the remaining results. This result is included in the calculated mean values and standard deviations.) These values for the mirror reflectivities result in a cavity finesse of $F = (11853 \pm 704)$.

From altogether 21 measurements the absorption could be obtained. The results of the single measurements are shown in Fig. 8.4 b., the light green bar marking the mean value of the 21 single results, the dashed light green bars their standard deviation. The resulting absorption for the input mirror coating is $\alpha = (1.7 \pm 0.3)$ ppm ($0.3 \text{ ppm} \hat{=} 17.6 \%$).

For a detailed discussion of the possible error caused by the input parameters see Subsec. 4.2.3, where the expectable error due to inaccurate material properties is analyzed. Since the material properties are identical or at least very similar to the parameters discussed in Subsec. 4.2.3 their influence on the result also has to be very similar. The mirror dimensions are also identical to the experiment in Subsec. 4.2.3, input power and mode matching always influence the result approximately linear. The only parameters which differ strongly from the other experiment are the cavity length and the beam waist. These two parameters were changed each by $\pm 10 \%$ and the results of one single measurement were recalculated. An error of $\pm 10 \%$ in the cavity length influences the result by approximately $\pm 10 \%$, where a cavity length assumed too long reduces the necessary absorption for the present thermal effect and inverse for a cavity length assumed too short. An error in the cavity length also affects the waist. An error of $\pm 10 \%$ in the length only affects the waist by approximately $\pm 3 \%$, which causes an error of $\pm 6 \%$ in the absorption result. The large error of about 10 % for such a short cavity is realistic.

Since cavity length and waist depend on each other as discussed, both errors add. The summed up error is still within the standard deviation for the absorption result.

Therefore for the results obtained from this series of measurements the standard deviation caused by statistical fluctuations of the detected resonance peaks is assumed to dominate the error caused by inaccurate input parameters.

8.1.3 Discussion

The results for the reflectivities are $1 - R_1 = (253.73 \pm 16.4)$ ppm and $1 - \tilde{R}_2 = (276.3 \pm 13.3)$ ppm. The cavity finesse is $F = (11853 \pm 704)$. This is better than the design value of $F = 10000$, but in the expected order of magnitude. The reflectivity R_1 is slightly better than expected from the transmission measured by the manufacturer which was $T_1 = 320$ ppm. For the coating reflectivities no tolerance was specified – neither in the order nor by the manufacturer. Assuming identical reflectivities for both mirrors $R_1 - \tilde{R}_2 = 22.6$ ppm is the round-trip loss of the cavity.

The result for the coating absorption was $\alpha = (1.7 \pm 0.3)$ ppm. The absorption requirements for GWDs are below these results as discussed in the introduction of this chapter. However, it has to be considered that the 1550 nm coatings were no specified low loss or low absorption coatings. Prior absorption measurements on ATF low loss coatings at a wavelength of 850 nm showed absorptions of 0.55 ppm per coating (1.1 ppm per two coatings) [8.18]. The absorption measurements presented in this chapter show results very close to the previous reported value and are in the expected order for high quality IBS coatings. Therefore it can be assumed that the absorption characteristic of Ta₂O₅/SiO₂ at 1550 nm is comparable to good 1064 nm coatings and changing the wavelength to 1550 nm causes no absorption problems with the commonly used Ta₂O₅/SiO₂.

8.2 Absorption Measurements on a Si/SiO₂ Coating at 1550 nm

The absorption measurements on Si/SiO₂ coatings at 1550 nm were performed using a three-mirror ring-cavity setup similar to the setup used in Sec. 4.2. The three mirror substrates consist of Corning 7980 glass [8.15] identical to the substrates used in the experiment in the first part of this chapter. The coatings were manufactured at Tafelmaier [8.19] using the Ion Plating procedure and optimized for a reflectivity of $R = (99.95 + 0.01 / - 0.03)$ % under an angle of incidence (AOI) of 44° at 1550 nm and s-polarization.

8.2.1 Experimental Setup

The three mirrors building the cavity were glued to an aluminium spacer. Between one mirror and the spacer a PZT was fixed to modulate the cavity round-trip length. For a schematic of the experimental setup see Fig. 4.7 in Chapter 4. The cavity geometry

8.2 Absorption Measurements on a Si/SiO₂ Coating at 1550 nm

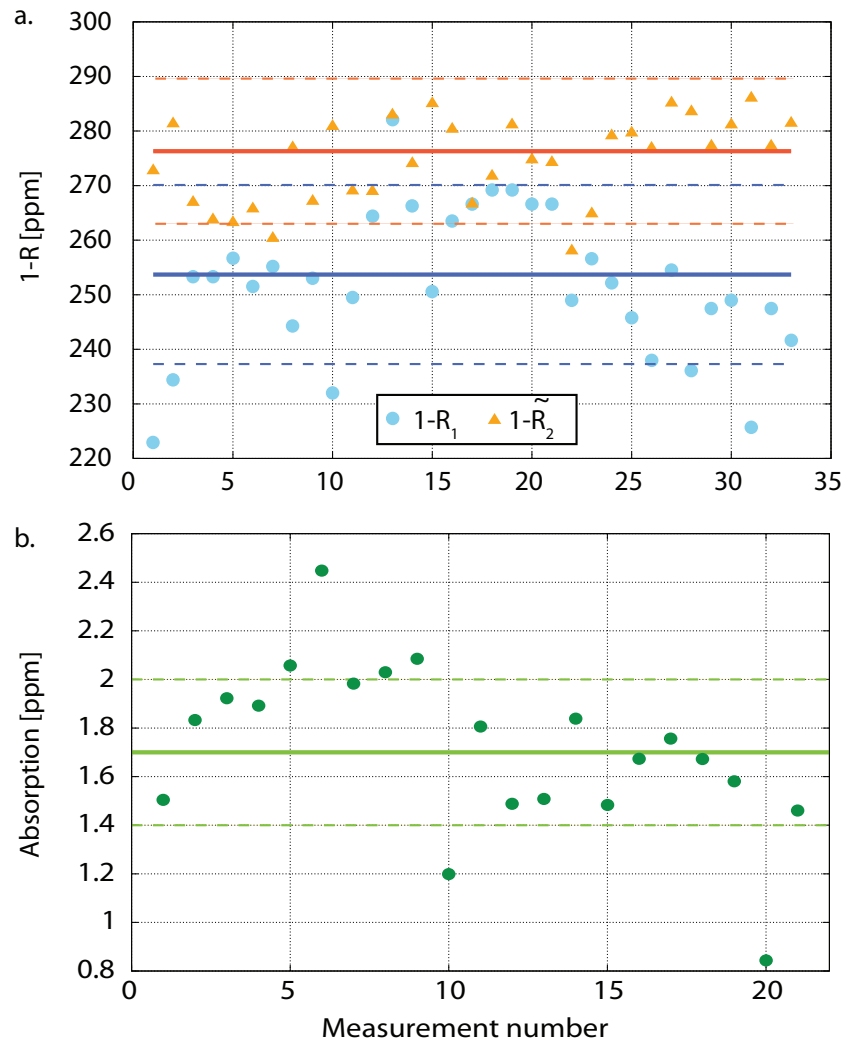


Figure 8.4: Measurement results for tantala HR-coatings at 1550 nm: In a. the results of the single measurements for $1 - R_1$ and $1 - \tilde{R}_2$ are shown. $1 - R_1$ is given by the blue dots. The dark blue line marks the mean value and the dashed line the standard deviation of $1 - R_1 = (253.7 \pm 16.4)$ ppm. $1 - \tilde{R}_2$ is shown by the orange triangles, the red line marks the mean value and the dashed red lines the standard deviation of $1 - \tilde{R}_2 = (276.3 \pm 13.3)$ ppm. b. shows the results for the absorption of the single measurements (dark-green dots). The light-green line and dashed lines mark the mean value and standard deviation of $\alpha = (1.7 \pm 0.3)$ ppm.

parameters are identical to the parameters presented in Tab. 4.3, only the beam waist differs due to the change of the wavelength. The waist in this setup was $448 \mu\text{m}$. Since the mirror substrate material is identical to the substrates used in Sec. 4.2 and Sec. 8.1, the material properties can be found in Tab. 8.1 where the wavelengths is the same as in the experiment presented here. All single measurements were performed in s-polarization.

The calibration of the time axis (mirror motion) was also identical to the procedure used for the 1064 nm experiment, the sideband frequency being larger so that approximately 10 % of an FSR were scanned per ramp side. In this experiment again the reflectivities R_1 and \tilde{R}_2 as well as α for measurements with significant thermal effect were treated as free parameters of the simulation. The three parameters were fitted to the single measurements using a Nelder-Mead algorithm (see Subsec. 4.2.2).

8.2.2 Experimental Results and Error Propagation

To obtain results for the three parameters R_1 , \tilde{R}_2 and α , 30 single measurement were taken. 11 measurements showed a significant thermal effect. For the different measurements the input power of 367 mW was constant, while the scan frequency was varied between 500 Hz and 5 Hz. At high scan frequencies no thermal effect is visible. Fig. 8.5 a. shows resonance peaks (external lengthening: red dots – measurement, orange line – simulation; external shortening: blue dots – measurement, light-blue line – simulation) detected at scan frequency of 90 Hz, where the two peaks for an external lengthening and shortening of the cavity are identical. At 19 Hz (Fig. 8.5 b.) a weak thermal effect is visible, which becomes more distinct at 13 Hz (Fig. 8.5 c.). At about 15 Hz was the limit at which the thermal effect was sufficient for fitting α . At faster scan-frequencies the results were very inaccurate. The resonance peaks detected at 5 Hz (Fig. 8.5 d.) were the lower limit for the scan frequency. In this measurements the thermal effect is strongly developed. For scan frequencies even slower the temperature within the mirror substrates around resonance becomes too large for the broad peak and material parameters do not change linear with temperature any more. While the small peak still can be fitted for 1 Hz scan frequency, the broad peak's appearance completely differs from the other peaks and can not be reproduced by the simulation (Fig. 8.5 e.).

The mean value and standard deviation of the results from the single measurements are $1 - R_1 = (529 \pm 20)$ ppm, $1 - \tilde{R}_2 = (2902 \pm 103)$ ppm and $\alpha = (1035 \pm 42)$ ppm. A graphical overview of the single results for all three quantities is shown in Fig. 8.6. In Fig. 8.6 a. the results of the single measurements for $1 - R_1$ are shown with the light-blue dots. The mean value of all single results is marked by the blue line, and the standard deviation by the dashed blue lines. The result of $1 - R_1 = (529 \pm 20)$ ppm is in excellent agreement with the specification of $R = (99.95 + 0.01 / - 0.03)$ %. Figure 8.6 b. shows the results of the single measurements for $1 - \tilde{R}_2$ in dark-green dots. Mean value and standard deviation are marked by the light-green line and dashed lines. The single results for the absorption of the input mirror coating are shown in Fig. 8.6 c. by the pink dots. Mean value and standard deviation are marked by the purple line and

8.2 Absorption Measurements on a Si/SiO₂ Coating at 1550 nm

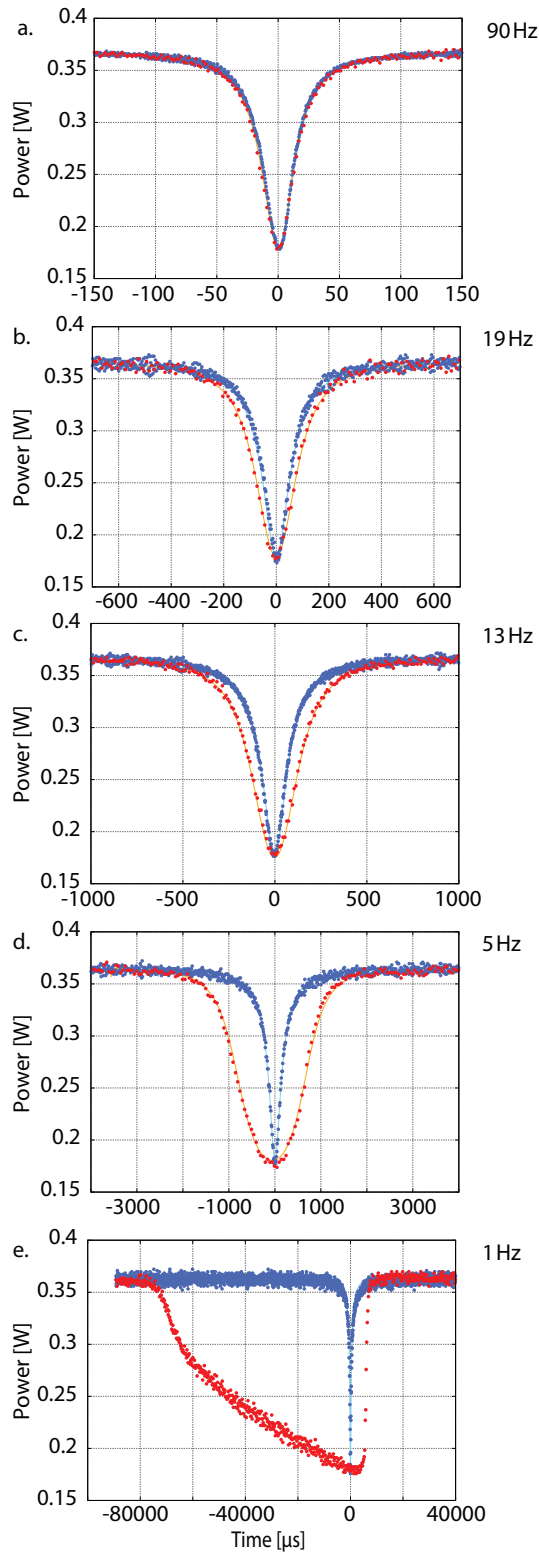


Figure 8.5: Reflected resonance peaks for different scan-frequencies at constant scan-amplitude and input power. For all five figures the dots show the measured peaks and the lines show the corresponding simulations. For an external lengthening of the cavity the broad peaks (red dots: measurement, orange line: simulation) form, for an external shortening the narrow peaks (dark-blue dots: measurement, light-blue line: simulation) form. Fig. a. shows resonance peaks at a scan-frequency of 90 Hz. At this scan-frequency no thermal effect is visible and the peaks are identical for both scan directions. Fig. b. shows resonance peaks at a scan-frequency of 19 Hz. A slight thermal effect is visible. In Fig. c. the scan frequency is reduced to 13 Hz and the thermal effect becomes more significant. Fig. d. shows resonance peaks at a scan frequency of 5 Hz which was the lower limit for the peaks to be reproducible by the simulation. Fig. e. shows resonance peaks for a scan-frequency of 1 Hz. While the narrow peak can still be simulated, the broad red peak has significantly changed its shape and can not be reproduced by the simulation.

dashed purple lines.

The standard deviation of each result is approximately 4%. This is a small standard deviation compared to the other absorption measurements presented in this work. Reasons for the small standard deviation are the stable setup due to the aluminium spacer, the large beam waist and the strong thermal effect. The error caused by inaccurate input parameters is very similar to the experiment presented in Sec. 4.2. Since the only difference for the experiment presented in this section is the beam waist, which is larger and therefore affects the result for the absorption less than the smaller waist in Sec. 4.2 due to the smaller intensity, it can be assumed that errors in the input parameters influence the result maximally linear in the present experiment too. This means that the standard deviation is dominating the error bar, if the error in the input parameters is 4% or smaller. For a input parameter which is known less accurate, the error of this parameter dominates the result.

8.2.3 Discussion and Conclusion

The Si/SiO₂ coatings show an extremely high absorption of 1000 ppm per coating at 1550 nm. This absorption is nearly three orders of magnitude above the absorption of the Ta₂O₅/SiO₂ coatings at 1550 nm. Apart from a high absorption of the material, problems with the AOI or the coating procedure (ion plating) can be reasons for this high absorption.

The Ta₂O₅/SiO₂ coatings in the experiment presented in Sec. 4.2 absorb 23.9 ppm per coating for an identical AOI. Due to a reduced penetration depth of the light field the absorption should decrease for s-polarization, it is very unlikely that the AOI causes the high absorption. Nevertheless a general problem designing low absorbing coatings for an AOI differing from 0° might be possible.

The Si/SiO₂ coatings were manufactured using the ion plating (IP) procedure which is known to induce higher losses than ion beam sputtering (IBS) used for the Ta₂O₅/SiO₂ coatings at 1064 nm and 1550 nm. Therefore using IBS could also reduce the absorption, although due to manufacturers information [8.20] for Si/SiO₂ coatings generally high losses are expected. Concrete reasons for a high absorption could not be named.

Summarizing, the absorption measured for Si/SiO₂ at 1550 nm in this experiment is much too high for applications in GWDs. A much lower absorption using IBS coatings under an AOI of 0° might be possible but is not very likely. However, it is planned to investigate Si/SiO₂ produced using IBS and optimized for an AOI of 0° at 1550 nm in a follow-up experiment.

8.2 Absorption Measurements on a Si/SiO₂ Coating at 1550 nm

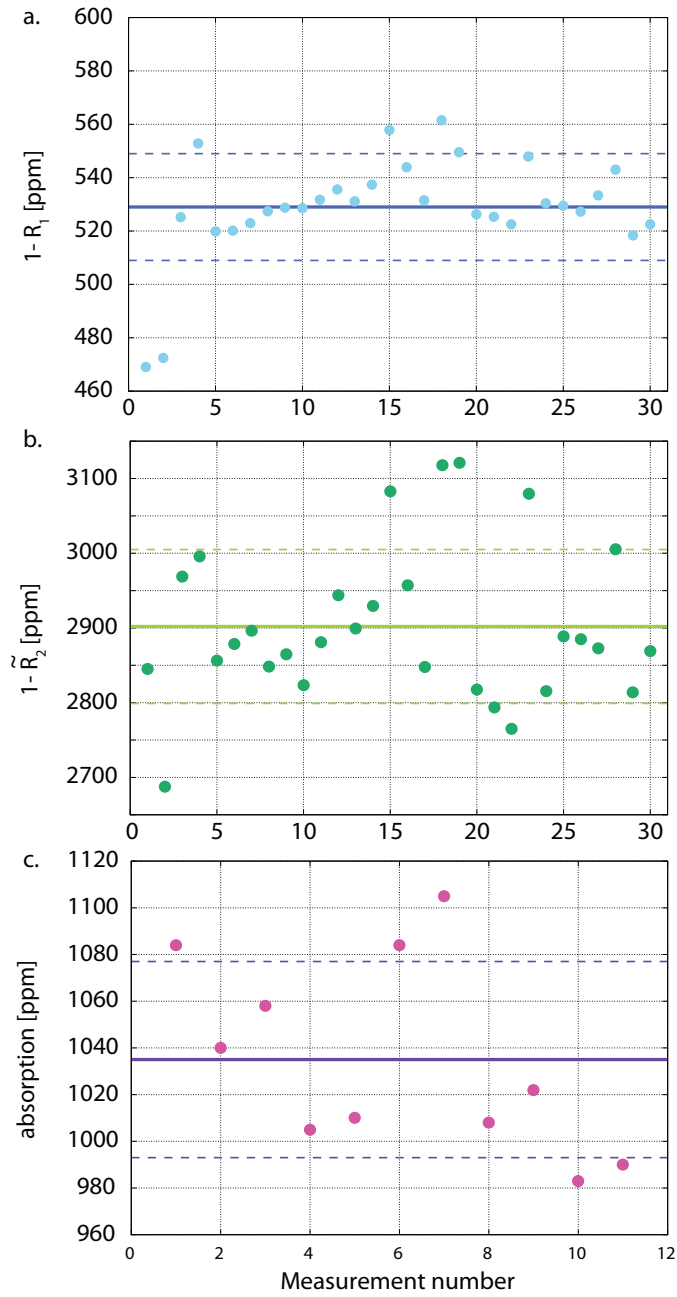


Figure 8.6: Measurement results for Si coatings at 1550 nm: a. shows the results for $1 - R_1$ in light-blue dots, mean value and standard deviation of all single results are marked by the blue line and dashed blue lines. b. shows the results of the single measurements for $1 - \tilde{R}_2$ in dark-green dots. Mean value and standard deviation are marked by the light-green line and dashed lines. The single results for the absorption of the input mirror coating are shown in c. by the pink dots. Mean value and standard deviation are marked by the purple line and dashed purple lines.

- 8.1 G. M. Harry, M. R. Abernathy, A. E. Becerra-Toledo, H. Armandula, E. Black, K. Dooley, M. Eichenfield, C. Nwabugwu, A. Villar, D. R. M. Crooks, G. Cagnoli, J. Hough, C. R. How, I. MacLar, P. Murray, S. Reid, S. Rowan, P. H. Sneddon, M. M. Fejer, R. Route, S. D. Penn, P. Ganau, J. Mackowski, C. Michel, L. Pinard, A. Remillieux
Titania-doped tantala/silica coatings for gravitational-wave detection
Class. Quantum Grav. **24** 405–415, 2007
- 8.2 G. M. Harry, A. M. Gretarsson, P. R. Saulson, S. E. Kittelberger, S. D. Penn, W. J. Startin, S. Rowan, M. M. Fejer, D. R. M. Crooks, G. Cagnoli, J. Hough, N. Nakagawa
Thermal noise in interferometric gravitational wave detectors due to dielectric optical coatings
Class. Quantum Grav. **19** 897–917, 2002
- 8.3 S. J. Waldman (for the LIGO Science Collaboration)
Status of LIGO at the start of the fifth science run
Class. Quantum Grav. **23** S653–S660, 2006
- 8.4 G. Harry On Behalf of the LIGO Science Collaboration
Optical Coatings for Gravitational Wave Detection
Optical Interference Coatings Conference – Tucson AZ, 2004
- 8.5 I. Martin, H. Armandula, C. Comtet, M. M. Fejer, A. Gretarsson, G. Harry, J. Hough, J.-M. M. Mackowski, I. MacLaren, C. Michel, J.-L. Montorio, N. Morgado, R. Nawrodt, S. Penn, S. Reid, A. Remillieux, R. Route, S. Rowan, C. Schwarz, P. Seidel, W. Vodel, A. Zimmer
Measurements of a low-temperature mechanical dissipation peak in a single layer

Bibliography

- of Ta₂O₅ doped with TiO₂
Class. Quantum Grav. **25** 055005, 2008
- 8.6 S. Hild, S. Chelkowski, A. Freise, J. Franc, N. Morgado, R. Flaminio, R. DeSalvo
A xylophone configuration for a third-generation gravitational wave detector
Class. Quantum Grav. **27** 015003, 2010)
- 8.7 R. Nawrodt, A. Zimmer, T. Koettig, C. Schwarz, D. Heinert, M. Hudl, R. Neubert,
M. Thürk, A. Tünnermann, S. Nietzsche, W. Vodel, P. Seidel
High mechanical Q-factor measurements on silicon bulk samples
Journal of Physics: Conference Series **122** 012008, 2008
- 8.8 D. F. McGuigan, C. C. Lam, R. Q. Gram, A. W. Hoffman, D. H. Douglass
Measurements of the Mechanical Q of Single-Crystal Silicon at Low Temperatures
Journal of Low Temperature Physics **30** 621–629, 1978
- 8.9 M. J. Keever, M. A. Green
Absorption edge of silicon from solar cell spectral response measurements
Appl. Phys. Lett. **66** 174–176, 1995
- 8.10 R. Schnabel, M. Britzger, F. Brückner, O. Burmeister, K. Danzmann, J. Dück, T.
Eberle, D. Friedrich, H. Lück, M. Mehmet, R. Nawrodt, S. Steinlechner, B. Willke
Building blocks for future detectors: Silicon test masses and 1550 nm laser light
Journal of Physics Conference Series **228** 012029, 2010
- 8.11 B. J. Frey, D. B. Leviton, T. J. Madison
Temperature dependent refractive index of silicon and germanium
arXiv:physics/0606168v1, 2006
- 8.12 D. B. Leviton, B. J. Frey
Temperature-dependent absolute refractive index measurements of synthetic fused
silica
Proc. SPIE **6273** Optomechanical Technologies for Astronomy 62732K, 2006
- 8.13 M. J. Weber
Handbook of optical materials
CRC Press LLC Boca Raton (FL) USA, 2003
- 8.14 www.lightmachinery.com
- 8.15 www.corning.com
Corning 7980 Product Sheet
- 8.16 Valley Design Corporation, Santa Cruz
USA <http://www.valleydesign.com>

- 8.17 ATFilms, USA
<http://www.atfilms.com>
- 8.18 G. Rempe, R. J. Thompson, H. J. Kimble, R. Lalezari
Measurement of ultralow losses in an optical interferometer
Optics Letters **17** No. 5 363–365, 1992
- 8.19 Tafelmaier Dünnschicht-Technik GmbH, Rosenheim, Germany
www.tafelmaier.de
- 8.20 Personal communication with manufacturers

To increase the sensitivity of 3rd generation gravitational wave detectors (GWDs) such as the Einstein Telescope (ET), it is planned to exploit techniques like cryogenically cooled test-masses to reduce thermal noise, and squeezed light injection to reduce quantum noise. For the reduction of these noise sources the optical absorption of the employed materials is relevant. To obtain precise knowledge of absorptions in the parts per million (ppm) regime, the photo-thermal self-phase modulation technique for absorption measurements was developed. Within this thesis, first absorption measurements were performed based on the simulation program `tksim` written by Nico Lastzka. The experimental application and verification of the results was provided and the measurement technique was established and limits of the simulation were determined. Exploiting the new technique, absorption measurements on materials relevant for the design of 3rd generation GWDs were performed.

Experiments were carried out to measure the absorption coefficient of a magnesium oxide doped lithium niobate ($\text{MgO}:\text{LiNbO}_3$) bulk substrate and the absorption of a fused silica and tantalum ($\text{SiO}_2/\text{Ta}_2\text{O}_5$) highly reflective mirror coating. For the LiNbO_3 bulk substrate an absorption coefficient of $\alpha_{\text{LN}} = 0.059\%/\text{cm}$ at a wavelength of 1064 nm was measured. This value is in agreement with the manufacturer's specification of $\alpha_{\text{LN}} < 0.1\%/\text{cm}$ and with results from a cavity round-trip loss measurement of $\alpha_{\text{LN}} \leq 0.07\%/\text{cm}$. The absorption result for $\text{SiO}_2/\text{Ta}_2\text{O}_5$ at 1064 nm was $\alpha = (23.9 \pm 2.0)$ ppm per coating, which is in excellent agreement with a calorimetric measurement performed at the Laser Zentrum Hannover (LZH), whose result was $\alpha = (25.0 \pm 3.3)$ ppm.

In the 1st and 2nd generation GWDs, $\text{SiO}_2/\text{Ta}_2\text{O}_5$ mirror coatings are used at a wavelength of 1064 nm. Since 3rd generation GWDs might operate at 1550 nm, the absorption of $\text{SiO}_2/\text{Ta}_2\text{O}_5$ was measured at this new wavelength and found to be $\alpha_{1550\text{nm}} = (1.7 \pm 0.3)$ ppm, comparable to the performance at 1064 nm. This is a promising result for

9 Conclusion

coatings which were not even specified to be low absorbing. Since in these coating-stacks, tantala is the material showing higher loss, a change to 1550 nm could give the chance to replace it by silicon (Si). The higher refractive index of Si ($n_{\text{Si}} = 3.5$) compared to tantala ($n_{\text{Ta}} = 2$) would reduce the number of necessary layers and the geometrical thickness of the Si layers significantly. First measurements showed an absorption of (1035 ± 42) ppm per coating of Si/SiO₂ at an angle of incidence (AOI) of 42° and s-polarization. An absorption this high is unsuitable for GWDs. The coatings were produced with the ion plating procedure. Since previous measurements showed higher absorptions under an AOI strongly differing from 0° it is recommended to measure the absorption of such coatings for an AOI of 0° in future experiments. Further the ion beam sputtering procedure could reduce absorption within the coatings. The measurement on SiO₂/Ta₂O₅ showed that at 1.7 ppm the sensitivity limit of the measurements technique was by far not reached. It is expected that coating absorptions at least two orders of magnitude below this value can be resolved.

Since quantum noise can be reduced by injecting squeezed light into GWDs, the non-linear crystalline material periodically poled potassium titanyl phosphate (PPKTP) was tested in view of its absorption coefficient. The results were $\alpha_{775\text{nm}} = (127 \pm 24)$ ppm/cm and $\alpha_{1550\text{nm}} = (84 \pm 40)$ ppm/cm. These results are of interest to derive an expected practical limit for future squeezed light lasers aiming at a maximal squeezing output, although it is worth mentioning that the residual PPKTP absorption will not constitute a limit for the ET squeezed light laser. Besides the high sensitivity, an advantage of the new absorption measurement technique is that it offers the possibility of exploiting already existing cavity setups to obtain the absorption of optical components as demonstrated with the two setups used for the measurements on PPKTP.

To reduce thermal noise, cryogenic test masses are planned for ET. Currently Si is considered as test-mass material, because of the high mechanical quality-factor at low temperatures, the high thermal conductivity and zeros of the thermal expansion coefficient at 125 K and 18 K. Therefore the optical absorption characteristics of crystalline Si are of interest. Around a laser wavelength of 1550 nm an absorption minimum of Si is assumed. In a first step, the room temperature absorption coefficient of an 11 k Ω cm sample was measured using a monolithic cavity setup. The absorption result of $\alpha_{\text{Si}} = (264 \pm 39)$ ppm/cm and a cavity round-trip loss measurement showed that almost 99% of the round-trip loss was caused by optical absorption. Recently, new results were reported, indicating an intensity-dependence of the Si absorption. The measurements using `tksim` were limited to the intensity of 700 W/cm². For lower power, a decreasing thermal effect increased the error bars and made it impossible to conclude an absorption coefficient. For higher power, the resonance peaks of this setup deformed in a way that was not reproducible by the simulation, which supports the assumption of an intensity-dependent absorption. This shows that the measurement technique is limited by non-linear absorption effects. Future experiments should concentrate on the ET intensity regime which is low due to a large beam diameter. Since for the monolithic

setup round-trip loss and absorption were almost identical, a finesse measurement will provide information about intensity dependent absorption effects.

To increase the sensitivity of cryogenic experiments which aim at the measurement and characterization of radiation pressure noise (RPN), the optical absorption and heating of silicon nitride membranes is of interest. With an infra-red camera the intensity-dependent temperature on the surfaces of membranes of different thicknesses was measured at wavelengths between 285 nm and $2\ \mu\text{m}$. Achieving thermally deformed resonance peaks requires strong heating for very thin substrates which conflicts with the assumptions made for `tksim`. Since the simulation also enables the measurement of cavity round-trip losses, the absorption of membranes at 1064 nm and 1550 nm was measured in this way. The results were used to calibrate the temperature measurements at the other wavelengths. The lowest absorption was found at 1550 nm, which showed an absorption decrease by a factor of about 10 compared to 1064 nm. A wavelength change thus can increase the sensitivity of an absorption-limited RPN experiment. The results of this thesis help in conquering the main noise sources of future GWDs in the complete frequency spectrum, i.e. RPN at low frequencies, thermal noise of coatings and test-masses in the mid-frequency range and shot-noise at high frequencies.

Acknowledgements

Finally, I would like to thank those who made this thesis possible.

Thank you, Prof. Dr. Karsten Danzmann, for the best institute I can imagine. I felt at home at the AEI Hannover from the first day and enjoyed every single day of the past years.

Especially, I want to thank Prof. Dr. Roman Schnabel for giving me the opportunity to work on this interesting topic, and for supervising and supporting this work.

For very helpful discussions during the experimental time and for proofreading parts of this manuscript I am very grateful to Tobias Eberle, Christina Vollmer, Vitus Händchen, Alexander Khalaidovski, Aiko Samblowski and Tobias Westphal.

I would like to thank Fabian Zywietz for the most entertaining corrections...

... and Ulrich Velte for innumerable nice coffee breaks!

And I want to thank all the people I met who encouraged and supported me during my university studies, especially Prof. Dr. Mikeska and Simon Barke.

My special thanks go to the two most important people of my life: Steini, who always was the first one to read, discuss and explain everything, who helped me to find time for working when time was rare and had patience I could never have. And little Jan for distracting me from work. Laptops were not only invented for working, but also for watching “trains” on Youtube!

Jessica Steinlechner, Dezember 2012

Curriculum Vitae

Personal Information

Jessica Steinlechner, nee Dück	Date of birth: 28.05.1981
Schaufelder Str. 27	Nationality: German
30167 Hannover	Marital status: married
Email: jessica.steinlechner@aei.mpg.de	

Education

since 03/2011	Doctoral studies in physics, Leibniz Universität Hannover
03/2010 – 02/2011	Parental leave
04/2007 – 02/2010	Doctoral studies in physics, Leibniz Universität Hannover
09/2001 – 01/2007	Physics studies, Leibniz Universität Hannover, Graduation (diploma)
08/1999 – 07/2001	Gymnasium “Wilhelm-Raabe-Schule” in Hannover, Graduation (Abitur)
08/1993 – 07/1999	Gymnasium Lehrte
08/1991 – 07/1993	“Orientierungsstufe Lehrte Süd” in Lehrte
08/1988 – 07/1991	Primary School “Grund- und Hauptschule Lehrte Süd” in Lehrte
09/1987 – 08/1988	Primary School “Grund- und Volksschule St. Johann” in Peißenberg

— 2012 —

1. **J. Steinlechner**, S. Ast, C. Krüger, A. Pal Singh, T. Eberle, V. Händchen, R. Schnabel, “Absorption Measurements of Periodically Poled Potassium Titanyl Phosphate (PPKTP) at 775 nm and 1550 nm”, *Sensors* **13**, 565–573, 2013
2. **J. Steinlechner**, L. Jensen, C. Krüger, N. Lastzka, S. Steinlechner, R. Schnabel, “Photothermal self-phase-modulation technique for absorption measurements on high-reflective coatings”, *Applied Optics* **51** 8, 2012.
3. J. Abadie, ..., E. Steinert, **J. Steinlechner**, S. Steinlechner, ..., X.-L. Zhang, “Search for Gravitational Waves Associated with Gamma-Ray Bursts During LIGO Science Run 6 and Virgo Science Runs 2 and 3”, *The Astrophysical Journal* **760** 12, 2012
4. J. Aasi, ..., E. Steinert, **J. Steinlechner**, S. Steinlechner, ..., J. Zweizig, “The characterization of Virgo data and its impact on gravitational-wave searches”, *Classical and Quantum Gravity* **29** 15, 2012.
5. J. Abadie, ..., E. Steinert, **J. Steinlechner**, S. Steinlechner, ..., M. Was, “Implications for the Origin of GRB 051103 from LIGO Observations”, *The Astrophysical Journal* **755** 51, 2012.
6. J. Abadie, ..., E. Steinert, **J. Steinlechner**, S. Steinlechner, ..., J. Zweizig, “All-sky search for gravitational-wave bursts in the second joint LIGO-Virgo run”, *Physical Review D* **85** 12, 2012.
7. J. Abadie, ..., E. Steinert, **J. Steinlechner**, S. Steinlechner, ..., J. Zweizig, “Upper limits on a stochastic gravitational-wave background using LIGO and Virgo interferometers at 600-1000 Hz”, *Physical Review D* **85** 12, 2012.

9 Conclusion

8. J. Abadie, ..., E. Steinert, **J. Steinlechner**, S. Steinlechner, ..., J. Zweizig, “Search for gravitational waves from intermediate mass binary black holes”, *Physical Review D* **85** 102004, 2012.
9. J. Abadie, ..., E. Steinert, **J. Steinlechner**, S. Steinlechner, ..., J. Zweizig, “First low-latency LIGO + Virgo search for binary inspirals and their electromagnetic counterparts”, *Astronomy & Astrophysics* **541** p. A155, 2012.
10. J. Abadie, ..., E. Steinert, **J. Steinlechner**, S. Steinlechner, ..., J. Zweizig, “Search for gravitational waves from low mass compact binary coalescence in LIGO’s sixth science run and Virgo’s science runs 2 and 3”, *Physical Review D* **85** 8, 2012.
11. J. Abadie, ..., E. Steinert, **J. Steinlechner**, S. Steinlechner, ..., J. Zweizig, “Implementation and testing of the first prompt search for gravitational wave transients with electromagnetic counterparts”, *Astronomy & Astrophysics* **539** p. A124, 2012.
12. J. Abadie, ..., E. Steinert, **J. Steinlechner**, S. Steinlechner, ..., J. Zweizig, “All-sky search for periodic gravitational waves in the full S5 LIGO data”, *Physical Review D* **85** 2, 2012.
- 2011 —
13. S. Ast, R. M. Nia, A. Schönbeck, N. Lastzka, **J. Steinlechner**, T. Eberle, M. Mehmet, S. Steinlechner, R. Schnabel, “High-efficiency frequency doubling of continuous-wave laser light”, *Optics Letters* **36** 17, 2011.
14. J. Abadie, ..., J. C. Driggers, **J. Dueck**, J.-C. Dumas, ..., J. Zweizig, “Directional Limits on Persistent Gravitational Waves Using LIGO S5 Science Data”, *Physical Review Letters* **107** 27, 2011.
15. J. Abadie, ..., E. Steinert, **J. Steinlechner**, S. Steinlechner, ..., J. Zweizig, “A gravitational wave observatory operating beyond the quantum shot-noise limit”, *Nature Physics* **7** 12, 2011.
16. J. Abadie, ..., A. J. Stein, **J. Steinlechner**, S. Steinlechner, ..., J. Zweizig, “Beating the Spin-Down Limit on Gravitational Wave Emission from the Vela Pulsar”, *The Astrophysical Journal* **737** 93, 2011.
17. J. Abadie, ..., A. J. Stein, **J. Steinlechner**, S. Steinlechner, ..., J. Zweizig, “Search for gravitational wave bursts from six magnetars”, *The Astrophysical Journal* **734** 2, 2011.

18. J. Abadie, ..., J. C. Driggers, **J. Dueck**, J.-C. Dumas, ..., J. Zweizig, “Search for gravitational waves from binary black hole inspiral, merger, and ring-down”, *Physical Review D* **83** 12, 2011.
19. J. Abadie, ..., J. C. Driggers, **J. Dueck**, I. Duke, ..., J. Zweizig, “Search for gravitational waves associated with the August 2006 timing glitch of the Vela pulsar”, *Physical Review D* **83** 4, 2011.

— 2010 —

20. N. Lastzka, **J. Steinlechner**, S. Steinlechner, R. Schnabel, “Measuring small absorptions by exploiting photothermal self-phase modulation”, *Applied Optics* **49** 28, 2010.
21. R. Schnabel, M. Britzger, F. Brückner, O. Burmeister, K. Danzmann, **J. Dück**, T. Eberle, D. Friedrich, H. Lück, M. Mehmet, R. Nawrodt, S. Steinlechner, and B. Willke, “Building blocks for future detectors: Silicon test masses and 1550 nm laser light”, *Journal of Physics: Conference Series* **228**, 2010
22. J. Abadie, ..., J. C. Driggers, **J. Dueck**, J.-C. Dumas, ..., J. Zweizig, “Calibration of the LIGO gravitational wave detectors in the fifth science run”, *Nuclear Instruments and Methods in Physics Research Section A: Accelerators, Spectrometers, Detectors and Associated Equipment* **624** 1, 2010.
23. J. Abadie, ..., J. C. Driggers, **J. Dueck**, J.-C. Dumas, ..., J. Zweizig, “Search for gravitational waves from compact binary coalescence in LIGO and Virgo data from S5 and VSR1”, *Physical Review D* **82** 10, 2010.
24. J. Abadie, ..., J. C. Driggers, **J. Dueck**, J.-C. Dumas, ..., J. Zweizig, “Predictions for the rates of compact binary coalescences observable by ground-based gravitational-wave detectors”, *Class. Quantum Grav.* **27** 17, 2010.
25. J. Abadie, ..., J. C. Driggers, **J. Dueck**, I. Duke, ..., J. Zweizig, “Search for Gravitational-Wave Inspirational Signals Associated with Short Gamma-Ray Bursts During LIGO’s Fifth and Virgo’s First Science Run”, *The Astrophysical Journal* **715** pp. 1453–1461, 2010.
26. J. Abadie, ..., J. C. Driggers, **J. Dueck**, I. Duke, ..., J. Zweizig, “All-sky search for gravitational-wave bursts in the first joint LIGO-GEO-Virgo run”, *Phys. Rev. D* **81** 10, 2010.
27. B. P. Abbott, ..., R. W. P. Drever, **J. Dueck**, I. Duke, ..., J. Zweizig, “Searches for Gravitational Waves from Known Pulsars with Science Run 5 LIGO Data”, *The Astrophysical Journal* **713** pp. 671–685, 2010.

— 2009 —

28. B. P. Abbott, ..., R. W. P. Drever, **J. Dueck**, I. Duke, ..., J. Zweizig, “Search for gravitational wave ringdowns from perturbed black holes in LIGO S4 data”, *Physical Review D* **80** p. 062001, 2009.
29. B. P. Abbott, ..., R. W. P. Drever, **J. Dueck**, I. Duke, ..., F. Robinet, “First LIGO search for gravitational wave bursts from cosmic (super)strings”, *Physical Review D* **80** p. 062002, 2009.
30. B. P. Abbott, ..., R. W. P. Drever, **J. Dueck**, I. Duke, ..., J. Zweizig, “Einstein@Home search for periodic gravitational waves in early S5 LIGO data”, *Physical Review D* **80** p. 0420023, 2009.
31. B. P. Abbott, ..., R. W. P. Drever, **J. Dueck**, I. Duke, ..., J. Zweizig, “An upper limit on the stochastic gravitational-wave background of cosmological origin”, *Nature* **460** pp. 990–994, 2009.
32. B. P. Abbott, ..., R. W. P. Drever, **J. Dueck**, I. Duke, ..., J. Zweizig, “Search for gravitational waves from low mass compact binary coalescence in 186 days of LIGO’s fifth science run”, *Physical Review D* **80** p. 047101, 2009.
33. B. P. Abbott, ..., R. W. P. Drever, **J. Dueck**, I. Duke, ..., J. Zweizig, “Stacked Search for Gravitational Waves from the 2006 SGR 1900+14 Storm”, *The Astrophysical Journal* **701** pp. L68–L74, 2009.
34. B. P. Abbott, ..., R. W. P. Drever, **J. Dueck**, I. Duke, ..., J. Zweizig, “LIGO: the Laser Interferometer Gravitational-Wave Observatory”, *Reports on Progress in Physics* **72** 7, 2009.
35. B. P. Abbott, ..., R. W. P. Drever, **J. Dueck**, I. Duke, ..., J. Zweizig, “Search for gravitational waves from low mass binary coalescences in the first year of LIGO’s S5 data”, *Physical Review D* **79** p. 122001, 2009.

— 2008 —

36. S. Steinlechner, S. Barke, **J. Dück**, L. Hoppe, R. A. Lorbeer, M. Otto, A. Sambrowski, T. Westphal, “Der Lifter”, *PhyDid A* **7** 20, 2008.

— 2006 —

37. **J. Dück**, “Neue Methoden zur Leistungsrauschmessung von Hochleistungslasern”, *Diploma Thesis*, Leibniz Universität Hannover, 2006.

